High harmonic generation in a Kronig-Penney model solid

Adam Thorpe

Thesis submitted to the University of Ottawa
in partial fulfillment of the requirements for the
Master of Science in Physics

Department of Physics
Faculty of Science
University of Ottawa

Abstract

In 2010 high harmonic generation (HHG) in solids was first observed where high order harmonics of a strong laser field's frequency were observed. HHG in solids is now a rapidly developing field that allows for exciting applications like fully solid state attosecond XUV sources and new ultrafast resolution imaging techniques for quantum dynamics in solids.

HHG in solids has been explained by two mechanisms: an interband mechanism, due to polarization associated with separate energy bands, and an intraband mechanism that results from nonlinearities and population changes associated with each individual band. While interband HHG has been seen in wide bandwidth semiconductors, intraband HHG has been observed in narrow bandwidth dielectrics. There has not yet been an explanation of the alternation of mechanisms with material differences. The main goal of this thesis is to attempt to provide a better understanding of the most important mechanisms and where they prevail. Although numerical modelling of HHG requires consideration of multiple energy bands, a two-band model consisting only of a valence band and a single conduction band can explain the most important mechanisms. This model requires a given material's band gap between its valence and conduction bands as well as dipole matrix elements between the bands. In this thesis we follow the Kronig-Penney model to develop a 1D δ-function potential model of solids to obtain these properties required of the two-band model. We implement this in a Wannier quasi-classical (WQC) model of interband HHG in semiconductors that explains the dominant dynamics leading to such through quasi-classical real space electron-hole pair trajectories. Although HHG in solids can be explained to be the result of a resonant process in which an electron-hole pair is generated in the first step, there are also virtual transition processes that lack consideration. These processes do not conserve energy and correspond to transitions to conduction bands resulting from field induced distortions of the ground state. We use methodology introduced by Keldysh for optical field ionization of atoms and solids along with the 1D δ-function potential model to quantify how both resonant and virtual transitions lead to HHG in solids for wide and low bandwidth solids.

Acknowledgements

First, and most importantly, I would like to thank my thesis supervisor Thomas Brabec for his ceaseless patience, wisdom, attention to detail and hospitality along the road of writing this thesis. Even more importantly, I would like to thank him for simply teaching me so much.

I would also like to thank all those professors who patiently answered my questions after class both as an undergraduate and as a graduate student.

I would like to say thanks to my parents for all the support and care along the way.

Finally, thanks to my brothers, as well as my good friend Chris for always helping me to catch a break and for their positivity.

Contributions

- Chapter 2, the development of the 1D δ-function potential model was done by me.
- Chapter 3 of this thesis is based on arXiv:2006.09651 [cond-mat.mes-hall] where Andrew Parks was the lead investigator. My contribution was the 1D δ-function potential there.
- All of the work leading to Chapter 4 was done by me.

Contents

List of Figures

Chapter 1

Introduction

The road to laser science was paved over a century ago when in 1917 Einstein wrote down his theory dealing with stimulated radiation vs. absorption and spontaneous emission [1]. Since then the field has been realized experimentally with achievements such as the first microwave maser in 1953 by Charles H. Townes, James P. Gordon and Herbert J. Zeiger [2] and the first visible light laser by Theodore Maiman [3] in 1960. Since these milestones laser science has been marked by numerous developments including the ability to generate increasingly short [4] and intense pulses [5]. Notably, in 1964 the concept of mode-locking [6, 7] has eventually allowed for pulses of durations on the order of femtoseconds [8]. This property relies on the coherent emission of photons by lasers; when more and more (frequency) laser modes can be locked coherently, shorter and more intense pulses are generated. These femtosecond pulses were fast enough for applications, such as Ahmed H. Zewail demonstrated in his 1988 paper [9], of observing chemical reactions as they occur. Nevertheless, it has been since demonstrated that femtosecond pulse durations are nowhere near as temporally short as pulses can be. As the pulse duration is limited by the laser carrier frequency to one optical cycle, shorter wavelength pulses are required, if one wants to achieve even shorter pulses. Research in the 1990s allowed attosecond science to be opened as a field when sub-femtosecond pulses were eventually generated in gas via a different mechanism called high harmonic generation (HHG) [10].

Perturbative nonlinear optics has been known since around the advent of lasers [11]. Second harmonic generation has been investigated with perturbative nonlinear optics in the 1960s [12]. Nevertheless, such theory cannot be used for considering phenomena in a sufficiently intense field [5]. When fields are intense enough, perturbative nonlinear optics is no longer valid and we enter the field of nonperturbative nonlinear optics. HHG takes place in this realm of nonperturbative nonlinear optics. HHG, in short, involves illuminating a medium with a strong field of angular frequency ω_0 so that the laser-medium dynamics cause coherent light bursts (that can be ultrafast [13, 14]) of higher

integer multiples of ω_0, or harmonics, to be emitted. The simplest example of such is HHG from an atomic gas. For atomic HHG the 'three-step model' is often invoked to explain the phenomenon [15]. The three steps of this model can be summarized as:

1. Ionization: a sufficiently intense laser field of frequency ω_0 allows a valence electron to tunnel out of its bound state from its parent ion.

2. Acceleration: the electron is accelerated away from the parent ion within the laser field until the field's polarization changes so that the electron accelerates towards the parent ion again.

3. Recombination: the electron recombines with the parent ion and additional energy obtained by the electron at the time of recombination is converted into light that can be a high harmonic of the laser frequency.

Spectra of atomic HHG are marked by odd harmonics (due to inversion symmetry) of the laser field within a high harmonic plateau region ending with a sudden cut-off [5]. The cut-off harmonic order energy $I_p + 3.17U_p$ is determined by the atom's ionization potential I_p as well as electronic motion in the field of a laser in the form of ponderomotive energy $U_p = e^2E_0^2/4m_e\omega_0^2$ (conventional units; e - electronic charge, E_0 - maximum field strength, m_e - electron mass, ω_0 - laser angular frequency) [5].

Besides the generation of sub-femtosecond pulses [13,14], HHG from gases has allowed for a variety of applications. The sub-femtosecond generated pulses of HHG allow for ultrafast time resolution of associated electronic processes [16, 17]. As such is the case, processes associated with atomic inner shell electrons and even nuclear mechanisms can be time resolved [16, 17]. Orbital tomography is also possible by allowing recollision electrons to interfere with molecular orbitals [10,18]. This is because recollision electrons tend to have wavelengths on the order of molecular orbital sizes (around 1 Å) [10]. In addition, HHG can be used to generate XUV radiation [19]. Recently, HHG has even been used to generate XUV radiation with time dependent orbital angular momentum, or self-torque [20]. Nevertheless, the gas phase presents inconveniences as a medium for fulfilling these applications, for example, due to the need of vacuum chambers.

A possible solution was found when in 2010 the first observed instances of HHG in solids were documented [21]. These experiments clearly demonstrated HHG in ZnO because odd harmonics as high as the 25th order were observed using a mid-infrared laser beam with a maximum intensity of around 5 TW/cm^2. Research of HHG in solids has developed into a hot topic. It has been since demonstrated in many more materials [22–31] such as other semiconductors like MgO [32] and MoS_2 [24]; insulating dielectrics like SiO_2 [25, 28]; amorphous glass [30] and even graphene [31].

As seen in the 2010 experiment, features of high harmonic spectra from solids are similar to those of atomic gases [21]. As with atomic gases, spectra are marked by high harmonic plateaus consisting of only odd harmonics followed by a sudden cut-off. Nevertheless, the cut-off harmonic for HHG in solids differs from atomic gases in that it has linear dependence on the electric field maximum rather than the square of such.

The theoretical model of HHG in solids is based on two mechanisms: an interband mechanism and an intraband mechanism [27, 33, 34]. The former is associated with polarization between valence and conduction bands while the latter results from nonlinear motion of charge carriers within individual bands. As a motivation, let us outline a highly simplistic model of interband HHG in solids that can be thought of analogously to the 'three-step model' of HHG in atomic gases [33, 35].

1. Ionization: an electron from a crystal's valence band is promoted to a conduction band and leaves a hole behind in the valence band.

2. Acceleration: the electron and hole are accelerated away from each other by the laser field until field polarization reverses such that they reapproach each other.

3. Recombination: The pair collide and emit a photon whose energy is defined according to the band gap between the bands corresponding to the momentum of the pair.

This model provides partial intuition of some important processes leading to HHG in solids. Nevertheless, understanding so far is incomplete. Semiconductors tend to have narrow minimum band gaps relative to dielectrics and as a result, to make strong field processes possible we need fewer photons so that longer wavelengths need to be used relative to dielectrics to bridge the maximum and minimum band gaps. Because of this, we say that semiconductors have greater bandwidths than dielectrics. Studies have demonstrated that interband HHG dominates in wide bandwidth semiconductors [32, 36] while in low bandwidth insulating dielectrics intraband HHG prevails [25, 28]. As such is the case, it is evident that there is a rift in overall comprehension of the dynamics of HHG in solids.

HHG in solids is of interest because of its various applications. For example, it can be used as a fully optical means of reconstructing crystal band properties [28, 37, 38]. In reference [37], the authours demonstrated that by using a weak second harmonic field to perturb internal dynamics leading to HHG in ZnO, that even harmonic signals are generated. These even harmonic signals were found to modulate appreciably with delay time. The phase of these modulations appeared to be of use for encoding crystal structure. In [38], the authours use an interband three-step model and demonstrated theoretically, for impurities in solids, the possibility of extracting transition dipole elements directly

from harmonic spectra, and from there, reconstructing the impurity ground state. As a final example, in [28], HHG from the dielectric SiO_2 is attributed to intraband current, with this assumption the lowest conduction band energy was constructed along a particular direction.

In addition, harmonic radiation bursts in solids can be ultrafast (on the order of attoseconds) such that they provide a solid state means of probing ultrafast solid state processes [26]. A notable example is demonstrated in [26] where an HHG experiment was done with GaSe. In this paper it is found that the temporal characteristics of high harmonic radiation can be used to map interference of electrons within multiple bands as a function of time.

Solid state media provide a particular advantage over gaseous media for generating high harmonics as it is possible to design solids with certain characteristics in order to control harmonic radiation [24,39–41]. For example, in [24] an experiment was done with a 2D monolayer of MoS_2. The authours found differing aspects of the high harmonic spectra in the low dimensional material compared to the same material in bulk. In particular, high harmonic efficiency was improved which was attributed mostly as a result of stronger Coulomb interactions. Another example is in [39] where nanoscale antennas made of gold that were embedded in a film of silicon increased harmonic brightness by ten times the amount without the antennas.

There is also, the possibility of generating XUV radiation with a solid state tabletop setup [28]. For example, in [28] a thin film of SiO_2 was illuminated with a 1.5-cycle field of just over 1 V/Å, with spectral a range of 1.1-2.5 eV to generate harmonics of energy greater than 30 eV. This is not the only example of an experiment where high harmonic radiation in the XUV range has been obtained. For example, XUV radiation has even been observed in glass [30]. Although XUV radiation can be generated using atomic HHG, the use of gaseous media for readily obtaining XUV radiation is difficult due to its containment in vacuum chambers. It is therefore advantageous to obtain the ability to generate XUV radiation from solid state media including abundantly available glass.

The preceding examples therefore demonstrate the potential usefulness HHG in solids provides. Nevertheless, as previously stated, the lack of understanding of the theory of HHG hinders the possibility of optimizing HHG from solids for use in its applications. This barrier indicates a need for more in depth analysis into processes leading to HHG in solids.

The goal of this thesis is to gain a better understanding of the variety of processes leading to HHG in both wide (e.g. semiconductors) and narrow bandwidth (e.g. insulating dielectrics) direct band gap materials. To do this, in the next section, we outline a simplistic two-band model of HHG in solids from [33] that we use throughout this thesis.

Although this model only implements two energy bands it can be used to analytically explain dominant interband and intraband features that may be more difficult to consider in more sophisticated multi-band numerical models (as an example see the supplement of [25]). As will be seen, the two-band model requires quantum mechanical solid state properties like valence-conduction band gaps and transition dipole moments between the two bands.

In Chapter 2 we will follow the Kronig-Penney model [42] and use a simple 1D δ-function potential model as a means to construct and obtain properties required of the two-band model for a large variety of solids. As we will see, this model is useful in that a direct band gap solid's properties can be adjusted with only two parameters: lattice spacing and 'strength' of potential barriers. It is useful not only for these reasons, but also because it allows us to define such properties like wavefunctions and dipole matrix elements mostly analytically.

In Chapter 3 we formulate an approximate and intuitive Wannier quasi-classical (WQC) model of HHG that can be used to explain the dominant dynamic mechanisms leading to HHG in semiconductors. This model relies on experimental observations of interband current being the dominant mechanism leading to HHG in semiconductors [32, 36]. As such, we will only consider interband HHG in this chapter. We will see that this model is similar to the simplistic 'three-step model' given above. It makes use of two particular mathematical techniques: Wannier functions and saddle point integration. In a periodic solid, Bloch functions are used to characterize eigenstates in terms of momentum space [43, 44]. Wannier functions are real space alternatives to these Bloch functions [45, 46]. By formulating the model in terms of a real space Wannier basis, we can gain insight into real space trajectories of electron-hole pairs leading to HHG. The use of saddle point integration techniques (see for example [47]), valid for wide bandwidth semiconductors, allows us to additionally characterize the dynamics via quasi-classical trajectories in terms of the time in which an electron-hole pair is created following tunnelling, the time of recombination and the momentum at the time of recombination. As will be seen, this model demonstrates reasonable agreement with fully numerical results for δ-function potential semiconductors. Therefore, the WQC model allows for accurate modeling of quantum processes with classical trajectories. Furthermore, the intuitive nature of this WQC model provides a means of understanding the most important aspects leading to HHG in semiconductors.

Finally, in Chapter 4, we will approach comprehension of HHG from a different point of view than in Chapter 3. As is the case with the explanation of Chapter 3, HHG is often explained entirely via resonant transitions for which energy conserving electron-hole pairs are born as a result of laser-matter interaction in the first step of the dynamic process

(see also for example, references: [33, 35]). There is a need to also take into account non-resonant or virtual transitions that are the result of laser field induced distortions to the ground state. These transitions do not conserve energy and the corresponding conduction band population disappears at the end of the laser pulse. To better understand HHG in solids it is therefore relevant to consider not only how resonant transitions result in HHG, but also the impact of non-resonant transitions on the final spectra. We will therefore follow references [36, 48] with Fourier analysis to extract resonant and non-resonant processes from interband and intraband mechanisms of HHG for a CW field. We will determine the relative weights of the differing processes in influencing HHG and interpret how resonant and non-resonant transitions influence HHG in both wide and narrow bandwidth solids. We will see that resonant transitions primarily drive interband HHG and non-resonant transitions drive intraband HHG, and the reasoning for such.

As a final note, within this thesis all equations will be expressed in terms of Hartree atomic units (au) unless specified otherwise (see Table A.1 in Appendix A for conversions between atomic units and SI units).

1.1 The two-band model of HHG in solids

We outline here the two-band model as explained in [33] and its supplement. This is a useful, but simple method of considering processes leading to HHG in solids. With this model we implement only the valence band and the first conduction band of a solid and consider only a single active electron. The advantage of this model is its potential for constructing analytical models, as will be seen.

We start with the solid's time independent Hamiltonian $\hat{H}_0 = \hat{T} + V(\mathbf{x})$, where $\hat{T} = 1/2\hat{\mathbf{p}}^2$ is the kinetic energy operator, $\hat{\mathbf{p}} = -i\nabla$ is the momentum operator and $V(\mathbf{x})$ is the periodic potential of the solid. As a result of Bloch's theorem [43] we can express the corresponding eigenstates and eigenvalues as $\Phi_{m,\mathbf{k}}(\mathbf{x}) = u_{m,\mathbf{k}}(\mathbf{x})e^{i\mathbf{k}\cdot\mathbf{x}}/\sqrt{V}$ and $E_{m,\mathbf{k}}$ respectively. Here V is the crystal volume, $u_{m,\mathbf{k}}(\mathbf{x})$ are periodic Bloch functions, $\mathbf{k}$ is the crystal momentum wavevector and $m = c$ (conduction band) or $m = v$ (valence band). Dressing the preceding Hamiltonian $\hat{H}_0$ with a laser field leads to the time-dependent Hamiltonian: $\hat{H}(t) = \hat{H}_0 - \mathbf{x}\cdot\mathbf{F}(t)$. We can express time-dependent wavefunctions by linearly combining the set of all time-independent eigenstates $\Phi_{m,\mathbf{k}}(x)$. Doing this leads to

$$\Psi(\mathbf{x},t) = \sum_{m=c,v}\int_{BZ} a_m(\mathbf{k},t)\Phi_{m,\mathbf{k}}(\mathbf{x})d^3\mathbf{k}, \tag{1.1}$$

where $a_m(\mathbf{k},t)$ are the time-dependent probability coefficients corresponding to states

$\Phi_{m,\mathbf{k}}(\mathbf{x})$. Applying the time-dependent Schrödinger equation with $\hat{H}(t)$, multiplying by $-i\Phi_{m,\mathbf{k}}(\mathbf{x})$ and then integrating over position leads to

$$\dot{a}_m = \left(-iE_{m,\mathbf{k}} + \mathbf{F}(t)\nabla_k\right) a_m + i\mathbf{F}(t) \sum_{m' \neq m} \mathbf{d}_{mm'}(\mathbf{k}) a_{m'}, \tag{1.2}$$

where $\mathbf{d}_{mm'}$ is a transition dipole matrix element that can be expressed in one form as

$$\mathbf{d}_{mm'}(\mathbf{k}) = \frac{-i}{v} \int_v d^3\mathbf{x} u^*_{m,\mathbf{k}}(\mathbf{x}) \nabla_{\mathbf{k}} u_{m',\mathbf{k}}(\mathbf{x}), \tag{1.3}$$

where v defines the unit cell volume. A relationship of the form $\langle \Phi_{m,\mathbf{k}}(\mathbf{x}) | \hat{\mathbf{x}} | \Phi_{m',\mathbf{k}'}(\mathbf{x}) \rangle = -i\nabla_{\mathbf{k}'}\delta_{mm'}\delta(\mathbf{k}' - \mathbf{k}) + \mathbf{d}_{mm'}(\mathbf{k})$ was used to obtain the result (see [49] which the original derivation [33] cites).

Although it is possible to use (1.2) to calculate processes such as band populations important for HHG, the equation is difficult to work with (e.g. due to the presence of ∇_k). We can simplify this by using an approach used by Keldysh in [48] by letting $a_m = b_m e^{-i\int_{-\infty}^{t} E_m dt'}$ and also by allowing $\mathbf{K} = \mathbf{k} - \mathbf{A}(t)$ where $\mathbf{A}(t)$ is the laser field's vector potential such that $\mathbf{F}(t) = -d\mathbf{A}(t)/dt$. By doing this we arrive at the following coupled differential equations:

$$\dot{b}_v(\mathbf{K}, t) = i\mathbf{F}(t) \cdot \mathbf{d}(\mathbf{K} + \mathbf{A}(t)) b_c(\mathbf{K} + \mathbf{A}(t)) e^{-iS(\mathbf{K},t)} \tag{1.4a}$$

$$\dot{b}_c(\mathbf{K}, t) = i\mathbf{F}(t) \cdot \mathbf{d}^*(\mathbf{K} + \mathbf{A}(t)) b_v(\mathbf{K} + \mathbf{A}(t)) e^{iS(\mathbf{K},t)}, \tag{1.4b}$$

where $\mathbf{d}(\mathbf{K} + \mathbf{A}(t)) = \mathbf{d}_{vc}(\mathbf{K} + \mathbf{A}(t))$, $\mathbf{d}^*(\mathbf{K} + \mathbf{A}(t)) = \mathbf{d}_{cv}(\mathbf{K} + \mathbf{A}(t))$,

$$S(\mathbf{K}, t) = \int_{-\infty}^{t} \mathcal{E}_g(\mathbf{K} + \mathbf{A}(t')) dt', \tag{1.5}$$

and $\mathcal{E}_g = E_c - E_v$ is the band gap.

Next we form density matrix terms describing population and coherence properties of the two-band system. This is done by considering band populations to be given by $n_m(\mathbf{K}, t) = |b_m(\mathbf{K}, t)|^2$ and coherence terms to be given by $\pi(\mathbf{K}, t) = b_c^*(\mathbf{K}, t) b_v(\mathbf{K}, t)$ and its complex conjugate. The original derivation [33] asserts that coherence terms relate to polarization by the expression

$$\mathbf{p}(\mathbf{K}, t) = \mathbf{d}^*(\mathbf{K} + \mathbf{A}(t)) \pi(\mathbf{K}, t) e^{iS(\mathbf{K},t)} + c.c. \tag{1.6}$$

Using the definitions of $n_m(\mathbf{K}, t)$ and $\pi(\mathbf{K}, t)$ along with equations (1.4) we arrive at

characteristic optical Bloch equations given by

$$\dot{\pi}(\mathbf{K},t) = -\frac{\pi(\mathbf{K},t)}{T_2} - i\Omega(\mathbf{K},t)w(\mathbf{K},t)e^{-iS(\mathbf{K},t)} \tag{1.7a}$$

$$\dot{n}_m(\mathbf{K},t) = is_m\Omega^*(\mathbf{K},t)\pi(\mathbf{K},t)e^{iS(\mathbf{K},t)} + c.c. \tag{1.7b}$$

where T_2 is a phenomenologically implemented dephasing time, $w(\mathbf{K},t) = n_v(\mathbf{K},t) - n_c(\mathbf{K},t)$ is the population difference, $\Omega(\mathbf{K},t) = \mathbf{F}(t)\cdot\mathbf{d}(\mathbf{K}+\mathbf{A}(t))$ is the Rabi frequency and $s_m = \pm 1$ is positive for $m = c$ and negative for $m = v$.

Before continuing further with equations (1.7), a strong field interacting with a solid leads to two types of current (intraband $\mathbf{j}_{ra}(t)$ and interband $\mathbf{j}_{er}(t)$) that lead to HHG. These are given by [33]:

$$\mathbf{j}_{ra}(t) = \sum_{m=c,v}\int_{\overline{BZ}} \mathbf{v}_m[\mathbf{K}+\mathbf{A}(t)]n_m(\mathbf{K},t)d^3\mathbf{K}, \tag{1.8a}$$

$$\mathbf{j}_{er}(t) = \frac{d}{dt}\int_{\overline{BZ}} \mathbf{p}(\mathbf{K},t)d^3\mathbf{K}, \tag{1.8b}$$

where $\overline{BZ} = BZ - A(t)$ is the shifted Brillouin zone and $\mathbf{v}_m(\mathbf{k}) = \nabla_{\mathbf{k}}E_{m,\mathbf{k}}$ is the band velocity. The intraband current $\mathbf{j}_{ra}$ is due to nonlinear movement of charge (in response to an applied field) and population variation of charge within individual bands. Interband current $\mathbf{j}_{er}$ results from changing polarization between the valence and the conduction bands. We can obtain high harmonic spectra by taking the absolute square of the Fourier transforms of these currents: $|\mathcal{F}\{\mathbf{j}_{ra}(t)+\mathbf{j}_{er}(t)\}|^2$

To obtain expressions for (1.8) in the frequency domain we consider a simplification to equations (1.7) where we set $w(\mathbf{K},t) \approx 1$ (frozen valence band approximation [48]). Doing so, in terms of $\mathbf{k}$, leads to

$$\mathbf{j}_{ra}(t) = \int_{BZ} d^3\mathbf{k}\mathbf{v}(\mathbf{k})\Bigg\{\int_{-\infty}^{t} dt'\mathbf{F}(t')\cdot\mathbf{d}(\boldsymbol{\kappa}_{t'}) \times \int_{-\infty}^{t'} dt''\mathbf{F}(t'')\cdot\mathbf{d}^*(\boldsymbol{\kappa}_{t''})e^{-iS(\mathbf{k},t'',t')-(t'-t'')/T_2} + c.c.\Bigg\}, \tag{1.9a}$$

$$\mathbf{j}_{er}(t) = \frac{d}{dt}\Bigg\{\int_{BZ} d^3\mathbf{k}\mathbf{d}(\mathbf{k})\int_{-\infty}^{t} dt'\mathbf{F}(t')\cdot\mathbf{d}^*(\boldsymbol{\kappa}_{t'})e^{-iS(\mathbf{k},t',t)-(t-t')/T_2} + c.c.\Bigg\}, \tag{1.9b}$$

so that in the angular frequency domain,

$$\mathbf{j}_{ra}(\omega) = \int_{BZ} d^3\mathbf{k}\mathbf{v}(\mathbf{k}) \int_{-\infty}^{\infty} dt e^{-i\omega t} \Bigg\{ \int_{-\infty}^{t} dt' \mathbf{F}(t') \cdot \mathbf{d}(\boldsymbol{\kappa}_{t'}) \times \int_{-\infty}^{t'} dt'' \mathbf{F}(t'') \cdot \mathbf{d}^*(\boldsymbol{\kappa}_{t''}) e^{-iS(\mathbf{k},t'',t')-(t'-t'')/T_2} + c.c. \Bigg\}, \quad (1.10a)$$

$$\mathbf{j}_{er}(\omega) = -i\omega \int_{-\infty}^{\infty} dt e^{-i\omega t} \Bigg\{ \int_{BZ} d^3\mathbf{k}\mathbf{d}(\mathbf{k}) \int_{-\infty}^{t} dt' \mathbf{F}(t') \cdot \mathbf{d}^*(\boldsymbol{\kappa}_{t'}) e^{-iS(\mathbf{k},t',t)-(t-t')/T_2} + c.c. \Bigg\}, \quad (1.10b)$$

where $\mathbf{v}(\mathbf{k}) = \mathbf{v}_c(\mathbf{k}) - \mathbf{v}_v(\mathbf{k}) = \nabla_{\mathbf{k}}\mathcal{E}_g(\mathbf{k})$ is the band velocity difference, $\boldsymbol{\kappa}_{t'} = \mathbf{k} + \mathbf{A}(t') - \mathbf{A}(t)$, and $S(\mathbf{k}, t', t) = \int_{t'}^{t} \mathcal{E}_g(\boldsymbol{\kappa}_\tau) d\tau$ is the classical action. This ends the derivation originally written in [33]. These equations provide us with the basis for much of the analysis that is to follow.

Chapter 2

1D δ-function potential model of solids

2.1 Introduction to the model

The two-band model of HHG described in the introduction requires solid state valence and conduction energy band functions as well as wavefunctions for calculating dipole matrix elements. To do this we want a model for solids that makes analysis simple and is also adjustable to analyse HHG for solids with different characteristics (i.e. minimum band gaps and bandwidths). One that allows for this follows the Kronig-Penney model [42], where we can model potentials in 1D solids using a comb of Dirac δ-functions situated at atomic lattice sites. This model is given by

$$V(x) = \Omega \sum_{n=-\infty}^{\infty} \delta(x - na), \tag{2.1}$$

where Ω is the potential strength parameter, n indexes lattice sites and a is the spacing between lattice sites.

Before applying this model, let us describe how such a model arises similar to as described in [42]. A model solid can be described as being a lattice of rectangular potential barriers of widths b and heights V_0 with edges spaced by a distance a (see Figure 2.1). Such a model is simplified in the limits $b \to 0$ and $V_0 \to \infty$ while maintaining the finite area $V_0 b = \Omega$ of potential barriers before these limits are applied. Therefore, in (2.1) Ω represents this potential barrier area and a is the spacing between adjacent δ-function barriers (equal to the spacing between rectangular well centres in old model). So despite this model being a simplification, it retains certain properties of a finite rectangular barrier model.

Finally, this model is useful in that the 1D model can be extended to similar higher

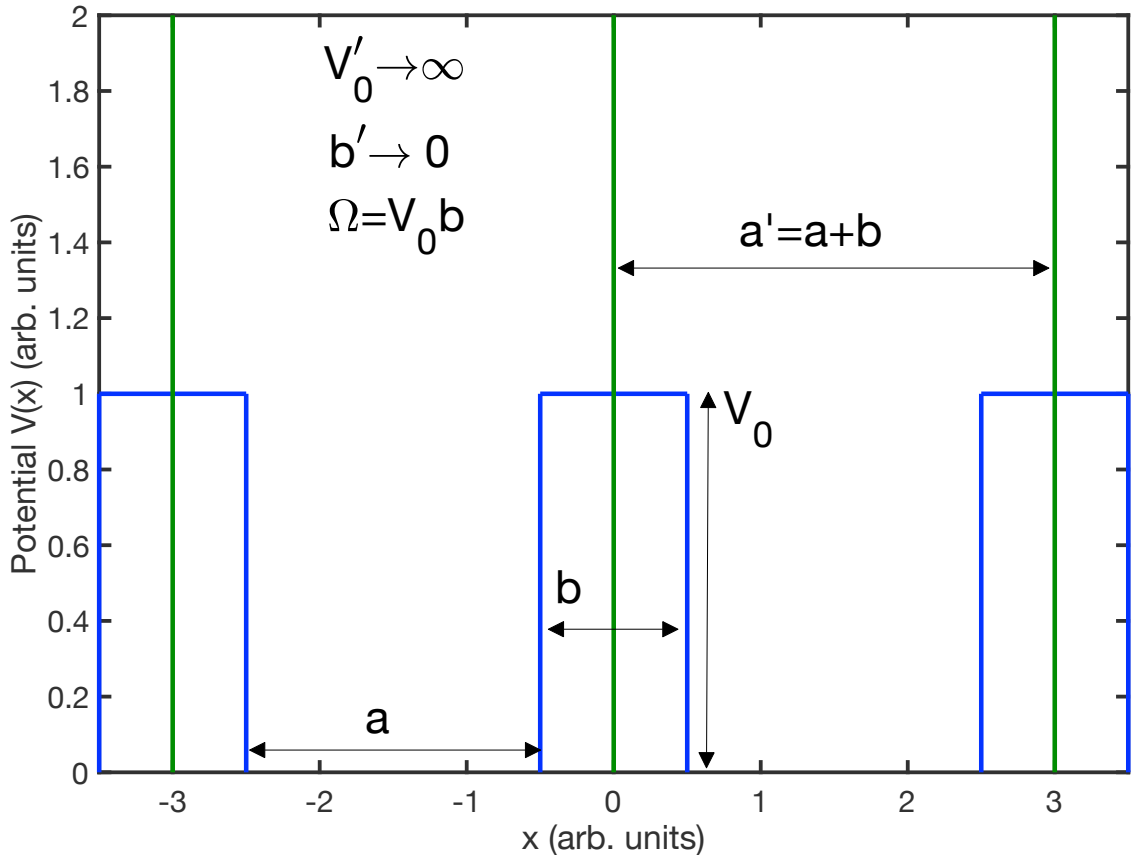

Figure 2.1: Transformation from a 1D solid potential model consisting of finite rectangular barriers (blue) of heights V_0, widths b and spacing a to a δ-function potential model (green) as in (2.1) by applying the limits $V_0' \to \infty$ and $b' \to 0$ while maintaining the finite 'area' below the barriers of $\Omega = V_0 b$. The spacing between the δ-function barriers becomes $a' = a + b$.

dimensional models with little extra work because, in three dimensions for example, one can write the potential as a sum of potentials along each dimension: $V(x, y, z) = V_x(x) + V_y(y) + V_z(z)$ [42]. This corresponds to rectangular prism shaped cells with δ-function potential barriers as walls. It is not directly analogous to the preceding 1D model because δ-function barriers are not located at individual lattice sites. Nevertheless, a model of this form allows for the Schrödinger equation to become separable and, as a result, eigenfunctions have the form $\Phi(x, y, z) = \Phi_x(x)\Phi_y(y)\Phi_z(z)$ with eigenvalues $E = E_x + E_y + E_z$.

2.2 The energy-momentum dispersion relation

Our analysis with the 1D δ-function potential of (2.1) begins by expressing the stationary Schrödinger equation as

$$\kappa^2 = -\frac{\partial^2 \Phi_k(x)}{\partial x^2} + 2\Omega \sum_n \delta(x - na)\Phi_k(x), \tag{2.2}$$

where κ relates to energy eigenvalues through $\kappa^2 = 2E$. We have indicated the crystal momentum wavenumber k as a subscript to the wavefunctions because the lattice potential is periodic and when this is the case according to Bloch's theorem [43] wavefunctions have the form: $\Phi_k(x) = u_k(x)e^{ikx}$ ($u_k(x) = \Phi_k(x)e^{-ikx}$), where $u_k(x)$ repeats with the lattice spacing a.

Solving (2.2) the equation in the region where $0 < x < a$ leads to

$$\Phi_k(x) = Ae^{i\kappa x} + Be^{-i\kappa x}, 0 < x < a, \tag{2.3}$$

where A and B are unknown coefficients. Using Bloch's theorem due to the periodicity of the lattice potential then leads to

$$u_k(x) = Ae^{i(\kappa-k)x} + Be^{-i(\kappa+k)x}, \tag{2.4}$$

and also,

$$\Phi_k(x) = e^{ika}\left[Ae^{i\kappa(x-a)} + Be^{-i\kappa(x-a)}\right], a < x < 2a, \tag{2.5}$$

where we assume a crystal momentum wavenumber k in the first Brillouin zone ($\frac{-\pi}{a} < k < \frac{\pi}{a}$).

We now apply the following boundary conditions:

$$\lim_{\varepsilon\to 0} \Phi_k(a - \varepsilon) = \Phi_k(a + \varepsilon), \tag{2.6a}$$

$$\lim_{\varepsilon\to 0} \int_{a-\varepsilon}^{a+\varepsilon} dx \frac{\partial^2 \Phi_k(x)}{\partial x^2} + \left[\kappa^2 - 2\Omega\delta(x - a)\Phi_k(x)\right] = 0, \tag{2.6b}$$

where the first condition allows for wavefunctions to match on two sides of a δ-function site and the second allows for smooth variation across a δ-function site. Using these

conditions with (2.3) and (2.5) leads to

$$\left(e^{ika} - e^{i\kappa a}\right) A + \left(e^{ika} - e^{-i\kappa a}\right) B = 0, \tag{2.7a}$$

$$\left(e^{ika} - e^{i\kappa a} + \frac{2i\Omega}{\kappa} e^{i\kappa a}\right) A - \left(-e^{ika} + e^{-i\kappa a} + \frac{2i\Omega}{\kappa} e^{-i\kappa a}\right) B = 0. \tag{2.7b}$$

As a result, we arrive at the standard Kronig-Penney model energy-momentum dispersion relation [42]:

$$\cos(ka) = \cos(\kappa_m a) + \frac{\Omega}{\kappa_m} \sin(\kappa_m a). \tag{2.8}$$

We have included indices $m = 1, 2, ...$ to indicate the different energy bands $E_{m,k}$ that can be solved numerically or approximately using this dispersion relation. In this thesis we use only the valence band ($m = 2$) and the conduction band ($m = 3$) as we use the two-band model of HHG as explained in the introduction. We assume $m = 1$ to be a core band that is disregarded.

2.3 Nearest-neighbour model of the band gap

For much of the analysis throughout this thesis it is advantageous to be able to use simple forms of the energy bands $E_{m,k}$ and most importantly the energy difference between valence and conduction bands $\mathcal{E}_g(k) = E_{3,k} - E_{2,k}$. To do this, note that that because of the cosine k-dependence of the dispersion relation (2.8), we can write $\mathcal{E}_g(k)$ as a cosine series:

$$\mathcal{E}_g(k) = \frac{C_0}{2} + \sum_{n=1}^{\infty} C_n \cos(nka), \tag{2.9}$$

with coefficients

$$C_n = \frac{a}{\pi} \int_{\frac{-\pi}{a}}^{\frac{\pi}{a}} dk \mathcal{E}_g(k) \cos(nka). \tag{2.10}$$

In the nearest-neighbour model to the dispersion relation (2.8), where $\frac{\Omega}{\kappa_m} \gg 1$, it is often sufficient to use only C_0 and C_1. As a result, we can use an approximate band gap of cosine dependence: $\mathcal{E}_g(k) = E_g + \Delta\{1 - \cos(ka)\}$, where E_g is the minimum band gap and 2Δ is the bandwidth. To demonstrate this we first consider an analytical approximate model for such. Nevertheless, for the calculations throughout this thesis we instead use a

numerical approach that assumes cosine dependence on k. We will explain this approach afterwards.

2.3.1 Approximate analytical method

Although not used we will briefly explain it here. In this method we note that because $\frac{\Omega}{\kappa_m} \gg 1$ that the term $\frac{\Omega}{\kappa_m}\sin(\kappa_m a)$ is much more important than $\cos(\kappa_m a)$ in (2.8). Because of this we expect solutions to the dispersion relation to be close to the zeros of $\sin(\kappa_m a)$. Noting such, we seek approximate solutions to κ_m by introducing a perturbative parameter $\eta_m(k)$ and letting $\kappa_m a = m\pi + a\eta_m(k)$. We use this expression for $\kappa_m a$ within $\frac{\Omega}{\kappa}\sin(\kappa_m a)$ and $\cos(\kappa_m a)$ and Taylor expand (to second order) about $\frac{m\pi}{a}$ to obtain the following approximations:

$$\frac{\Omega}{\kappa}\sin(\kappa_m a) \approx (-1)^m \Omega a \left\{ \frac{1}{m\pi}\eta_m a - \frac{1}{(m\pi)^2}(\eta_m a)^2 \right\} \tag{2.11}$$

$$\cos(\kappa_m a) \approx (-1)^m \left\{ 1 - \frac{1}{2}(\eta_m a)^2 \right\}. \tag{2.12}$$

Combining these expressions as in (2.8) we obtain the following approximate dispersion relation:

$$\cos(ka) \approx (-1)^m \left\{ 1 + \frac{\Omega a}{m\pi}(\eta_m a) - \left(\frac{1}{2} + \frac{\Omega a}{(m\pi)^2} \right)(\eta_m a)^2 \right\}. \tag{2.13}$$

We can rearrange the above and then use the quadratic formula with regards to $\eta_m a$ to obtain

$$\eta_m(k)a = \frac{m\pi\Omega a}{(m\pi)^2 + 2\Omega a} \left\{ 1 \pm \sqrt{1 + \frac{2}{(\Omega a)^2}((m\pi)^2 + 2\Omega a)(1 - (-1)^m \cos(ka))} \right\}. \tag{2.14}$$

We then use the binomial approximation $(1+x)^l \approx 1 + lx$ for the square root with $l = 1/2$ and x being the second term within the square root. This approximation stems from the Taylor expansion of $(1+x)^l$ about $x = 0$, and is most effective for small values of x. In addition, we choose the minus sign before the square root so that we finally obtain

$$\eta_m(k)a = \frac{m\pi}{\Omega a}\left\{(-1)^m \cos(ka) - 1\right\}. \tag{2.15}$$

By returning to the expression $\kappa_m a = m\pi + a\eta_m(k)$ we then obtain the following approximation for $\kappa_{m,k}$:

$$\kappa_{m,k} = \frac{m\pi}{a} + \frac{m\pi}{\Omega a^2}\left\{(-1)^m \cos(ka) - 1\right\}. \tag{2.16}$$

From this we use $E_{m,k} = \kappa_{m,k}^2/2$ to obtain the following expression for the energy bands:

$$E_{m,k} = \frac{(m\pi)^2}{2a^2}\left(1 + \frac{1}{\Omega a}\left\{(-1)^m \cos(ka) - 1\right\}\right)^2. \tag{2.17}$$

We can now further approximate $E_{m,k}$ by once again using the binomial approximation $(1+x)^l \approx 1 + lx$ for the large squared bracket with $l = 2$ and x being the second term within it to obtain

$$E_{m,k} = \frac{(m\pi)^2}{2a^2} + \frac{(m\pi)^2}{\Omega a^3}\left\{(-1)^m \cos(ka) - 1\right\}. \tag{2.18}$$

Using the above we obtain the approximate band gap between conduction ($m = 3$) and valence ($m = 2$) bands as

$$\mathcal{E}_g(k) = \frac{\pi^2}{2a^2}\left(5 - \frac{36}{\Omega a}\right) + \frac{13\pi^2}{\Omega a^3}(1 - \cos(ka)). \tag{2.19}$$

We therefore found a band gap expression in the form $\mathcal{E}_g(k) = E_g + \Delta\{1 - \cos(ka)\}$ with $E_g = \frac{\pi^2}{2a^2}\left(5 - \frac{36}{\Omega a}\right)$ and $\Delta = \frac{13\pi^2}{\Omega a^3}$. Therefore, we observe that to the extent that this approximation is valid, that a solid's bandwidth 2Δ is increased by spatially compressing wavefunctions of individual cells by decreasing a and to a lesser extent decreasing well strength Ω so that wavefunctions are reduced less near cell boundaries. For the minimum band gap E_g, decreasing well strength Ω decreases it and it is clear that corresponding electronic wavefunctions become less bound. That is, the lower spatial confinement of wavefunctions corresponds to less distinction at minimum between energies of states of separate bands. Furthermore, it can be seen that the minimum band gap (assuming it is positive) has a maximum value of $E_g^{\max} = 5\pi^2/2a^2$ in the limit of maximally bound wavefunctions when $\Omega \to \infty$. Finally, varying a can either increase or decrease E_g subject to to a cubic function of $\frac{1}{a}$. According to how the parameters Ω and a result in variations of E_g and Δ we find, to the extent that this approximation works, that we can construct a wide range of solids with the δ-function potential model.

Also of note is that in the proceeding section we will determine wavefunctions for the δ-function potential model. In doing so we do not define the k-dependence of $\kappa_{m,k}$ analytically because we generally solve for this numerically in much of the results presented in this thesis. Nevertheless, the expression for such in (2.16) could possibly

be used for rough analytical wavefunction approximations provided the conditions of the nearest-neighbour model hold.

2.3.2 Numerical method

The numerical process of obtaining energy bands of the form $\mathcal{E}_g(k) = E_g + \Delta\{1 - \cos(ka)\}$ involves first solving for $\kappa_{m,k}$ using a standard root finding function with the dispersion relation of (2.8) in its entirety. In doing so we assume that the lowest band ($m = 1$) is a core band that is not affected by laser interactions and so can be discarded for our purposes. With the results of root finding we obtain the band gap $\mathcal{E}_g(k) = \frac{1}{2}\{\kappa_{3,k}^2 - \kappa_{2,k}^2\}$. From this we make use of the cosine series formalism of (2.9) and (2.10) and use numerical integration to calculate $\Delta = |C_1|$. The absolute value can be taken for inversion symmetric potentials. The minimum band gap E_g can be taken directly as the minimum of $\mathcal{E}_g(k) = \frac{1}{2}\{\kappa_{3,k}^2 - \kappa_{2,k}^2\}$.

2.4 Wavefunction determination

We next extend the model to determine wavefunctions that correspond to the valence and conduction energy bands needed for calculating transition dipole matrix elements

$$d_{mm'}(k) = \frac{-i}{a}\int_0^a dx u_{m,k}^*(x)\partial_k u_{m',k}(x) \tag{2.20}$$

required of the two-band model as mentioned in the introduction. To do this we return to equations (2.3) and (2.7a) to obtain the relationship between coefficients A and B of $B = -R_m A$, where

$$R_m = \frac{e^{ika} - e^{i\kappa_m a}}{e^{ika} - e^{-i\kappa_m a}} \tag{2.21}$$

can be thought of as a reflection coefficient about a δ-function potential site. From here we can express the part of the wavefunction where $0 < x < a$ (as in (2.3)) as

$$\Phi_{m,k}(x) = A\left\{e^{i\kappa_m x} - R_m e^{-i\kappa_m x}\right\}, 0 < x < a. \tag{2.22}$$

We next allow the crystal lattice to be defined over a finite length l such that we can write the wavefunction as

$$\Phi_{m,k}(x) = \frac{1}{\sqrt{l}} u_{m,k}(x) e^{ikx}, \tag{2.23}$$

where

$$u_{m,k}(x) = A\left\{e^{i(\kappa_m - k)x} - R_m e^{-i(\kappa_m + k)x}\right\}. \tag{2.24}$$

We now consider the normalization condition where we write the crystal length as $l = Na$ where N is the number of unit cells. We also note the repetition of $u_{m,k}(x)$ in different unit cells so that we can write

$$\frac{1}{a}\int_0^a |u_{m,k}(x)|^2 dx = 1. \tag{2.25}$$

We are therefore considering the normalization condition based on a single unit cell. Using this normalization condition alongside (2.24) we eventually (through common trigonometric identities and the energy-momentum dispersion relation) arrive at expressions for the square of the magnitude of the coefficient A_m:

$$|A_m|^2 = \frac{\kappa_m a\left\{1 - \cos[(\kappa_m + k)a]\right\}}{2\left(\kappa_m a + \frac{\Omega}{\kappa_m}\right)\sin^2(\kappa_m a) - \Omega a \sin(2\kappa_m a)} \tag{2.26}$$

$$= \frac{1 - \cos[(\kappa_m + k)a]}{2\left(1 + \frac{\Omega}{\kappa_m^2 a}\right)\sin^2(\kappa_m a) - \frac{\Omega}{\kappa_m}\sin(2\kappa_m a)}. \tag{2.27}$$

Although these expressions are fairly concise, they can sometimes be difficult to use for numerical calculations because when $k = 0$ and $\kappa = 2q\pi/a, q \in \mathbb{Z}$ the equations have the form of a $0/0$ limit case. Another form in terms of complex variables that works around this difficulty is

$$|A_m|^2 = \frac{a}{(1 + |R_m|^2)\, a - \frac{R_m^*}{2i\kappa_m}\left(e^{2i\kappa_m a} - 1\right) + \frac{R_m}{2i\kappa_m}\left(e^{-2i\kappa_m a} - 1\right)}. \tag{2.28}$$

This form of the equation can be calculated by directly applying the normalization condition to (2.24) without further rewriting complex exponents in the resultant equation in terms of sine and cosine functions.

If we take $A_m = |A_m|$ and use above expressions for $|A_m|^2$, we can then express the wavefunctions $\Phi_{m,k}(x)$ and their periodic parts $u_{m,k}(x)$ using (2.24) and (2.23) with R_m given in (2.21). The only unknown variable that remains is κ_m. As previously stated, this can be determined by solving the dispersion relation of (2.8) using numerical root finder algorithms or by approximate techniques in certain circumstances such as the nearest-neighbour model.

2.5 Alternative wavefunction choices

Above we have determined a form of wavefunctions for a 1D solid. Nevertheless, this is not the only choice that can be used because Bloch eigenfunctions are not uniquely defined since one can choose any real and periodic k-dependent phase factor $\alpha_m(k)$ such that $\Phi'_{m,k}(x) = \Phi_{m,k}(x)e^{i\alpha_m(k)}$ [50]. Furthermore, the dipole matrix elements $d_{mm'}(k)$ (see (2.20)) are gauge invariant in regards to this phase [49, 50]. In addition, in an inversion symmetric solid there is a choice that allows for purely real or imaginary non-diagonal dipole elements $d_{m\neq m'}$ [49]. Such a choice also results in zero diagonal dipole elements $d_{mm} = 0$ [49]. Such a choice is not only advantageous for its simplicity, but also because it can be seen from (2.20) that diagonal elements $d_{mm}(k)$ are essentially k-dependent Berry connection terms that are in turn associated with Berry phases [51]. Such a choice therefore removes the possibility of such geometric phases. Finally, in the next chapter we will switch from the k-space Bloch basis to the real space Wannier basis. In such a basis Wannier functions are real space functions that Bloch wavefunctions can be constructed from [46]. Wannier functions are maximally confined for the such a phase choice [46].

First, consider the energy-momentum dispersion relation $\cos(ka) = \cos(\kappa_m a) + (\Omega/\kappa_m)\sin(\kappa_m a)$. Replacing k with $-k$ leaves the relation unchanged. This means that $\Phi_{m,k}(x)$ and $\Phi_{m,-k}(x)$ have the same energy eigenvalues $E_{m,\pm k} = \kappa^2_{m,\pm k}/2$ and are therefore degenerate. As a result, linear combinations of these two solutions $(C_+\Phi_{m,k}(x) + C_-\Phi_{m,-k}(x))$ are also valid solutions. To remove any possible phase factor $\alpha_m(k)$ our goal is to determine coefficients C_+ and C_- so that solutions forming the linear combination are real. We will see that our work here is alike to choosing a coordinate center symmetric in the middle between two δ-peaks so that diagonal dipole elements $d_{mm} = 0$ (note this effect through the derivative with respect to k in (2.20)). To do this we first use (2.22) to write $\Phi_\pm = \Phi_{m,\pm k}(x)$ as:

$$\Phi_\pm = \frac{A_\pm}{\sqrt{l}}\left\{e^{i\kappa x} - R_\pm e^{-i\kappa x}\right\}. \tag{2.29}$$

Note next that from (2.21) the reflection coefficients for $\pm k$,

$$R_\pm = \frac{1 - e^{i(\kappa\mp k)a}}{1 - e^{-i(\kappa\pm k)a}}, \tag{2.30}$$

can be related to each other through new variables $\tilde{R}$ and δ such that $R_+ = \tilde{R}e^{i\delta}$ and

$R_- = e^{i\delta}/\tilde{R}$. Using these relations alongside the square root of (2.28) we obtain

$$A_\pm = \frac{1}{\sqrt{(1+\tilde{R}^{\pm 2}) + \tilde{R}^{\pm 1}\left\{\frac{e^{i\delta}}{2i\kappa a}\left(e^{-2i\kappa a}-1\right) + c.c.\right\}}}, \tag{2.31}$$

and note that the coefficients are related to each other through $A_- = \tilde{R}A_+$. We use these relations to obtain the following expressions for the periodic parts of the Bloch functions:

$$u_\pm = A_+ e^{i\frac{i\delta}{2}}\left(e^{\frac{\mp i\delta}{2}}e^{\pm i\kappa x} - \tilde{R}e^{\frac{\pm i\delta}{2}}e^{\mp i\kappa x}\right)e^{\mp ikx}. \tag{2.32}$$

To complete these forms of the equations we now only need to determine δ and $\tilde{R}$.

We obtain δ and $\tilde{R}$ by rearranging R_+ from (2.30) and by using the dispersion relation $\cos(ka) = \cos(\kappa a) + \frac{\Omega}{\kappa}\sin(\kappa a)$ such that we can write

$$R_+ = -\frac{\Omega}{\kappa}\frac{\sin(\kappa a)}{1-\cos\left[(\kappa+k)a\right]}e^{i\kappa a}. \tag{2.33}$$

From this we take $\delta = \kappa a + \pi$ and (with further use of algebra and the dispersion relation of (2.8))

$$\tilde{R} = \frac{\sin\left[(\kappa-k)\frac{a}{2}\right]}{\sin\left[(\kappa+k)\frac{a}{2}\right]}. \tag{2.34}$$

We use these results with (2.31) and (2.32) to obtain:

$$A_+ = \frac{1}{\sqrt{\left(1+\tilde{R}^2\right) + 2\tilde{R}\frac{\sin(\kappa a)}{\kappa a}}}, \tag{2.35}$$

$$u_\pm = A_+ e^{i\frac{\kappa a}{2}}\left(e^{\pm i\kappa\left(x-\frac{a}{2}\right)} + \tilde{R}e^{\mp i\kappa\left(x-\frac{a}{2}\right)}\right)e^{\mp ikx}. \tag{2.36}$$

The next step is to use the phase arbitrariness to define new Bloch functions through the transformation $\Phi'_\pm \to \Phi_\pm e^{\frac{-i\kappa a}{2}}$ to obtain

$$\Phi'_\pm = \frac{A_+}{\sqrt{l}}\left\{e^{\pm i(\kappa-k)\xi} + \tilde{R}e^{\mp i(\kappa+k)\xi}\right\}e^{\pm i\kappa\xi}, \tag{2.37}$$

where $\xi = x - a/2$. The corresponding periodic parts are defined by $\Phi'_\pm = u'_\pm e^{\pm ik\xi}/\sqrt{l}$

and are given by:

$$u'_{\pm} = A_{+}\left\{e^{\pm i(\kappa-k)\xi} + \tilde{R}e^{\mp i(\kappa+k)\xi}\right\}. \tag{2.38}$$

Considering equation (2.38), we find that $u_{+} = u^{*}_{-}$ and $\Phi_{+} = \Phi^{*}_{-}$ (we are now dropping the primes from the new variables) because both A_{+} and $\tilde{R}$ are real. Furthermore, for $k \in [0, \pi/a]$ the linear combinations

$$\Phi_1 = \frac{1}{2}(\Phi_{+} + \Phi_{-}), \tag{2.39a}$$

$$\Phi_2 = \frac{1}{2i}(\Phi_{+} - \Phi_{-}), \tag{2.39b}$$

are symmetric and antisymmetric about $\xi = 0$ respectively. Additional k-dependent phase is no longer present. Therefore, these equations satisfy a group theoretical constraint where an inversion symmetric potential must have symmetric and antisymmetric solutions about inversion centres [49]. We will therefore use periodic parts of Bloch functions that have the form of u_{+} as in (2.38) for calculating dipole moments as in the next section.

The wavefunction chosen in this section and related variables can be summarized by the following equations:

$$u_{m,k}(\xi) = A_m\left\{e^{i(\kappa_m-k)\xi} + \tilde{R}e^{-i(\kappa_m+k)\xi}\right\}, (\xi = x - a/2) \in [-a/2, a/2], \tag{2.40a}$$

$$\Phi_{m,k}(\xi) = \frac{1}{\sqrt{l}}u_{m,k}(\xi)e^{ik\xi}, \tag{2.40b}$$

$$A_m(k) = \frac{1}{\sqrt{\left(1 + \tilde{R}_m^2\right) + 2\tilde{R}_m\frac{\sin(\kappa_m a)}{\kappa_m a}}}, \tag{2.40c}$$

$$\tilde{R}_m(k) = \frac{\sin\left[(\kappa_m - k)\frac{a}{2}\right]}{\left[(\kappa_m + k)\frac{a}{2}\right]}, \tag{2.40d}$$

$$\cos(ka) = \cos(\kappa_m a) + \frac{\Omega}{\kappa_m}\sin(\kappa_m a). \tag{2.40e}$$

Note that the wavefunctions defined here are the same as ones that would have been

obtained had we shifted the origin in Figure 2.1 by $\pm a/2$. Only for such a shifted origin is the potential inversion symmetric with respect to a unit cell.

2.6 Calculation of dipole matrix elements

Wavefunctions are defined in the previous section that now allow us to calculate dipole matrix elements $d_{mn}(k)$ required of the two-band model of HHG as explained in the introduction.

The most important dipole matrix elements to calculate are those for which $m \neq n$, because in the two-band model the only matrix elements present are $d_{cv} = d_{32}$ and $d_{vc} = d_{23}$. Nevertheless, we consider a more general case where m and n correspond to any two separate energy bands as these dipole matrix elements could be of interest for more rigorous models of HHG.

For this section we will use an alternative way (see [50]) of writing dipole matrix elements to (2.20) that can be used for elements where $m \neq n$. That is we can use

$$d_{mn}(k) = \frac{ip_{mn}(k)}{\mathcal{E}_{mn}(k)}, \tag{2.41}$$

where $\mathcal{E}_{mn}(k) = E_{m,k} - E_{n,k}$ is the energy difference between the two bands and

$$p_{mn}(k) = \frac{1}{a}\int_0^a dx u^*_{m,k}(x)\hat{p}u_{n,k}(x) \tag{2.42}$$

is the momentum matrix element calculated from a single unit cell with $\hat{p} = -i\partial_x$.

We use $u_{m,k}(x)$ and $u_{n,k}(x)$ from (2.40) to calculate $p_{mn}(k)$ through direct differentiation followed by integration. Doing so leads to the following formula for dipole matrix elements:

$$\begin{aligned} d_{mn}(k) = i\frac{2A_mA_n}{\mathcal{E}_{mn}}\Bigg\{ &\left[(\kappa_n - k)\tilde{R}_m - (\kappa_n + k)\tilde{R}_n\right]\frac{\sin\left[(\kappa_n+\kappa_m)\frac{a}{2}\right]}{(\kappa_n+\kappa_m)a} \\ &+ \left[(\kappa_n - k) - \tilde{R}_m\tilde{R}_n(\kappa_n + k)\right]\frac{\sin\left[(\kappa_n-\kappa_m)\frac{a}{2}\right]}{(\kappa_n-\kappa_m)a}\Bigg\}, m \neq n. \end{aligned} \tag{2.43}$$

This can now be used to calculate interband and intraband high harmonic spectra.

Furthermore, as stated in Section 2.5 there is the requirement that $d_{mm} = 0$ for the wavefunction choice considered (see (2.40)). This can be shown to be true by direct evaluation using (2.20). Furthermore, in Figure 2.4 of Section 2.7 we numerically verify that this is the case for $d_{cc}(k)$ and $d_{vv}(k)$. We also demonstrate that these diagonal elements are not always zero for all values of k using wavefunctions defined in the initial

gauge of Section 2.4.

2.7 Example energy bands and dipole elements

Let us now consider examples of results arising from the 1D δ-function potential solid model that can be used within the two-band formulation of HHG. Here we consider two representative examples of solids with similar band gaps and different bandwidths that

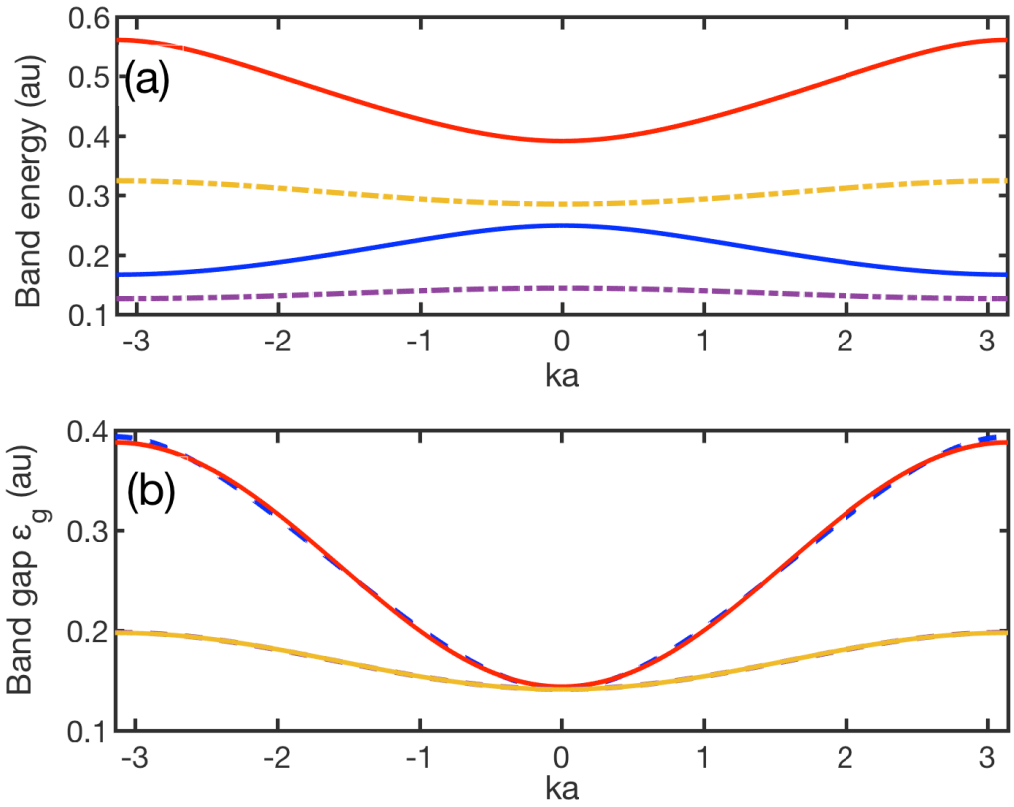

Figure 2.2: Comparison of energy band properties for a wide bandwidth material defined by parameters $a = 8.9$ au and $\Omega = 0.9$ au ($E_g = 0.1437$ au and $2\Delta = 0.2445$ au) and a narrow bandwidth material defined by parameters $a = 11.7$ au and $\Omega = 2.5$ au ($E_g = 0.1410$ au and $2\Delta = 0.0566$ au). In (a) valence energy bands are given by the blue solid and the purple dash-dotted lines for the wide and narrow bandwidth materials respectively. Also plotted there are conduction bands as red solid and orange dash-dotted lines for the wide and narrow bandwidth materials respectively. In (b) red (wide bandwidth material) and orange (narrow bandwidth material) solid lines correspond to numerically calculated band gaps $\mathcal{E}_g(k)$ assuming the nearest neighbour approximation. Also plotted are 'exact' band gaps as blue (wide bandwidth material) and purple (narrow bandwidth material) dashed lines.

can be constructed by choosing lattice spacing a and well strength Ω. The first is a wide bandwidth material with $a = 8.9$ au and $\Omega = 0.9$ au so that when approximated in the nearest-neighbour model the minimum band gap is $E_g = 0.1437$ au and the bandwidth is $2\Delta = 0.2445$ au. The other is a narrow bandwidth material with $a = 11.7$ au and $\Omega = 2.5$ au leading to $E_g = 0.1410$ au and $2\Delta = 0.0566$ au. Examples as such representing wide and narrow bandwidth materials are of interest for studying how HHG occurs in different classes of materials (in the context of strong field physics; see introduction) such as semiconductors (wide bandwidths) and insulating dielectrics (narrow bandwidths). Furthermore, these two bandwidth limits demonstrate the usefulness of the 1D δ-function potential model in that a wide variety of solids can be modelled with it simply by adjusting a and Ω.

In Figure 2.2 the valence and conduction energy bands (from numerically calculated $\kappa_{m,k}$ variables) for the wide and narrow bandwidth materials discussed above are plotted in part (a). We therefore observe how the model provides for distinct energy bands. In part (b) of the same figure, comparisons of 'exact' band gaps to those of the numerical nearest-neighbour model are plotted for the same two solids. We observe adequate agreement between the nearest-neighbour and 'exact' results for both solids. The only region of slight disagreement is near the Brillouin zone edges for the wide bandwidth material. This is because the nearest-neighbour model works best when $\Omega/\kappa_m \gg 1$ and $\kappa_{3,k}$ for the conduction band reaches an extreme in this region. Furthermore, the wide bandwidth material has a lower value of Ω (0.9 au) than that of the narrow bandwidth material (2.5 au) so that the ratio Ω/κ_m is prone to be smaller and therefore less representative of the nearest-neighbour model.

In addition, in Figure 2.3 we plot the imaginary part of the dipole matrix element $d_{cv}(k) = d^*_{vc}(k)$ (the real part is zero) as defined in (2.43) (using wavefunctions defined by (2.40)) for the same two solids. The variation is much greater for the wide bandwidth material than that of the narrow bandwidth material. The importance of transitions is mostly around the centre of the Brillouin zone, but drops off rapidly towards Brillouin zone edges. This is in contrast to the narrow bandwidth material that never has such great rises and drops. The importance of transitions does not change much at any given point in the Brillouin zone. For this reason the dipole matrix elements can sometimes be approximated as constant for narrow bandwidth materials such as dielectrics. In any case, we expect that such marked differences in dipole matrix elements for wide vs. narrow bandwidth materials should have important consequences on HHG in relation to the choice of a solid state medium.

Finally, in Figure 2.4 we plot numerically calculated diagonal dipole matrix elements $d_{cc}(k)$ and $d_{vv}(k)$, as well as $d_{cv}(k)$ derived instead from wavefunctions of Section 2.4

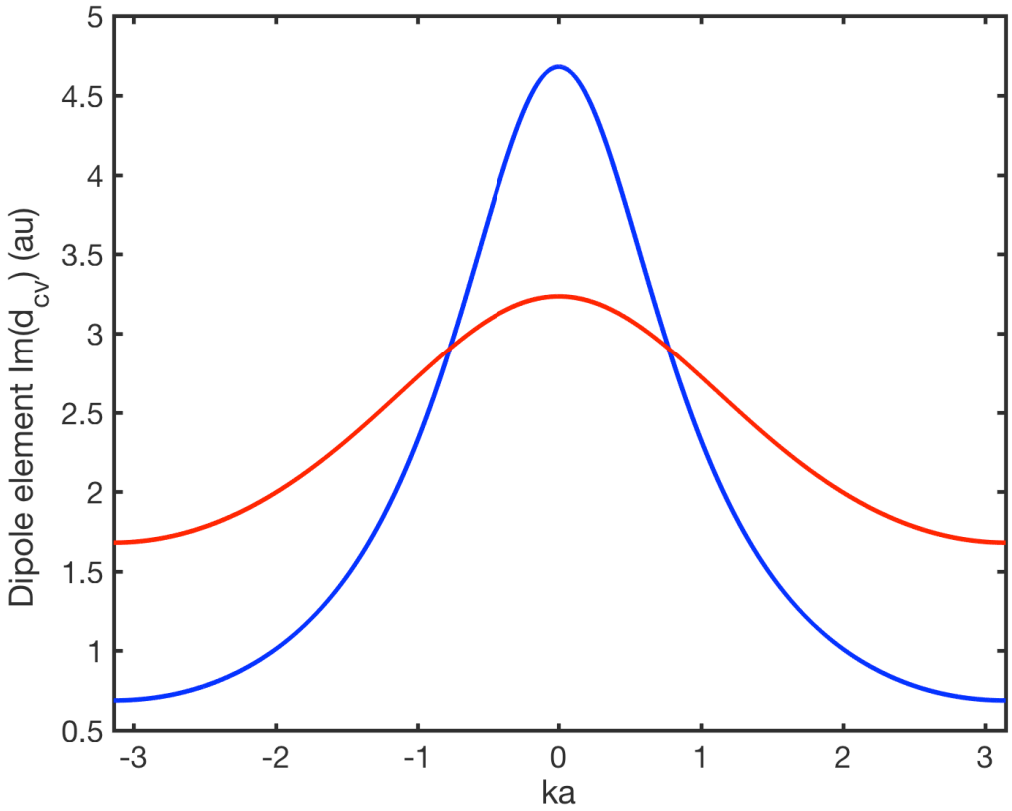

Figure 2.3: Non-zero, imaginary parts of dipole matrix elements $d_{cv}(k)$ calculated from (2.43). The blue line corresponds to a wide bandwidth material defined by parameters $a = 8.9$ au and $\Omega = 0.9$ au ($E_g = 0.1437$ au and $2\Delta = 0.2445$ au) and the red line corresponds to a narrow bandwidth material defined by parameters $a = 11.7$ au and $\Omega = 2.5$ au ($E_g = 0.1410$ au and $2\Delta = 0.0566$ au).

(see equations (2.21), (2.22), (2.24), and (2.28)) derived in the initial gauge. We observe that the non-diagonal elements $d_{cv}(k)$ have both real and imaginary parts as opposed to those as shown in Figure 2.3. The diagonal elements are also non-zero. For comparison we plotted numerically calculated diagonal matrix elements for wavefunctions of (2.40) that are used for Figure 2.3. This verifies that the diagonal elements are zero for the chosen gauge. Also note that the two-band expressions (1.10) given in the introduction are gauge invariant and give the same results for both gauges.

With the results of this chapter we now have a solid state model that can be used for actually performing HHG calculations with the two-band model. We consider HHG calculations in the next chapters.

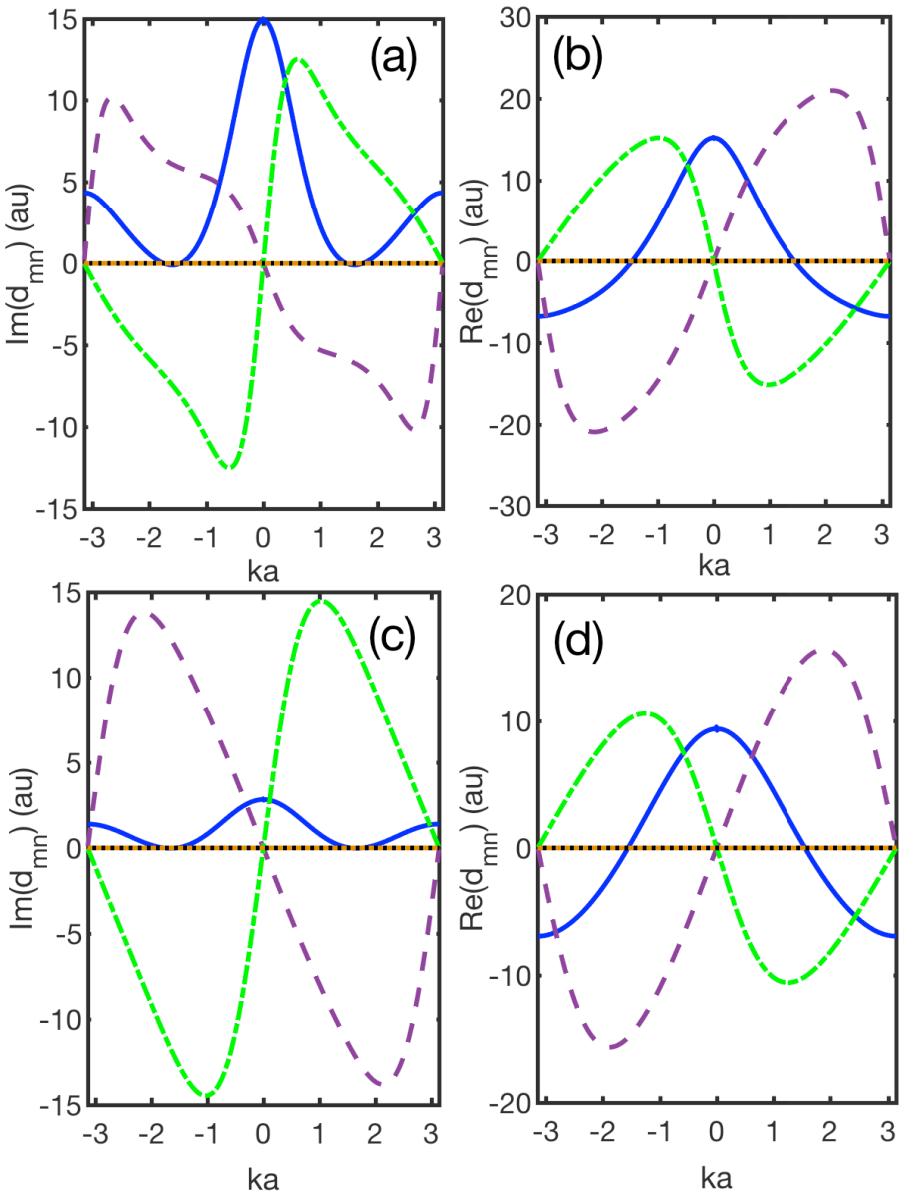

Figure 2.4: Numerical results of dipole matrix elements $d_{cv}(k)$ (solid blue lines) as well as non-zero diagonal elements $d_{cc}(k)$ (purple dashed lines) and $d_{vv}(k)$ (green dash-dotted lines) calculated using wavefunctions defined in Section 2.4 as opposed to the alternatives defined by (2.40) and given in Figure 2.3. (a) and (b) refer to real and imaginary parts of dipole matrix elements for the solid defined by $a = 8.9$ au and $\Omega = 0.9$ au ($E_g = 0.1437$ au and $2\Delta = 0.2445$ au). (c) and (d) are the real and imaginary parts for the solid defined by $a = 11.7$ au and $\Omega = 2.5$ au ($E_g = 0.1410$ au and $2\Delta = 0.0566$ au). For comparison, numerically calculated diagonal dipole elements $d_{cc}(k)$ (orange dotted lines) and $d_{vv}(k)$ (solid black lines) are also plotted for the alternative wavefunction choices of (2.40) and Figure 2.3 to demonstrate that they are equal to zero.

Chapter 3

Wannier quasi-classical method

In this Chapter we formulate an approximate Wannier quasi-classical (WQC) method of calculating interband high harmonic spectra that is valid for materials with wide energy bandwidths such as semiconductors (need large number of photons to bridge maximum and minimum energy band gaps as explained in the introduction). There are two parts in deriving this approach. The first involves transforming high harmonic interband equations from the Bloch basis of k-space to the Wannier basis of real space. This will allow for interpretation of interband HHG in terms of relative lattice site separations of electrons and holes contributing to such. The second part involves using a saddle point method of approximating integrals needed for calculating the interband current. Such saddle points describe electron-hole birth time (following ionization), recombination time and the characteristic crystal wavevector of recombination. We find that the combination of relative Wannier sites and saddle points provide for a simple quasi-classical interpretation of interband HHG for examples where the model reasonably represents fully numerical results. We demonstrate the outcome of this approach using two δ-function potential semiconductors constructed according to theory in Chapter 2.

3.1 Theoretical methods

3.1.1 Interband current in the Wannier basis

Although intraband current also contributes to HHG, in this Chapter we restrict our analysis to interband current because, as will be explained, we will be specifically applying the model to wide bandwidth materials such as semiconductors and experiments [32, 37] attribute HHG in such materials to interband mechanisms.

We begin with the interband current in terms of angular frequency ω as introduced

in the Introduction:

$$\mathbf{j}_{er}(\omega) = -i\omega \int_{-\infty}^{\infty} dt e^{-i\omega t} \left\{ \int_{BZ} d^3\mathbf{k} \mathbf{d}(\mathbf{k}) \int_{-\infty}^{t} dt' \mathbf{F}(t') \cdot \mathbf{d}^*(\boldsymbol{\kappa}_{t'}) e^{-iS(\mathbf{k},t',t)-(t-t')/T_2} + c.c. \right\}. \tag{3.1}$$

Note that just for this chapter we will be using an alternative, but valid formulation than is introduced in the introduction following the convention of the lead authour of the paper that this chapter is based on. That is, we use $\boldsymbol{\kappa}_{t'} = \mathbf{k} + \mathbf{A}(t) - \mathbf{A}(t')$ instead of $\boldsymbol{\kappa}_{t'} = \mathbf{k} + \mathbf{A}(t') - \mathbf{A}(t)$. In considering the above equation we recall that the dipole matrix elements between valence and conduction bands $\mathbf{d}(\mathbf{k}) = \mathbf{d}_{vc}(\mathbf{k})$ are given by

$$\mathbf{d}_{vc}(\mathbf{k}) = \frac{-i}{v} \int_v d^3\mathbf{x} u^*_{v,\mathbf{k}}(\mathbf{x}) \nabla_{\mathbf{k}} u_{c,\mathbf{k}}(\mathbf{x}). \tag{3.2}$$

The periodic parts of Bloch functions $u_{m,\mathbf{k}}(\mathbf{x})$ used for dipole calculations can be expressed in terms of Wannier functions [34]

$$w_m(\mathbf{x} - \mathbf{x}_j) = \frac{1}{v} \int_{BZ} u_{m,\mathbf{k}}(\mathbf{x}) e^{i\mathbf{k}\cdot(\mathbf{x}-\mathbf{x}_j)} d^3\mathbf{k}, \tag{3.3}$$

such that

$$u_{m,\mathbf{k}}(\mathbf{x}) = \sum_j w_m(\mathbf{x} - \mathbf{x}_j) e^{-i\mathbf{k}\cdot(\mathbf{x}-\mathbf{x}_j)}, \tag{3.4}$$

where $\mathbf{x}_j$ are unit cell site vectors. Of note is that if we recall from the introduction that laser dressed wavefunctions in the two-band model are given by

$$\Psi(\mathbf{x}, t) = \sum_{m=c,v} \int_{BZ} a_m(\mathbf{k}, t) \Phi_{m,\mathbf{k}}(\mathbf{x}) d^3\mathbf{k}, \tag{3.5}$$

we find that the valence band Wannier functions at $\mathbf{x}_j = 0$ are defined through these functions (assuming $a_c(\mathbf{k}, t = 0) = 0$ and $a_v(\mathbf{k}, t = 0) = 1$) as

$$w_v(\mathbf{x}) = \Psi(\mathbf{x}, t = 0) = \int_{BZ} a_v(\mathbf{k}, t = 0) \Phi_{v,\mathbf{k}}(\mathbf{x}) d^3\mathbf{k}. \tag{3.6}$$

Because all lattice sites are equivalent, it is possible to shift these Wannier functions to other sites $\mathbf{x}_j$ with no consequence on calculations to HHG by setting $a_v(\mathbf{k}, t = 0) = e^{-i\mathbf{k}\cdot\mathbf{x}_j}$. Nevertheless, we will continue to use $\mathbf{x}_j = 0$ due to its simplicity.

We now express the dipole matrix element $\mathbf{d}(\mathbf{k}) = \mathbf{d}_{vc}(\mathbf{k})$ in the Wannier basis using

the alternative dipole formula $\mathbf{d}(\mathbf{k}) = -\langle u_{v,\mathbf{k}}(\mathbf{x})|\hat{\mathbf{x}}|u_{c,\mathbf{k}}(\mathbf{x})\rangle$ and (3.4) so that

$$\mathbf{d}(\mathbf{k}) = -\frac{1}{v}\sum_{j,q}\int_v w_v^*(\mathbf{x}-\mathbf{x}_q)\{\mathbf{x}-\mathbf{x}_j\}w_c(\mathbf{x}-\mathbf{x}_j)e^{i\mathbf{k}\cdot(\mathbf{x}_j-\mathbf{x}_q)}d^3\mathbf{x}. \tag{3.7}$$

Note that the $\mathbf{x}-\mathbf{x}_j$ terms within the braces are position coordinate vectors that appear after applying the position operator $\hat{\mathbf{x}}$ within the Wannier basis. We then allow $\mathbf{x}_l = \mathbf{x}_q - \mathbf{x}_j$ to obtain

$$\mathbf{d}(\mathbf{k}) = -\frac{1}{v}\sum_{j,q}\int_v w_v^*(\mathbf{x}-\mathbf{x}_j-\mathbf{x}_l)\{\mathbf{x}-\mathbf{x}_j\}w_c(\mathbf{x}-\mathbf{x}_j)e^{-i\mathbf{k}\cdot\mathbf{x}_l}d^3\mathbf{x}. \tag{3.8}$$

Then, summation over j in the above equation leads to

$$\mathbf{d}(\mathbf{k}) = -\sum_l e^{-i\mathbf{k}\cdot\mathbf{x}_l}\frac{1}{V}\int_V w_v^*(\mathbf{x}-\mathbf{x}_l)\mathbf{x}w_c(\mathbf{x})d^3\mathbf{x} \tag{3.9}$$

$$= \sum_l \mathbf{d}_l e^{-i\mathbf{k}\cdot\mathbf{x}_l}, \tag{3.10}$$

where, due to the summation over j, we integrate over crystal volume V instead of a single cell v.

The result of (3.10) is the Fourier expansion of $\mathbf{d}(\mathbf{k})$. This means that $\mathbf{d}_l$ corresponds both to Wannier dipole moments and Fourier coefficients of $\mathbf{d}(\mathbf{k})$. As a Wannier dipole moment, the index l describes a separation of l lattice sites between an electron and hole in a transition.

Using (3.10) we can now express the interband current of (3.1) as

$$\begin{aligned}\mathbf{j}_{er}(\omega) = -i\omega\int_{-\infty}^{\infty}dt e^{-i\omega t}\Bigg\{\int_{BZ}d^3\mathbf{k}\left(\sum_j \mathbf{d}_j e^{-i\mathbf{k}\cdot\mathbf{x}_j}\right)\\ \times\int_{-\infty}^{t}dt'\mathbf{F}(t')\cdot\left(\sum_l \mathbf{d}_l^* e^{i[\mathbf{k}-\mathbf{A}(t')+\mathbf{A}(t)]\cdot\mathbf{x}_l}\right)e^{-iS(\mathbf{k},t',t)-(t-t')/T_2}+c.c.\Bigg\}\end{aligned}$$

$$\begin{aligned}= -i\omega\sum_{j,l}\int_{-\infty}^{\infty}dt e^{-i\omega t}\Bigg\{\mathbf{d}_j\mathbf{d}_l^*\int_{BZ}d^3\mathbf{k}\int_{-\infty}^{t}dt'\mathbf{F}(t')\\ \times e^{i[-S(\mathbf{k},t',t)+i(t-t')/T_2+\mathbf{k}\cdot(\mathbf{x}_l-\mathbf{x}_j)+\{\mathbf{A}(t)-\mathbf{A}(t')\}\cdot\mathbf{x}_l]}+c.c.\Bigg\}.\end{aligned} \tag{3.11}$$

This can be rewritten in a compact form as

$$\mathbf{j}_{er}(\omega) = \sum_{j,l} \mathbf{d}_j \{\mathbf{d}_l^* \cdot \mathbf{T}_{jl}(\omega)\} - \mathbf{d}_j^* \{\mathbf{d}_l \cdot \mathbf{T}_{jl}^*(-\omega)\}, \tag{3.12}$$

where

$$\mathbf{T}_{jl}(\omega) = -i\omega \int_{BZ} d^3\mathbf{k} \int_{-\infty}^{\infty} dt \int_{-\infty}^{t} dt' \mathbf{F}(t') e^{i\varphi(\mathbf{k},t',t,\mathbf{x}_l,\mathbf{x}_j)}, \tag{3.13}$$

is the propagator that quantifies the change of Wannier dipole $\mathbf{d}_l^*$ to $\mathbf{d}_j$. Its phase $\varphi(\mathbf{k}, t', t, \mathbf{x}_l, \mathbf{x}_j)$ is given by

$$\varphi(\mathbf{k}, t', t, \mathbf{x}_l, \mathbf{x}_j) = -S(\mathbf{k}, t', t) + i(t - t')/T_2 - \omega t + \mathbf{k} \cdot (\mathbf{x}_l - \mathbf{x}_j) + \{\mathbf{A}(t) - \mathbf{A}(t')\} \cdot \mathbf{x}_l. \tag{3.14}$$

Of note is that the term $\mathbf{d}_j\{\mathbf{d}_l^* \cdot \mathbf{T}_{jl}(\omega)\} = \mathbf{P}_{jl}(\omega)$ in (3.12) corresponds to the probability amplitude of an electron-hole pair with an initial separation of l lattice sites recombining j lattice sites from each other and, as a result, emitting light of angular frequency ω. That is, $\mathbf{P}_{jl}(\omega)$ (as well as $\mathbf{d}_j^*\{\mathbf{d}_l \cdot \mathbf{T}_{jl}(-\omega)\} = \mathbf{P}_{jl}^*(-\omega)$) weighs the importance of different combinations of j and l leading to emission at frequency ω. Its complex nature allows for interference between these combinations.

Equation (3.12) is now represented in the Wannier basis in a way that is ideal for approximate evaluation using the saddle point method when $e^{iS(\mathbf{k},t',t)}$ is highly oscillatory (i.e. for large bandwidth semiconductors).

3.1.2 The saddle point method of integration

We now turn to the saddle point approximation (see for example [47]) that is valid when the exponent of the classical action $e^{-iS(\mathbf{k},t',t)}$ is highly oscillatory. The classical action is given by $S(\mathbf{k}, t', t) = \int_{t'}^{t} \mathcal{E}_g(\mathbf{k} + \mathbf{A}(t) - \mathbf{A}(\tau))d\tau$ (for the convention used in the chapter). According to the action's relation to band gap, we expect that for semiconductors with increasingly large bandwidths $e^{-iS(\mathbf{k},t',t)}$ will become increasingly oscillatory, and so the saddle point approximation will become increasingly valid.

We begin by setting up saddle point equations characteristic of (3.13) by setting $\partial\varphi/\partial n = 0$ where $n = t'$, t or $\mathbf{k}$. For the variables (in the same order) these equations are given by

$$\mathcal{E}_g(\boldsymbol{\kappa}_{t',t}) + \mathbf{F}(t') \cdot \mathbf{x}_l = 0, \tag{3.15a}$$

$$\mathcal{E}_g(\mathbf{k}) - \mathbf{F}(t)\cdot\{\boldsymbol{\xi}(t',t) - \mathbf{x}_l\} = \mathcal{E}_g(\mathbf{k}) + \mathbf{F}(t)\cdot\mathbf{x}_j = \mp\omega, \tag{3.15b}$$

$$\boldsymbol{\xi}(t',t) = \mathbf{x}_l - \mathbf{x}_j, \tag{3.15c}$$

where $\boldsymbol{\kappa}_{t',t} = \boldsymbol{\kappa}_{t'} = \mathbf{k} + \mathbf{A}(t) - \mathbf{A}(t')$ and $\boldsymbol{\xi}(\mathbf{k},t',t) = \int_{t'}^{t} d\tau \mathbf{v}(\boldsymbol{\kappa}_{\tau,t})$ describes relative electron-hole motion between t' and t with band velocity difference $\mathbf{v}(\mathbf{k}) = \nabla_{\mathbf{k}}\mathcal{E}_g(\mathbf{k})$. The condition (3.15b) has $\mp\omega$ to correspond to the two the complex conjugates of each other in (3.1). Note that all results are obtained through direct differentiation of φ except for the second equality in (3.15b) that is obtained by substituting (3.15c) into the first equality of (3.15b). Also note that we have dropped dephasing time T_2, which can be done to leading order. In results at the end of this chapter we account for a short dephasing time of half a laser cycle by solving for trajectories within one laser cycle.

The equations must be solved to obtain saddle points representing electron-hole birth time t', recombination time t and the characteristic crystal momentum wavevector $\mathbf{k}$. To do this we assume that the laser field and its vector potential are linearly polarized along the x-axis and also that $k = k_x$. Let us write the saddle points as $t' = t_b + i\delta$, $t = t_r$ and $\mathbf{k} = \mathbf{k}_s$. The complex birth time $t' = t_b + i\delta$ required for solving the saddle point equations can be thought of as a reflection of the quantum mechanical nature of tunnelling (see for example [52] where an imaginary part of a birth time saddle point is interpreted as the tunelling time for HHG in gases). For a small value of δ ($|\delta| < 1$) it is possible to solve (3.15a) by Taylor expanding about $i\delta$. Doing so leads $\mathbf{k}_s = \mathbf{A}(t_b) - \mathbf{A}(t_r)$. Furthermore, assuming an approximate band gap

$$\mathcal{E}_g(\mathbf{k}) \approx E_g + \frac{1}{2}\sum_{i,j} k_i k_j \beta_{ij}(0), \tag{3.16}$$

we find that $\delta = \sqrt{\frac{2(E_g + F(t_b)x_l)}{\beta_{xx}(0)F^2(t_b)}}$, where $\beta_{ij} = \partial^2\mathcal{E}_g(k)/\partial k_i \partial k_j$ is the inverse mass tensor where $i,j = x,y,z$. In solving for δ there is a choice of sign. We chose the positive sign because it results in exponential decay of $e^{i\varphi}$. As for t_b and t_r, they are difficult to solve for using analytical techniques. Nevertheless, we can solve for them numerically by using (3.15c) to find a set of recombination times t_r that correspond to an input set of birth times t_b. The angular frequency of light emitted due to HHG is then determined by using (3.15b).

The next step is to perform approximate integration using the determined saddle points. We use a second order expansion of φ and consider the following asymptotic

through the saddle points:

$$\int_{-\infty}^{\infty} d\mathbf{q} e^{\frac{i}{2}\mathbf{q}^T H \mathbf{q}} = \frac{(\sqrt{2\pi})^5}{\sqrt{-i|H|}}, \tag{3.17}$$

where $\mathbf{q} = (t', t, k_x, k_y, k_z)$ and H is the Hessian matrix with elements give by $H_{ij} = \partial^2\varphi/\partial i \partial j$ and i, j being components of $\mathbf{q}$. The determinant of the Hessian matrix evaluated at the set of saddle points $\mathbf{q}_s$ can be shown to be given by:

$$|H| = \left| \begin{array}{ccccc} -\mathbf{F}(t')\cdot\mathbf{v}(\boldsymbol{\kappa}_{t',t}) & 0 & v_x(\boldsymbol{\kappa}_{t',t}) & v_y(\boldsymbol{\kappa}_{t',t}) & v_z(\boldsymbol{\kappa}_{t',t}) \\ +\dot{\mathbf{F}}(t')\cdot\mathbf{x}_l & & & & \\ -\mathbf{F}(t)\cdot\mathbf{v}(\boldsymbol{\kappa}_{t',t}) & -\dot{\mathbf{F}}(t)\cdot\mathbf{x}_l & -v_x(\mathbf{k}) + \sum_i & -v_y(\mathbf{k}) + \sum_i & -v_z(\mathbf{k}) + \sum_i \\ & & F_i(t)D_{ix}(t',t) & F_i(t)D_{iy}(t',t) & F_i(t)D_{iz}(t',t) \\ v_x(\boldsymbol{\kappa}_{t',t}) & -v_x(\mathbf{k}) & -D_{xx}(t',t) & -D_{xy}(t',t) & -D_{xz}(t',t) \\ v_y(\boldsymbol{\kappa}_{t',t}) & -v_y(\mathbf{k}) & -D_{yx}(t',t) & -D_{yy}(t',t) & -D_{yz}(t',t) \\ v_z(\boldsymbol{\kappa}_{t',t}) & -v_z(\mathbf{k}) & -D_{zx}(t',t) & -D_{zy}(t',t) & -D_{zz}(t',t) \end{array} \right|_{\mathbf{q}=\mathbf{q}_s}, \tag{3.18}$$

where $D_{ij}(t', t) = \int_{t'}^{t} d\tau \beta_{ij}(\boldsymbol{\kappa}_{\tau,t})$. Furthermore, if we assume a driving field of low frequency ω_0 so that $\dot{\mathbf{F}}(t) \approx 0$ and also assume charge velocity is most important along the laser polarization direction, then to the leading order the form of the Hessian determinant is $|H| = v_x(\mathbf{k}_s) f(t_b + i\delta, t_r, \mathbf{k}_s)$ [32].

Let us now express the propagator of (3.13) in terms of these results as

$$\mathbf{T}_{jl}(\omega) = \sum_{(t_b, t_r)} \mathbf{g}(t_b + i\delta, t_r) e^{-t_x} e^{-i\chi(t_b,t_r) - i\pi/4}, \tag{3.19}$$

where (t_b, t_r) refers only to ordered pairs that satisfy l, j and ω as specified in $T_{jl}(\omega)$. The functions within this equation are given by

$$\mathbf{g}(t_b + i\delta, t_r) = \omega \mathbf{F}(t_b + i\delta) \frac{(\sqrt{2\pi})^5}{\sqrt{|H|}}, \tag{3.20a}$$

$$t_x = \mathrm{Im}\{\varphi(t_b + i\delta)\} \approx \sqrt{\frac{2\{E_g + F(t_b)x_l\}^3}{\beta_{xx}(0)F^2(t_b)}}, \tag{3.20b}$$

$$\chi = \int_{t_b}^{t_r} \mathcal{E}_g(A(t_b) - A(\tau)) d\tau + \omega t_r + \mathbf{k}_s \cdot \mathbf{x}_j. \tag{3.20c}$$

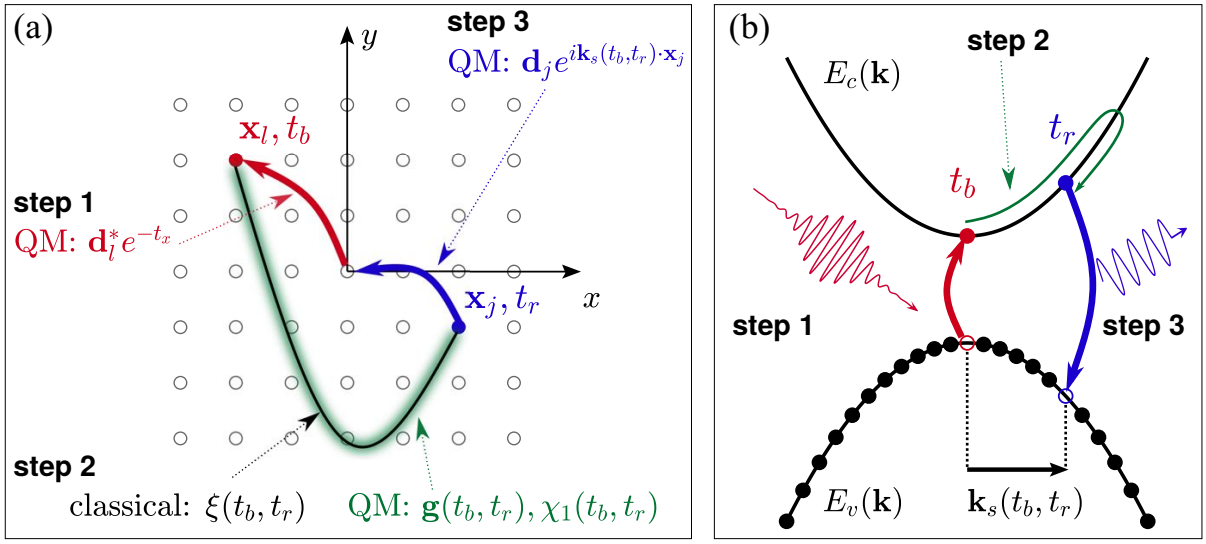

Figure 3.1: Real position space (a) and k-space (b) diagrams of the 'three-step model' interpretation of WQC equations (see text). Step 1: an electron-hole pair is born (electron promoted to conduction band) at time t_b with probability based on the dipole component d_l^* and tunnelling term e^{-t_x}. Step 2: the electron-hole pair accelerates within the laser field between times t_b and t_r. Their trajectory is described classically by $\xi(t_b, t_r)$ within real space, but $\mathbf{g}$ and χ (in particular χ_1) correspond to quantum processes. In k-space this process corresponds to the pair evolving from a zero wavevector to $\mathbf{k}_s$. Step 3: the electron-hole pair recombine at time t_r, with $\mathbf{x}_j$ (weight and phase determined by $d_j e^{i\mathbf{k}_s\cdot\mathbf{x}_j}$) separation and characteristic wavevector $\mathbf{k}_s$. As a result, light of frequency ω is emitted with energy determined by the band gap $\mathcal{E}_g(\mathbf{k}_s)$ and also (not shown) by $\mathbf{F}(t_r)\cdot\mathbf{x}_j$.

Of the functions in (3.20), t_x refers to exponential decay and $i\chi$ refers to the imaginary phase of propagator terms. Of note is how t_x has dependence on electron birth time t_b and electron-hole lattice site separation index l. It can therefore be thought of as weighing various electron-hole creation processes. In it, the term $E_g+F(t_b)x_l$ indicates the ionization potential barrier that must be overcome for the given electron-hole configuration and the denominator consists of a combination of solid state ($\beta_{xx}(0)$) and field ($F^2(t_b)$) properties besides the ionization potential that further affect the tunnelling process.

The imaginary phase $i\chi$ corresponds to interference between different trajectories associated with the specifications of $\mathbf{T}_{jl}(\omega)$. Unlike t_x it reflects processes not only occurring at birth time t_b, but also the end result of a collision process where an electron and a hole recombine at time t_r, $\mathbf{x}_j$ lattice sites apart, with a characteristic crystal momentum wavevector of $\mathbf{k}_s$. For interpretation purposes χ can be rewritten as $\chi = \chi_1 + \chi_2$ where $\chi_1 = \int_{t_b}^{t_r} \mathcal{E}_g(A(t_b) - A(\tau))d\tau + \omega t_r$ and $\chi_2 = \mathbf{k}_s \cdot \mathbf{x}_j$. χ_1 corresponds to phase acquired between t_b and t_r due to the action and harmonic frequency ω. χ_2 is associated with the recombination wavevector and electron-hole separation. It results from the change of Bloch $\mathbf{k}$-space dipole elements to Wannier dipole elements.

The above equations therefore provide an approximate method of calculating interband HHG. To the extent of its validity, the fact that the model is defined in terms of birth and recombination electron-hole lattice site separations $\mathbf{x}_l$ and $\mathbf{x}_j$, as well as characteristic saddle points $t_b + i\delta$ (birth time), t_r (recombination time) and $\mathbf{k}_s$ (characteristic crystal momentum wavevector) allows for intuition of processes leading to interband HHG. Let us now outline a 'three-step model' characteristic of these results. In doing so, we take the origin to be the lattice site at which electron is initially found in its valence band (all lattice sites are equivalent). The three steps are (see Figure 3.1):

1. Ionization: At birth time t_b an electron tunnels to the conduction band at site x_l leaving a hole in the valence band behind. As mentioned, the tunnelling process is weighted by t_x, but as seen in (3.12), the Wannier dipole element d_l also influences such.

2. Acceleration: the electron-hole pair accelerates within the laser field before recombination. Understanding how this occurs specifically between times t_b and t_r is less important than the initial and end conditions corresponding to the set of saddle points $\mathbf{q}_s$ and the Wannier lattice sites. The path the electron and hole pair take can be characterized by (3.15c) as $\boldsymbol{\xi}(t_b, t_r)$. This path can be thought of in a generally classical sense. Nevertheless, quantum interference still has influence on the electron-hole pair's propagation before recombination. As previously mentioned, χ has an influence on such (in particular χ_1 for this step), as well as the prefactor of the propagator $\mathbf{g}$ (see (3.20a)). In reciprocal space the process of acceleration is characterised by change of the crystal momentum wavevector from $\mathbf{0}$ to the eventual saddle point wavevector $\mathbf{k}_s$.

3. Recombination: finally the pair recombines at time t_r with a Wannier lattice site separation of $\mathbf{x}_j$. The probability amplitude associated with a recombination configuration is $d_j e^{i\mathbf{k}_s \cdot \mathbf{x}_j}$. The energy of harmonic radiation emitted is characterised by the band gap energy $\mathcal{E}_g(\mathbf{k}_s)$ and the term $\mathbf{F}(t_r) \cdot \mathbf{x}_j$ (see (3.15b)) due to electron-hole separation within the field of the laser.

3.2 Results

3.2.1 Wannier transition dipole components

To evaluate the functionality of the WQC approximation's harmonic spectra we model semiconductors using the δ-function potential model in Chapter 2. We use the nearest neighbour model $\mathcal{E}_g(k) = E_g + \Delta\{1 - \cos(ka)\}$ and the dipole matrix element of (2.43).

The semiconductors we consider are defined by the same lattice parameter value $a = 7$ au and different barrier strengths $\Omega = 0.5,\ 1.5$ au. In the same order, these barrier strengths correspond to minimum band gaps of $E_g = 0.1414,\ 0.2691$ au; and bandwidths $2\Delta = 0.5379,\ 0.3399$ au. Noting that the barrier strength of $\Omega = 1.5$ au is the greatest, confinement of its wavefunctions in individual unit cells should be greater. For this reason we expect faster fall-off of its Wannier dipole components than with the solid with $\Omega = 0.5$ au.

In Figure 3.2 we observe the transformation from the dipole defined in (2.43) within k-space to real space defined Wannier dipole components for the solids mentioned above. We observe, as we expect, that the narrower bandwidth material that is more confined with $\Omega = 1.5$ au has faster fall-off of Wannier dipole components in real space than is the case for the solid with $\Omega = 0.5$ au. This corresponds expectedly with the greater spread of the tightly bound semiconductor's dipole in k-space because Wannier dipole components are Fourier coefficients of the Bloch basis dipole moments.

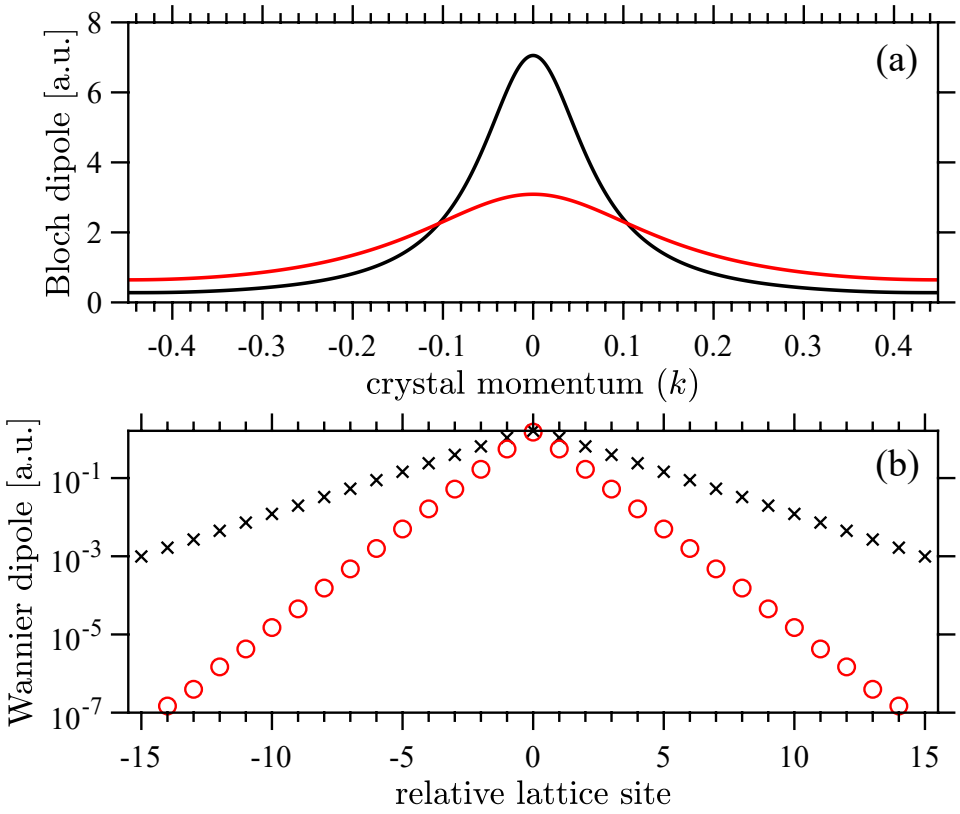

Figure 3.2: Transformation from dipole matrix elements $\mathrm{Im}(d_{cv}(k))$ defined in the Bloch basis (a) (see (2.43)) to those defined in the Wannier basis d_j. The black lines in (a) and the black crosses in (b) refer to refer to a solid with $a = 7$ au and $\Omega = 0.5$ au ($E_g = 0.1414$ au, $2\Delta = 0.5379$ au). Red lines in (a) and red circles in (b) refer to a more tightly bound solid with $a = 7$ au and $\Omega = 1.5$ au ($E_g = 0.2691$ au and $2\Delta = 0.3399$ au).

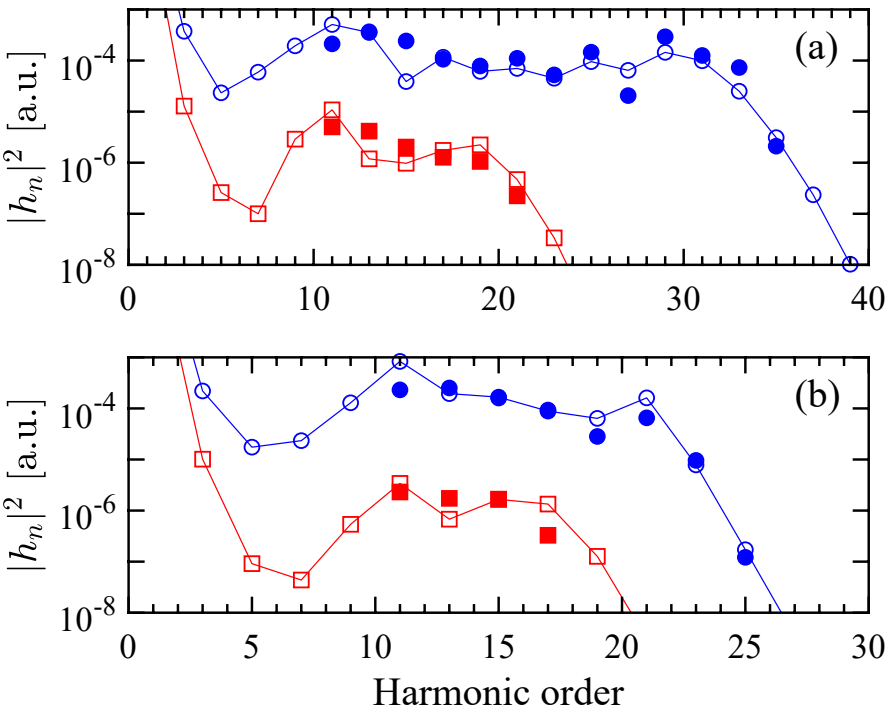

Figure 3.3: Harmonic yield spectra for δ-function potential semiconductors with lattice parameter $a = 7$ au and barrier strengths $\Omega = 0.5$ au (blue circles; $E_g = 0.1414$ au, $2\Delta = 0.5379$ au) and $\Omega = 1.5$ au (red squares; $E_g = 0.2691$ au and $2\Delta = 0.3399$ au). Filled shapes refer to the WQC approximation while empty shapes connected with lines refer to the 'exact' approach. In (a) the field amplitudes are $F_0 = 0.0025$, 0.008 au; and the laser carrier angular frequencies are $\omega_0 = 0.01425$, 0.0285 au for $\Omega = 0.5$, 1.5 au respectively. In (b) $F_0 = 0.0015$, 0.005 au; $\omega_0 = 0.01425$, 0.0285 au corresponding to $\Omega = 0.5$, 1.5 au. Field parameters are chosen to correspond to a range that could be experimentally relevant. A dephasing time of $T_2 = \pi/\omega_0$ is implemented.

3.2.2 WQC harmonic spectra

We next consider high harmonic spectra calculated using the WQC approximation for the two solids as specified above for experimentally relevant field carrier amplitude and frequency parameters. We consider such in comparison to 'exact' numerical results in Figure 3.3. In both we use a half-cylce dephasing time of $T_2 = T_0/2 = \pi/\omega_0$ so that only electron-hole recombination events within the cycle duration $T_0 = 2\pi/\omega_0$ are relevant with the WQC approach (WQC trajectories are numerically calculated using standard root-finding algorithms with regards to saddle point equations). The 'exact' numerical results are calculated by direct numerical integration of (3.1) (using trapezoidal integration as well as fast Fourier transformation of the final integral). For such we assume a laser field with a Gaussian envelope and sine carrier of $F(t) = F_0 \sin(\omega_0 t) e^{-(t/\tau)^2}$. Here we assume an envelope time constant $\tau = 40T_0$ so that the Gaussian envelope is much longer than a carrier cycle so that the field has characteristics approaching those of a continuous wave

(CW). With this temporal profile we calculate harmonic yields for angular frequencies at and around odd harmonics corresponding to

$$|h_n|^2 = \int_{(n-1/2)\omega_0}^{(n+1/2)\omega_0} d\omega |j_{er}(\omega)|^2. \tag{3.21}$$

As for spectra of the WQC approximation we use, for simplicity, a CW of the form $F(t) = F_0 \sin(\omega_0 t)$. Because of this we calculate harmonic yield from a finite Fourier series integral rather than a Fourier transform integral for the integral over t in (3.1) or the propagator (3.13) that we use. In doing so we must consider angular frequencies of light emitted as discrete integer multiples n of ω_0 rather than being within a continuous range. Furthermore, we modify g to $g/(2\pi T_0)$. The divisor 2π is implemented because we are using a 1D model, and the divisor T_0, required of Fourier series, means we are now calculating yield $|h_n|^2$ rather than $|j_{er}(n\omega_0)|^2$ (this can be verified by observing that units of the result are not equal to those of $|j_{er}(\omega)|^2$ calculated using Fourier transform formalism).

Considering the results of the spectra in Figure 3.3 we observe in all configurations reasonable agreement between 'exact' and WQC results within the most relevant region of study of the high harmonic plateau region where the WQC approach was applied. Nevertheless, some amount of discrepancy is seen between the spectra for certain harmonic orders such as $n = 15$ for the less tightly bound semiconductor with $\Omega = 0.5$ au for $F_0 = 0.0025$ au as shown by blue circles in Figure 3.3a. Higher order saddle point expansions than second order are likely needed to mediate this. Despite these errors, the reasonable agreement between 'exact' and WQC approximated results demonstrates that the simple 'three-step' quasi-classical interpretation is often sufficient for semiconductors.

We therefore find the WQC to be a useful approximation and method for interpreting HHG in semiconductors. Nevertheless, we seek to understand processes leading to HHG in other classes of materials including low bandwidth dielectrics that do not allow for a saddle point approximation. We take up the first steps of this endeavour in the next Chapter.

Chapter 4

Virtual and resonant ionization processes

When considering high harmonic generation in solids there is a lack of discussion as to whether resonant as well as non-resonant valence-conduction band transitions are most important. HHG in solids can be explained due to a resonant transition where an electron-hole pair is born in the first step (see Chapter 3 as well as, for example, references: [33,35]). However, as will be seen, non-resonant, or virtual transitions are also important. They result from electric field induced distortions of the ground state. They correspond to transitions to the conduction band that do not obey principles of energy conservation, and so virtual conduction band population vanishes at the end of a laser pulse. In this section we acknowledge the presence of both resonant and non-resonant processes as drivers of HHG. Furthermore, we will evaluate the weight of resonant vs. non-resonant transitions for both interband and intraband harmonic contributions. In addition, semiconductors often to have small minimum band gaps relative to dielectrics and as a result, to make strong field processes possible we need fewer photons so that longer wavelengths need to be used relative to dielectrics to bridge the maximum and minimum band gaps. Semiconductors therefore tend to have effectively wider bandwidths than dielectrics. We will therefore extend our study to wide bandwidth materials such as semiconductors and narrow bandwidth materials like dielectrics.

4.1 Theoretical methods

In order to consider the relevance of resonant and non-resonant valence-conduction band transition processes (we hereby refer to as ionization processes) leading to HHG due to interband and intraband currents in direct band gap materials of differing bandwidths we seek to expand time-dependent processes relating to ionization into constituent frequencies. For simplicity we consider 1D δ-function potential solids (see Chapter 2) and use a CW

field of the form $F(t) = F_0 \sin(\omega_0 t)$ and we will Fourier expand ionization processes in terms of integer multiples of the laser angular frequency ω_0. By determining which of these frequency multiples are resonant and which are not we can obtain insight into the importance of resonant vs. non-resonant processes.

4.1.1 Interband current

Expression for interband HHG in terms of ionization and propagation processes

We begin with the 1D interband current of (1.9b) in terms of $K = k - A(t)$ and in terms of observation time t:

$$j_{er}(t) = \frac{d}{dt} \int_{-\pi/a - A(t)}^{\pi/a - A(t)} dK d(K + A(t)) \int_{-\infty}^{t} dt' F(t') d^*(K + A(t')) e^{-iS(K,t',t) - (t-t')/T_2} + c.c.,$$

where

$$S(K, t', t) = \int_{t'}^{t} \mathcal{E}_g(K + A(\tau)) d\tau. \tag{4.1}$$

Here we use the band gap

$$\begin{aligned} \mathcal{E}_g(K + A(t)) =& E_g + \Delta \{1 - \cos[a(K + A(t))]\} && (4.2) \\ =& E_g + \Delta \{1 - \cos(Ka)\cos(A(t)a) - \sin(Ka)\sin(A(t)a)\}. && (4.3) \end{aligned}$$

Assuming a monochromatic CW laser field of the form $F(t) = F_0 \sin(\omega_0 t)$ that has a vector potential of the form $A(t) = (F_0/\omega_0)\cos(\omega_0 t)$ we can separate the band gap into a sinusoidally time varying part $R(K, t)$ and a non-sinusoidal stationary part $\mathcal{E}_{ns}(K)$. This is done through Jacobi-Anger expansions:

$$\cos(z\cos\theta) = J_0(z) + 2\sum_{q=1}^{\infty} (-1)^q J_{2q}(z)\cos(2q\theta), \tag{4.4a}$$

$$\sin(z\cos\theta) = 2\sum_{q=0}^{\infty} (-1)^q J_{2q+1}(z)\cos[(2q+1)\theta], \tag{4.4b}$$

(see [53]) applied to $\cos(A(t)a)$ and $\sin(A(t)a)$. In doing so we obtain

$$\mathcal{E}_g(K + A(t)) = \mathcal{E}_{ns}(K) - R(K, t), \tag{4.5}$$

where

$$\mathcal{E}_{ns}(K) = E_g + \Delta\left(1 - J_0\left(\frac{\omega_b}{\omega_0}\right)\cos(Ka)\right), \tag{4.6a}$$

$$R(K,t) = \Delta\left(\bar{C}(t)\cos(Ka) + \bar{S}(t)\sin(Ka)\right), \tag{4.6b}$$

with the Bloch frequency $\omega_b = F_0 a$ and expansion terms (relating to $\cos(A(t)a)$ and $\sin(A(t)a)$ respectively) can be written as

$$\bar{C}(t) = 2\sum_{q=1}^{\infty}(-1)^q J_{2q}\left(\frac{\omega_b}{\omega_0}\right)\cos(2q\omega_0 t), \tag{4.7a}$$

$$\bar{S}(t) = -2\sum_{q=0}^{\infty}(-1)^q J_{2q+1}\left(\frac{\omega_b}{\omega_0}\right)\cos((2q+1)\omega_0 t). \tag{4.7b}$$

Using (4.5) and decomposing the action integral of (4.1) into two integrals with upper limits of t and t' we obtain an alternate form of the interband current

$$j_{er}(t) = \frac{d}{dt}\int_{-\pi/a}^{\pi/a} dK d(K + A(t)) e^{i\int_0^t R(K,\tau)d\tau} e^{-i\mathcal{E}_{ns}(K)t - t/T_2} \times \int_{-\infty}^{t} dt' F(t') d^*(K + A(t')) e^{-i\int_0^{t'} R(K,\tau)d\tau} e^{i\mathcal{E}_{ns}(K)t' + t'/T_2} + c.c. \tag{4.8}$$

We have dropped the $A(t)$ in the limits of the integral over K because of Bloch periodicity (all functions of K repeat over an interval of length $2\pi/a$).

The interband current as expressed in (4.8) now consists of periodically time varying parts that are separate from non-periodic parts. Following methodology developed by Keldysh for optical field ionization of atoms and solids as in references [36, 48], it is therefore advantageous to Fourier expand the periodic parts into integer multiples of the laser angular frequency ω_0. We do this by letting

$$L(K,t) = d^*(K + A(t)) e^{-i\int_0^t R(K,\tau)d\tau}. \tag{4.9}$$

By Fourier expanding this periodic function in time we can represent it in a new way as

$$L(K,t) = \sum_{m=-\infty}^{\infty} L_m(K) e^{im\omega_0 t}, \tag{4.10}$$

where

$$L_m(K) = \frac{1}{T_0}\int_0^{T_0} L(K,t)e^{-im\omega_0 t}dt \tag{4.11}$$

refers to the corresponding Fourier coefficients. We can now use (4.10) alongside (4.8). With the new formulation in terms of Fourier coefficients as in (4.11) we will now switch to the angular frequency domain. To achieve this we use a Fourier coefficient integral over a single cycle of observation time t due to signal periodicity. In doing so we extract current corresponding to integer harmonics $j = \omega/\omega_0 \in \mathbb{Z}$. In following these steps we obtain

$$h_{er}(j\omega_0) = \frac{ij\omega_0^2 F_0}{4\pi}\sum_{l=-\infty}^{\infty}\sum_{n=-\infty}^{\infty}\int_{-\pi/a}^{\pi/a} dK \int_0^{T_0} dt e^{-ij\omega_0 t}\Bigg\{ iL^*_{-l}(K)\left\{L_{n-1}(K) - L_{n+1}(K)\right\} \\ \times e^{-i\tilde{\beta}_{-l}(K)t}\int_{-\infty}^{t} dt' e^{i\tilde{\beta}_n(K)t'} + c.c.\Bigg\}, \tag{4.12}$$

where $\tilde{\beta}_n(K) = \beta_n(K) - i/T_2 = \mathcal{E}_{ns}(K) + n\omega_0 - i/T_2$, n corresponds to ionization (or probability amplitude integration variable t' associated) angular frequency channels and l corresponds to propagation (or current observation time t) integer angular frequency channels. Of note is that we absorbed the exponentials of $F(t') = F_0\{e^{i\omega_0 t'} - e^{-i\omega_0 t'}\}/2i$ into the ionization Fourier coefficient $L_n(K)$ to form the difference $\{L_{n-1}(K) - L_{n+1}(K)\}$. Also note that we denoted the result as $h_{er}(j\omega_0)$ instead of $j_{er}(j\omega_0)$. This is because by using a Fourier series integral instead of a Fourier transform integral as in (1.10b) there is a factor of $1/T_0$ we introduce such that $h_{er}(j\omega_0)$ can be thought of as a time averaged current that has units that differ from Fourier transform current $j_{er}(\omega)$.

We now write (4.12) fully including the complex conjugate terms in braces as:

$$h_{er}(j\omega_0) = \frac{ij\omega_0^2 F_0}{4\pi}\sum_{l=-\infty}^{\infty}\sum_{n=-\infty}^{\infty}\int_{-\pi/a}^{\pi/a} dK \int_0^{T_0} dt e^{-ij\omega_0 t} \\ \times\Bigg\{ iL^*_{-l}(K)\left\{L_{n-1}(K) - L_{n+1}(K)\right\} e^{-i\tilde{\beta}_{-l}(K)t}\int_{-\infty}^{t} dt' e^{i\tilde{\beta}_n(K)t'} \\ -iL_l(K)\left\{L^*_{-1-n}(K) - L^*_{1-n}(K)\right\} e^{i\tilde{\beta}^*_l(K)t}\int_{-\infty}^{t} dt' e^{-i\tilde{\beta}^*_{-n}(K)t'}\Bigg\}. \tag{4.13}$$

Note that in the complex conjugate term we have taken the transform of a complex

conjugate time signal. As a result we obtain in (4.13),

$$L^*_{-m}(K) = \frac{1}{T_0}\int_0^{T_0} L^*(K,t)e^{-im\omega_0 t}dt, \tag{4.14}$$

which explains the flipped signs of the indices in the last line.

We will use an alternative convention where we reverse summation indices in the conjugate term (following the minus sign). This is of no consequence due to the infinite summation limits. This will be of convenience for defining resonant and virtual ionization channels, as will be explained. Doing so leads to

$$\begin{aligned} h_{er}(j\omega_0) = \frac{ij\omega_0^2 F_0}{4\pi}\sum_{l=-\infty}^{\infty}\sum_{n=-\infty}^{\infty}\int_{-\pi/a}^{\pi/a}dK\int_0^{T_0}dte^{-ij\omega_0 t} \\ \times\Bigg\{iL^*_{-l}(K)\left\{L_{n-1}(K)-L_{n+1}(K)\right\}e^{-i\tilde{\beta}_{-l}(K)t}\int_{-\infty}^{t}dt'e^{i\tilde{\beta}_n(K)t'} \\ -iL_{-l}(K)\left\{L^*_{n-1}(K)-L^*_{n+1}(K)\right\}e^{i\tilde{\beta}^*_{-l}(K)t}\int_{-\infty}^{t}dt'e^{-i\tilde{\beta}^*_n(K)t'}\Bigg\}. \end{aligned} \tag{4.15}$$

Note that e^{t'/T_2} can be extracted from both $e^{i\tilde{\beta}_n(K)t'}$ and $e^{-i\tilde{\beta}^*_n(K)t'}$. Therefore, if we assume a finite dephasing time T_2 so that $\lim_{t'\to-\infty}e^{t'/T_2}=0$, it becomes possible to evaluate the two temporal integrals of (4.12) to obtain

$$\begin{aligned} h_{er}(j\omega_0) = \frac{\pi ijF_0}{T_0}\sum_{n=-\infty}^{\infty}\int_{-\pi/a}^{\pi/a}dK\Bigg\{\frac{L^*_{n-j}(K)[L_{n-1}(K)-L_{n+1}(K)]}{\tilde{\beta}_n(K)} \\ +\frac{L_{n+j}(K)[L^*_{n-1}(K)-L^*_{n+1}(K)]}{\tilde{\beta}^*_n(K)}\Bigg\}. \end{aligned} \tag{4.16}$$

Of note is that we have used orthogonality relations of the form

$$\frac{1}{T_0}\int_0^{T_0}e^{im\omega_0 t}e^{-i\mu\omega_0 t}dt = \delta_{m,\mu}, m,\mu\in\mathbb{Z} \tag{4.17}$$

to express the propagation channel indices in terms of ionization channel indices n and harmonic orders j.

Classification of ionization channels

Equation (4.16) is in a form that allows us to classify different ionization processes leading to interband HHG. Of note is that for the integration interval $K\in[-\pi/a,\pi/a]$, the terms $1/\tilde{\beta}_n(K)=(\beta_n(K)-i/T_2)^{-1}$ and $1/\tilde{\beta}^*_n(K)=(\beta_n(K)+i/T_2)^{-1}$ are maximized for

ionization channels n that can fulfill the conservation condition $\beta_n(\pm K_n) = \mathcal{E}_{ns}(\pm K_n) + n\omega_0 = 0$, for some $K_n \in [0, \pi/a]$. We therefore consider resonant ionization channels to be ones that fulfill this condition (see also Figure 4.1) and those that do not to be virtual channels. Of note is that the summation convention we are using as in (4.15) allows us to define all resonant channels using this same constraint, as opposed to the convention of (4.13) where resonant processes would be more difficult to isolate.

Following the approach in [36], we can determine the set of all resonant channels by writing the condition again using (4.6a):

$$E_g + \Delta\left(1 - J_0\left(\frac{\omega_b}{\omega_0}\right)\cos(\pm K_n a)\right) + n\omega_0 = 0. \tag{4.18}$$

We seek $K_n \in \mathbb{R}$ that satisfy this. For real arguments, $\cos(\pm K_n) \in [-1, 1]$. Using this constraint we obtain the set of all resonant ionization channels as

$$N_r = \left\{n \in \mathbb{Z} | n_r^{\min} \leq n \leq n_r^{\max}\right\}, \tag{4.19}$$

where

$$n_r^{\min} = -\left\lfloor \frac{E_g + \Delta\left(1 + \left|J_0\left(\frac{\omega_b}{\omega_0}\right)\right|\right)}{\omega_0} \right\rfloor \tag{4.20a}$$

$$n_r^{\max} = -\left\lceil \frac{E_g + \Delta\left(1 - \left|J_0\left(\frac{\omega_b}{\omega_0}\right)\right|\right)}{\omega_0} \right\rceil \tag{4.20b}$$

are the minimum (maximum magnitude) and maximum (minimum magnitude) resonant ionization channels respectively. Similar results are obtained in [36].

The total number of different resonant ionization channels $n_r^{\max} - n_r^{\min}$ is controlled by both laser and field parameters as $\mathcal{E}_{ns}(K)$ is a laser dressed band gap that changes dynamically with field. The simplest way to increase the number of resonant channels is by decreasing the laser frequency ω_0, but finding a solid that has a wide bandwidth 2Δ relative to another solid (e.g. a semiconductor compared to a dielectric) will also allow for an increase in resonant channels. The ratio $\omega_b/\omega_0 = F_0 a/\omega_0$ often must be small enough to support any integer resonant ionization channels because of how the Bessel function $J_0(\theta)$ damps out as its argument θ increases. Nevertheless, $J_0(\theta)$ oscillates through zeroes so that there are particular values of the ratio ω_b/ω_0 that completely close all resonant ionization channels.

In Figure 4.1 we consider examples of processes associated with resonant and virtual channels n for a 1D δ-function potential solid defined by parameters: $a = 8.9$ au, $\Omega = 0.9$ au, $E_g = 0.1437$ au and $2\Delta = 0.2445$ au. A sine field of the form $F(t) = F_0 \sin(\omega_0 t)$ is used with $F_0 = 0.003$ au and $\omega_0 = E_g/7$. Figure 4.1a and Figure 4.1b correspond to two different processes associated with a given channel n and have arrows colour coded according to (4.16) rewritten there. Purple arrows correspond to propagation energy difference required to reach harmonic order $j = 9$.

We observe that a process associated with n (blue arrows) in Figure 4.1a is associated with a change of energy $n\omega_0$ (weighted according to $[L_{n-1}(K) - L_{n+1}(K)]/\tilde{\beta}_n(K)$) and that one (red arrows) in Figure 4.1b is associated with change $-n\omega_0$ (weighted according to $[L^*_{n-1}(K) - L^*_{n+1}(K)]/\tilde{\beta}^*_n(K)$). That is, for a resonant channel (like $n = -10$ shown), where n is negative, the process of Figure 4.1a corresponds to resonant de-excitation while that in Figure 4.1b corresponds to resonant excitation. We note that the arrows in parts a and b corresponding to a resonant process like $n = -10$ would be reversed for its opposite sign ($n = 10$). Nevertheless, we do not consider the opposite sign ($n = 10$) process as being resonant because it does not satisfy: $\beta_n(\pm K_n) = \mathcal{E}_{ns}(\pm K_n) + n\omega_0 = 0$, for some $K_n \in [0, \pi/a]$. Other examples of $n = -5$ and $n = 4$ that more clearly do not satisfy this condition are shown in Figure 4.1.

Considering the examples of propagation energy differences (purple arrows) in Figure 4.1 needed to reach fixed harmonic order $j = 9$, we note that for a given channel value n, these processes are weighted by $L^*_{n-j}(K)$ and $L_{n+j}(K)$ for processes in Figure 4.1a and Figure 4.1b respectively. Note the dependence of the Fourier coefficients $L_m(K)$ on bandwidth dependent variables $d(K + A(t))$ (see Chapter 2 and in particular (2.43)) and $\int_0^t d\tau R(K, \tau)$ from the Fourier coefficient definitions in (4.11) and (4.9). Because of this we expect that propagation processes with energy magnitudes that vastly exceed the bandwidth are not supported and therefore have low probabilities of occurrence. This is important in considering the weight of the process in Figure 4.1a vs. Figure 4.1b for a particular channel n. For the resonant channel of $n = -10$, for example, we expect the process in Figure 4.1a to be less important because of the large amount of propagation energy change required to reach $j = 9$ compared to that in Figure 4.1b.

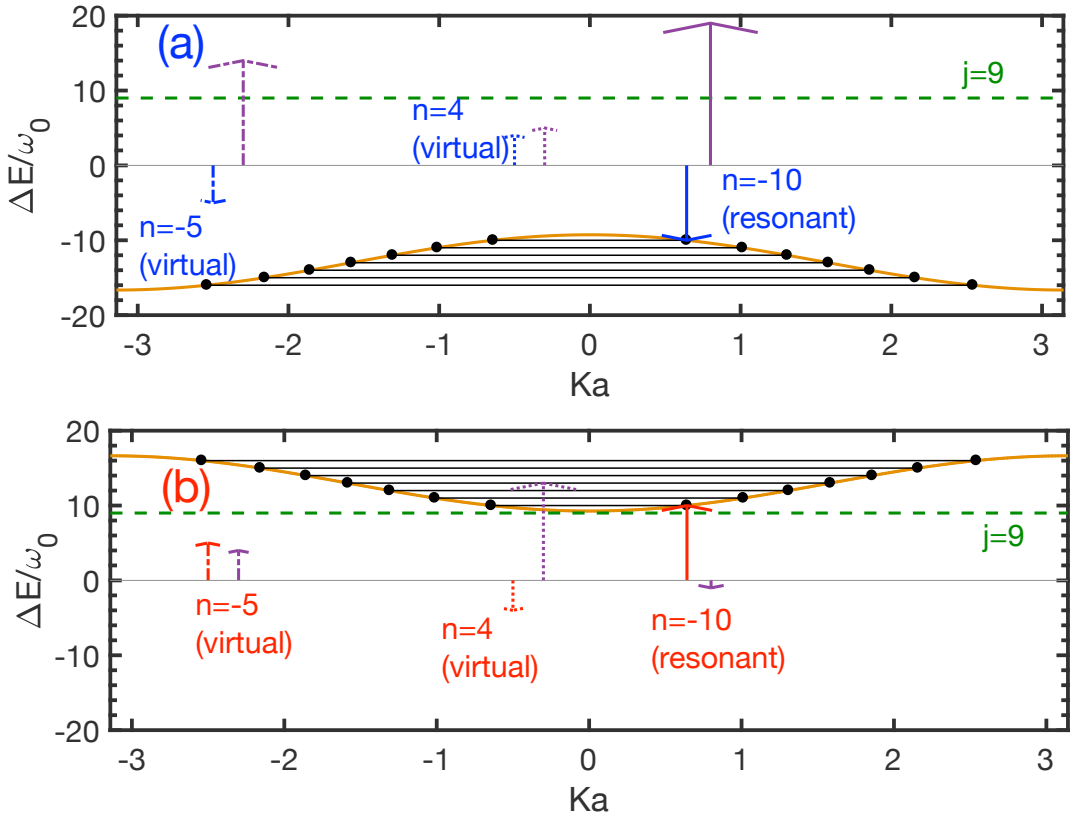

$$h_{er}(j\omega_0) = \frac{\pi i j F_0}{T_0} \sum_{n=-\infty}^{\infty} \int_{-\pi/a}^{\pi/a} dK \left\{ \frac{L^*_{n-j}(K)[L_{n-1}(K) - L_{n+1}(K)]}{\tilde{\beta}_n(K)} + \frac{L_{n+j}(K)[L^*_{n-1}(K) - L^*_{n+1}(K)]}{\tilde{\beta}^*_n(K)} \right\}$$

Figure 4.1: Examples of resonant and virtual interband ionization processes for a 1D δ-function potential solid with parameters: $a = 8.9$ au, $\Omega = 0.9$ au, $E_g = 0.1437$ au and $2\Delta = 0.2445$ au. A sine field of the form $F(t) = F_0 \sin(\omega_0 t)$ is used with $F_0 = 0.003$ au and $\omega_0 = E_g/7$. Energy changes (ΔE) of two processes associated with a given channel n are shown in (a) and (b) as blue and red arrows and are colour coded according to blue and red parts of (4.16) rewritten here. Of these processes, dash-dotted and dotted arrows refer to virtual processes while solid arrows refer to resonant processes. For each, a purple arrow indicates the propagation energy difference required to reach the fixed harmonic order $j = 9$ (green dashed line) for the given ionization process. For parts (a) and (b) either $\pm\mathcal{E}_{ns}(K)/\omega_0$ is shown in orange with black lines and dots corresponding to energy changes (ΔE) of resonant processes.

4.1.2 Intraband current

Expression for intraband HHG in terms of ionization processes

We start with the following expression of time-dependent intraband current in terms of $K = k - A(t)$ from the density matrix approach as in (1.9a) in the introduction:

$$j_{ra}(t) = \int_{\frac{-\pi}{a}}^{\frac{\pi}{a}} dK v[K + A(t)] \int_{-T'}^{t} dt' F(t') d[K + A(t')] \times \int_{-T''}^{t'} dt'' F(t'') d^*[K + A(t'')] e^{-iS(K,t'',t') - \frac{(t'-t'')}{T_2}} + c.c. \quad (4.21)$$

Here shifts on Brillouin zone limits of $-A(t)$ have been dropped because of Bloch periodicity. The lower limits on the two temporal integrals are chosen to be $-T''$ and $-T'$ instead of $-\infty$. We do this because the infinite limits pose limitations on the calculation with the assumptions we will be using of a monochromatic CW laser field of the form $F(t) = F_0 \sin(\omega_0 t)$ and a finite dephasing time T_2. Such limitations are due to divergence of e^{-t'/T_2} as $t' \to -\infty$ as well as phase indeterminacy of the monochromatic field in that limit.

Following the steps of section 4.1.2 involving Jacobi-Anger expansion of the action integral as well as Fourier expansions defined through equations (4.9) to (4.11) we rewrite the intraband current of (4.21) in full as

$$j_{ra}(t) = -\frac{F_0^2}{4} \sum_{\nu=-\infty}^{\infty} \sum_{n=-\infty}^{\infty} \left\{ \int_{-\frac{\pi}{a}}^{\frac{\pi}{a}} dK v[K + A(t)] \int_{-T'}^{t} dt' \left\{ L^*_{-1-\nu}(K) - L^*_{1-\nu}(K) \right\} \times e^{-i\tilde{\beta}_{-\nu}(K)t'} \int_{-T''}^{t'} dt'' \left\{ L_{n-1}(K) - L_{n+1}(K) \right\} e^{i\tilde{\beta}_n(K)t''} + \int_{-\frac{\pi}{a}}^{\frac{\pi}{a}} dK v[K + A(t)] \times \int_{-T'}^{t} dt' \left\{ L_{\nu-1}(K) - L_{\nu+1}(K) \right\} e^{i\tilde{\beta}^*_{\nu}(K)t'} \int_{-T''}^{t'} dt'' \left\{ L^*_{-1-n}(K) - L^*_{1-n}(K) \right\} e^{-i\tilde{\beta}^*_{-n}(K)t''} \right\}, \quad (4.22)$$

where n and ν correspond to ionization channel indices from Fourier expansion in the t'' and t' time variables respectively. Both t'' and t' are integration variables that result in transition probability. This is in contrast to interband current that has only one integration variable over t' for transition amplitude leading to only one summation index n in the Fourier series formalism. Although we do not do this here, $v[K + A(t)]$ can also be Fourier expanded with Fourier coefficients integrated over t such that velocity channels can be defined.

We now rewrite (4.22) with an alternative summation convention where we let $\nu \to -\nu$

in the first term in braces and $n \to -n$ for the second term in braces. As result of this change we obtain:

$$j_{ra}(t) = -\frac{F_0^2}{4}\sum_{\nu=-\infty}^{\infty}\sum_{n=-\infty}^{\infty}\Bigg\{\int_{-\frac{\pi}{a}}^{\frac{\pi}{a}} dK v[K+A(t)]\int_{-T'}^{t} dt'\left\{L^*_{\nu-1}(K)-L^*_{\nu+1}(K)\right\}$$
$$\times e^{-i\tilde{\beta}_\nu(K)t'}\int_{-T''}^{t'} dt''\left\{L_{n-1}(K)-L_{n+1}(K)\right\}e^{i\tilde{\beta}_n(K)t''} + \int_{-\frac{\pi}{a}}^{\frac{\pi}{a}} dK v[K+A(t)]$$
$$\times\int_{-T'}^{t} dt'\left\{L_{\nu-1}(K)-L_{\nu+1}(K)\right\}e^{i\tilde{\beta}^*_\nu(K)t'}\int_{-T''}^{t'} dt''\left\{L^*_{n-1}(K)-L^*_{n+1}(K)\right\}e^{-i\tilde{\beta}^*_n(K)t''}\Bigg\}. \tag{4.23}$$

This is of no consequence because of the infinite summation limits. We have chosen to use the given summation convention as it will later provide convenience in considering resonant vs. non-resonant ionization processes. In much of the analysis that follows we abbreviate the second term in braces of (4.23) as *c.c.* with the corresponding summation convention assumed. That is, we write:

$$j_{ra}(t) = -\frac{F_0^2}{4}\sum_{\nu=-\infty}^{\infty}\sum_{n=-\infty}^{\infty}\int_{-\frac{\pi}{a}}^{\frac{\pi}{a}} dK v[K+A(t)]\int_{-T'}^{t} dt'\left\{L^*_{\nu-1}(K)-L^*_{\nu+1}(K)\right\}e^{-i\tilde{\beta}_\nu(K)t'}$$
$$\times\int_{-T''}^{t'} dt''\left\{L_{n-1}(K)-L_{n+1}(K)\right\}e^{i\tilde{\beta}_n(K)t''} + c.c. \tag{4.24}$$

We now directly integrate the two temporal integrals to obtain

$$j_{ra}(t) = \frac{-iF_0^2}{4}\sum_{n,\nu}\int_{-\frac{\pi}{a}}^{\frac{\pi}{a}} dK v[K+A(t)]\frac{\left\{L_{n-1}(K)-L_{n+1}(K)\right\}}{\tilde{\beta}_n(K)}\left\{L^*_{\nu-1}(K)-L^*_{\nu+1}(K)\right\}$$
$$\times\left[\left\{\frac{e^{i(n-\nu)\omega_0 t}-e^{-i(n-\nu)\omega_0 T'}}{i(n-\nu)\omega_0}\right\} - e^{-i\tilde{\beta}_n(K)T''}\left\{\frac{e^{-i\tilde{\beta}_\nu(K)t}-e^{i\tilde{\beta}_\nu(K)T'}}{-i\tilde{\beta}_\nu(K)}\right\}\right] + c.c. \tag{4.25}$$

If for simplicity we assume $T'' = T'$ and $T'/T_0 \in \mathbb{N}$. Then

$$j_{ra}(t) = \frac{-iF_0^2}{4}\sum_{n,\nu}\int_{-\frac{\pi}{a}}^{\frac{\pi}{a}} dK v[K+A(t)]\frac{\left\{L_{n-1}(K)-L_{n+1}(K)\right\}}{\tilde{\beta}_n(K)}\left\{L^*_{\nu-1}(K)-L^*_{\nu+1}(K)\right\}$$
$$\times\left[\left\{\frac{e^{i(n-\nu)\omega_0 t}-1}{i(n-\nu)\omega_0}\right\} + \left\{\frac{1-e^{-i\tilde{\beta}_n(K)T'}e^{-i\tilde{\beta}_\nu(K)t}}{-i\tilde{\beta}_\nu(K)}\right\}\right] + c.c. \tag{4.26}$$

Further we assume T' is large so that $e^{-i\tilde{\beta}_n(K)T'} = e^{-i\beta_n(K)T'-T'/T_2} \approx 0$, and

$$j_{ra}(t) = \frac{F_0^2}{4}\sum_{n,\nu}\int_{-\frac{\pi}{a}}^{\frac{\pi}{a}} dKv[K+A(t)]\frac{\{L_{n-1}(K)-L_{n+1}(K)\}}{\tilde{\beta}_n(K)} \times \left\{L^*_{\nu-1}(K)-L^*_{\nu+1}(K)\right\}\left[\left\{\frac{1-e^{i(n-\nu)\omega_0 t}}{(n-\nu)\omega_0}\right\}+\frac{1}{\tilde{\beta}_\nu(K)}\right]+c.c. \quad (4.27)$$

Using this, and a Fourier coefficient integral over observation time t, we can write a single cycle averaged harmonic current expression $h_{ra}(j\omega_0)$ analogous to $h_{er}(j\omega_0)$ for interband current. In doing so we obtain

$$h_{ra}(j\omega_0) = \frac{F_0^2}{4T_0}\sum_{n,\nu}\int_0^{T_0} dte^{-ij\omega_0 t}\left\{\int_{-\pi/a}^{\pi/a} dKv[K+A(t)]\frac{\{L_{n-1}(K)-L_{n+1}(K)\}}{\tilde{\beta}_n(K)} \times \left\{L^*_{\nu-1}(K)-L^*_{\nu+1}(K)\right\}\left\{\frac{1-e^{i(n-\nu)\omega_0 t}}{(n-\nu)\omega_0}\chi_{n\neq\nu}+\frac{1}{\tilde{\beta}_\nu(K)}\right\}+c.c.\right\}, \quad (4.28)$$

where $\chi_{n\neq\nu} = 1-\delta_{n,\nu}$ is introduced to remove anharmonic terms that come from $\left(1-e^{i(n-\nu)\omega_0 t}\right)/(n-\nu)\omega_0$ when $n=\nu$. We discount these terms as our theory only allows for analysis of periodic signals. However, we do not even need to consider these terms because they do not result in harmonic contributions. If we were to use a full Fourier transform integral to obtain a continuous range of frequencies these terms would result in frequency broadening about spectral maxima of harmonic intensity.

Finally, note that according to our summation convention defined in (4.23), the complex conjugate of the term shown within the outer braces of (4.28) is

$$\int_{-\pi/a}^{\pi/a} dKv[K+A(t)]\frac{\left\{L^*_{n-1}(K)-L^*_{n+1}(K)\right\}}{\tilde{\beta}^*_n(K)}\left\{L_{\nu-1}(K)-L_{\nu+1}(K)\right\} \times\left\{\frac{1-e^{-i(n-\nu)\omega_0 t}}{(n-\nu)\omega_0}\chi_{n\neq\nu}+\frac{1}{\tilde{\beta}^*_\nu(K)}\right\}. \quad (4.29)$$

That is, we took the complex conjugate of the term in braces of (4.28) *directly* as it appears. Note that the form we are using can also be understood by interpreting summation indices directly as how they appear in

$$h_{ra}(j\omega_0) = \frac{F_0^2}{2T_0}\sum_{n,\nu}\int_0^{T_0} dte^{-ij\omega_0 t}\mathrm{Re}\left\{\int_{-\pi/a}^{\pi/a} dKv[K+A(t)]\frac{\{L_{n-1}(K)-L_{n+1}(K)\}}{\tilde{\beta}_n(K)} \times \left\{L^*_{\nu-1}(K)-L^*_{\nu+1}(K)\right\}\left\{\frac{1-e^{i(n-\nu)\omega_0 t}}{(n-\nu)\omega_0}\chi_{n\neq\nu}+\frac{1}{\tilde{\beta}_\nu(K)}\right\}\right\}, \quad (4.30)$$

an alternative form of (4.28).

Classification of ionization channels

Unlike the case with interband HHG where there is only one summation over ionization channels n, here we must consider pairs of ionization processes (n, ν). Nevertheless, because of how we set up equation (4.28) with complex conjugate (4.29), we define the sets of resonant channels for both n and ν in exactly the same way we did for channels n of interband current as in equations (4.19) and (4.20). Because of this, there are more ways to classify ionization processes. There can be processes where both channels in a pair are resonant (pure resonant processes), those that have one of either n or ν being resonant (mixed processes) and those that have both being virtual (pure virtual processes).

Examples of these processes are shown in Figure 4.2 for a 1D δ-function potential solid defined by parameters: $a = 8.9$ au, $\Omega = 0.9$ au, $E_g = 0.1437$ au and $2\Delta = 0.2445$ au. A sine field of the form $F(t) = F_0 \sin(\omega_0 t)$ is used with $F_0 = 0.003$ au and $\omega_0 = E_g/7$. The (n, ν) energy changes are shown by pairs of arrows that are colour coded to $h_{ra}(j\omega_0)$ rewritten below the figure. As with a channel n of interband HHG, each pair of intraband channels (n, ν) is associated with two processes shown in parts a and b of Figure 4.2. In Figure 4.2 we do not consider velocity harmonic contribution terms. Examples are given of pure virtual (dotted arrows), mixed (dashed and dash-dotted arrows) and pure resonant (solid arrows) processes. Also shown, boxed in red, is an example of a process we exclude where $n = \nu = -13$ as it leads to a non-sinusoidal signal that we discount from our theory.

Let us consider Figure 4.2 in the context of resonant channels by considering the example where $(n, \nu) = (-16, -15)$. We see in Figure 4.2a that this process is associated with resonant excitation with energy change $-n\omega_0 = 16\omega_0$ and resonant de-excitation by energy $\nu\omega_0 = -15\omega_0$. n and ν reverse roles in resonant excitation and de-excitation in the process of Figure 4.2b. However, it should be noted that the reversal of the sign(s) (and therefore direction of arrows) of at least one of n and ν results in a non-resonant pair (n, ν). For the portion of intraband HHG shown in Figure 4.2, given that resonant channels are negative in our formulation (same reasoning follows as with interband current) and that the energy difference leading to harmonic order j is $(\nu - n)\omega_0$ (Figure 4.2a) or $(n - \nu)\omega_0$ (Figure 4.2b), we observe that a purely resonant process always consists of a resonant excitation contribution (e.g. $n = -16$ in Figure 4.2a for $(n, \nu) = (-16, -15)$) and a resonant de-excitation contribution (e.g. $\nu = -15$ in Figure 4.2a for $(n, \nu) = (-16, -15)$).

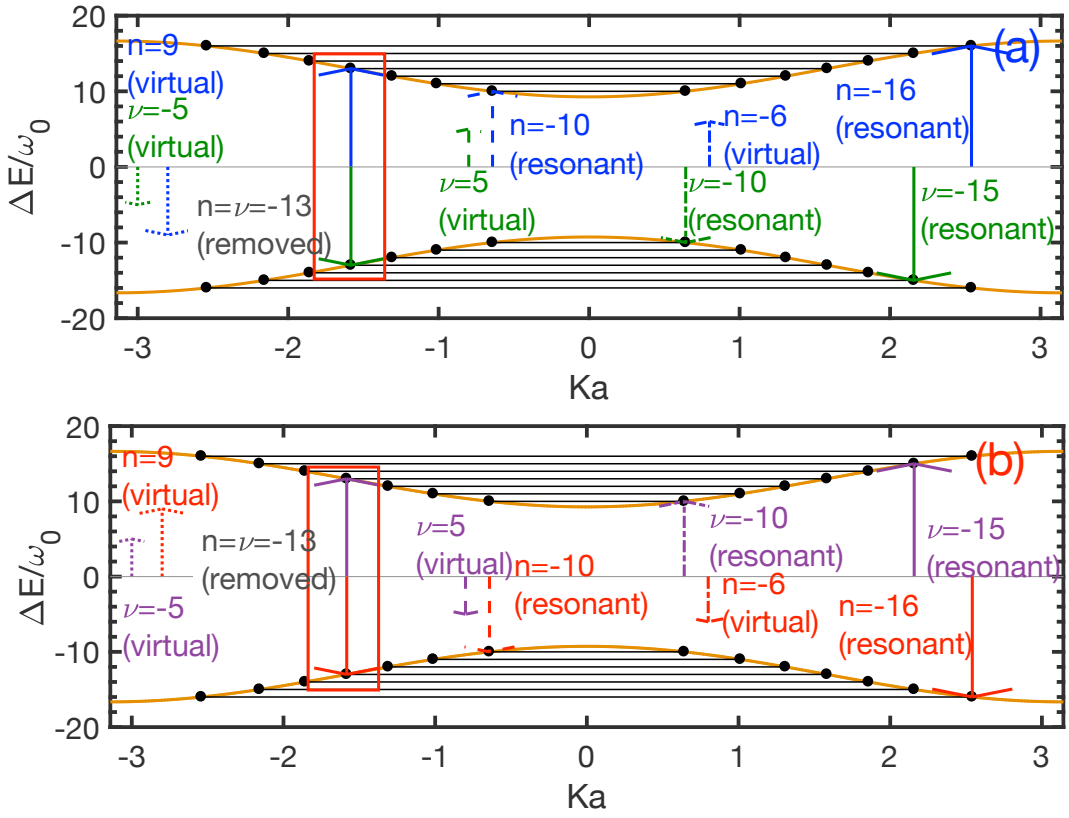

$$h_{ra}(j\omega_0) = \frac{F_0^2}{4T_0}\sum_{n,\nu}\int_0^{T_0} dt e^{-ij\omega_0 t}\Big\{\int_{-\pi/a}^{\pi/a} dK v[K+A(t)]\frac{\{L_{n-1}(K)-L_{n+1}(K)\}}{\tilde{\beta}_n(K)}$$
$$\times\left\{L^*_{\nu-1}(K)-L^*_{\nu+1}(K)\right\}\left\{\frac{1-e^{i(n-\nu)\omega_0 t}}{(n-\nu)\omega_0}\chi_{n\neq\nu}+\frac{1}{\tilde{\beta}_\nu(K)}\right\}+\int_{-\pi/a}^{\pi/a} dK v[K+A(t)]$$
$$\times\frac{\left\{L^*_{n-1}(K)-L^*_{n+1}(K)\right\}}{\tilde{\beta}^*_n(K)}\left\{L_{\nu-1}(K)-L_{\nu+1}(K)\right\}\left\{\frac{1-e^{-i(n-\nu)\omega_0 t}}{(n-\nu)\omega_0}\chi_{n\neq\nu}+\frac{1}{\tilde{\beta}^*_\nu(K)}\right\}\Big\}$$

Figure 4.2: Examples of resonant and non-resonant intraband ionization processes for a 1D δ-function potential solid with parameters: $a = 8.9$ au, $\Omega = 0.9$ au, $E_g = 0.1437$ au and $2\Delta = 0.2445$ au. A sine field of the form $F(t) = F_0\sin(\omega_0 t)$ is used with $F_0 = 0.003$ au and $\omega_0 = E_g/7$. $\pm\mathcal{E}_{ns}(K)/\omega_0$ is shown in orange with black lines and dots having *absolute values* equal to absolute values of individual resonant channels. Examples of processes associated with ordered pairs of channels (n,ν) have energy differences (ΔE) shown as pairs of arrows in each figure. Each pair of channels (n,ν) has two processes associated with them ((a) and (b) correspond to these processes). The arrows are colour coded according to (4.28) with complex conjugate (4.29) rewritten here. Shown are examples of pure virtual (dotted arrows), mixed (dashed and dash-dotted arrows) and resonant (solid arrows) processes. Boxed in red is an example of a case where $n = \nu$ leading to a non-sinusoidal signal that we remove from our theory. Terms relating to velocity harmonics from $v[K + A(t)]$ are not shown here.

4.2 Results

4.2.1 Interband and intraband ionization processes based harmonic spectra

In this section we compare numerical results of interband and intraband harmonic spectra $|h_{er}(j\omega_0)|^2$ and $|h_{ra}(j\omega_0)|^2$ calculated according to equations (4.16) and (4.30) respectively. Furthermore, for both interband and intraband currents, we compare harmonic spectra constructed only from specific classifications of ionization channels (resonant and virtual for interband; resonant, virtual and mixed for intraband). In doing so we consider different 1D δ-function potential solids (see Chapter 2) with similar minimum band gaps of $E_g \approx 1.4$ au and bandwidths 2Δ ranging from 0.0566 au to 0.2445 au to allow for insight into HHG in wide bandwidth materials like semiconductors vs. narrow bandwidth materials like insulating dielectrics. In all examples we take the field amplitude to be $F_0 = 0.003$ au and the laser field angular frequency to be $\omega_0 = E_g/7$. To facilitate numerical calculations we use a relatively short dephasing time of $T_2 = T_0/2 = \pi/\omega_0$ so that denominator terms such as $1/\tilde{\beta}_n(K) = (\beta_n(K) - i/T_2)^{-1}$ of (4.16) and (4.28) do not vary too abruptly for K in the neighbourhoods of $\pm K_n$ that fulfill the condition $\beta_n(\pm K_n) = 0$ for resonant channels (same idea for $1/\tilde{\beta}_\nu(K)$ terms). All integrals are calculated numerically via trapezoidal integration except for action integrals, $\int_0^t R(K,\tau)d\tau$, that can be calculated analytically from (4.6b).

Interband

In Figure 4.3a-d are plots of harmonic yield $|h_{er}(j\omega_0)|^2$ (along with virtual and resonant ionization channel only yields) for odd harmonics j for four solids in order of decreasing bandwidth 2Δ. We observe, as should be expected, that high harmonic plateau regions, above the minimum band gap harmonic $j = 7$, have greater extents and yields for the solids that have greater bandwidths 2Δ. This is likely because such can support greater ranges of frequencies for fixed field parameters and similar minimum band gaps E_g. Despite the variation in bandwidth, we observe similar characteristics in all examples: the full yields are well represented by resonant ionization processes alone in the high harmonic plateau region above the minimum band gap E_g ($j > (E_g/\omega_0 = 7)$). Virtual channels generally tend to be of most importance only for low harmonic orders j below the minimum band gap. Of note is that the full spectrum is not always greater than the spectra of virtual and resonant channels alone. This demonstrates the importance of interference, not only constructive but also destructive, between processes associated with these channels for given harmonic orders. This is indicative of the importance of

signs/phases of components of interband currents. We consider such interference more closely in Section 4.2.2.

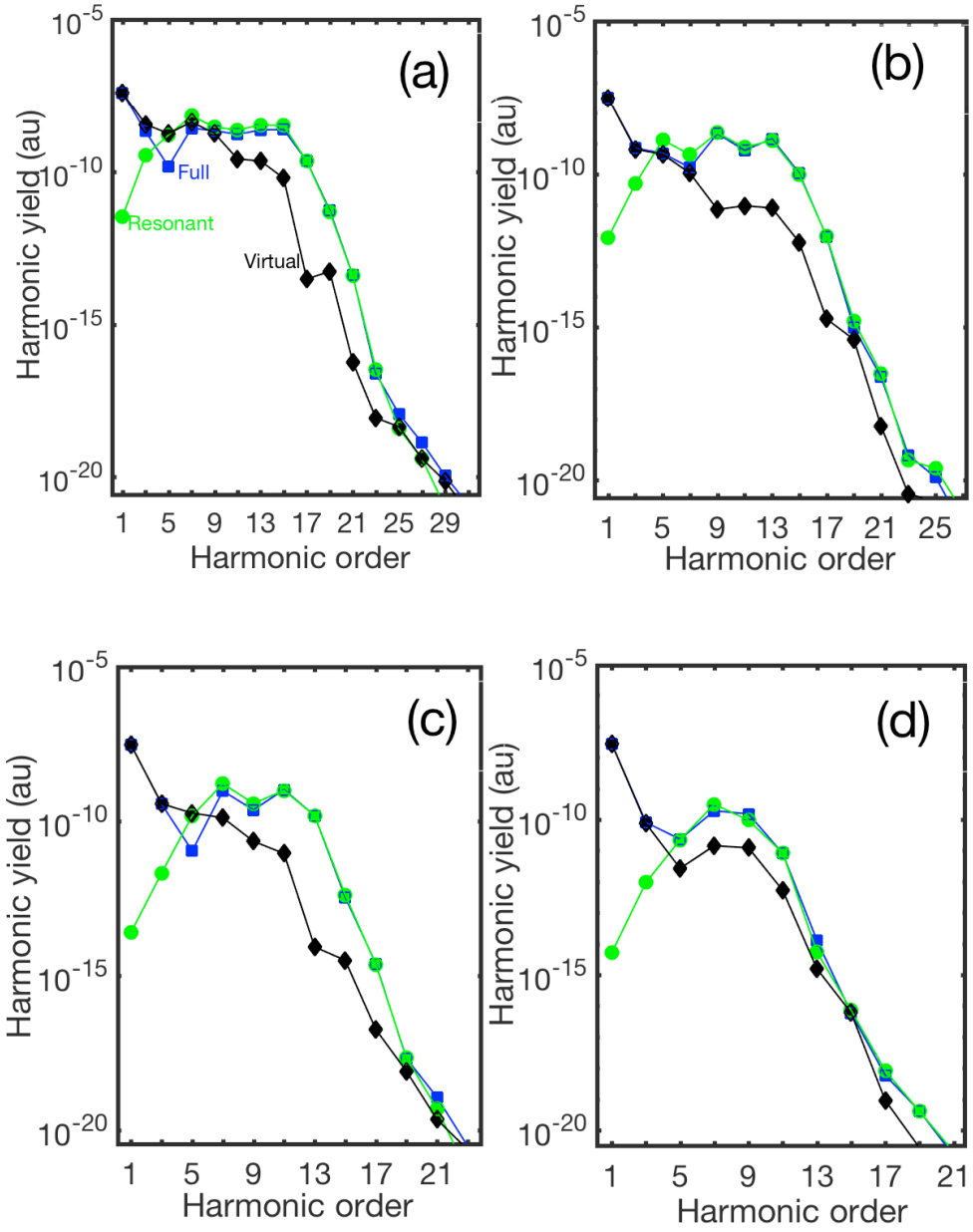

Figure 4.3: Comparison of full interband HHG spectra (blue squares), to resonant ionization channel only spectra (green circles) and virtual ionization channel only spectra (black diamonds). Plots (a)-(d) are given in descending order of solid bandwidths $2\Delta = 0.2445$, 0.1573, 0.1153, 0.0566 au and are defined in the same order by lattice parameters $a = 8.9$, 9.9, 10.5, 11.7 au; barrier strengths $\Omega = 0.9$, 1.2, 1.5, 2.5 au; and the minimum band gaps $E_g = 0.1437$, 0.1431, 0.1440, 0.1410 au. For all, the field form is $F(t) = F_0 \sin(\omega_0 t)$, with $F_0 = 0.003$ au, $\omega_0 = E_g/7$ and dephasing time $T_2 = \pi/\omega_0$.

Intraband

Next, in Figure 4.4a-d we consider intraband harmonic yield $|h_{ra}(j\omega_0)|^2$ for the same four solids as with interband current. Also plotted are harmonic yields corresponding to ionization channels pairs (n, ν) that are purely resonant, purely virtual, mixed and the combination of both mixed and purely virtual (at least one part of ionization process is virtual). As with interband HHG, the extent of yield and high harmonic orders is greater for solids with greater bandwidths 2Δ. In all examples purely resonant ionization channel pairs have very little influence on the full harmonic yields and the yields corresponding to such fall off very rapidly from the first harmonic onward. Furthermore, in all examples the combination of mixed and virtual channels matches very closely with the full result. It should be stated that both mixed and purely virtual channels are non-resonant because at least one channel in the pair (n, ν) is not. We therefore observe that in contrast to the situation with interband current HHG being mostly driven by resonant ionization processes, intraband HHG is driven mostly by virtual ionization processes. Distinguishing purely virtual ionization processes from mixed ionization processes we observe that mixed processes tend to be of most relevance for above minimum band gap harmonics ($j > 7$). For the lowest harmonic orders ($j = 1, 3$), much like the situation with virtual channels for interband HHG, purely virtual processes are most important. For $j = 5$ and $j = 7$, below and at the minimum band gap respectively, mixed and purely virtual processes are both of importance and destructively interfere. The only exception to this is for the narrowest bandwidth material of Figure 4.4d where mixed processes have the most similarity to the full spectrum.

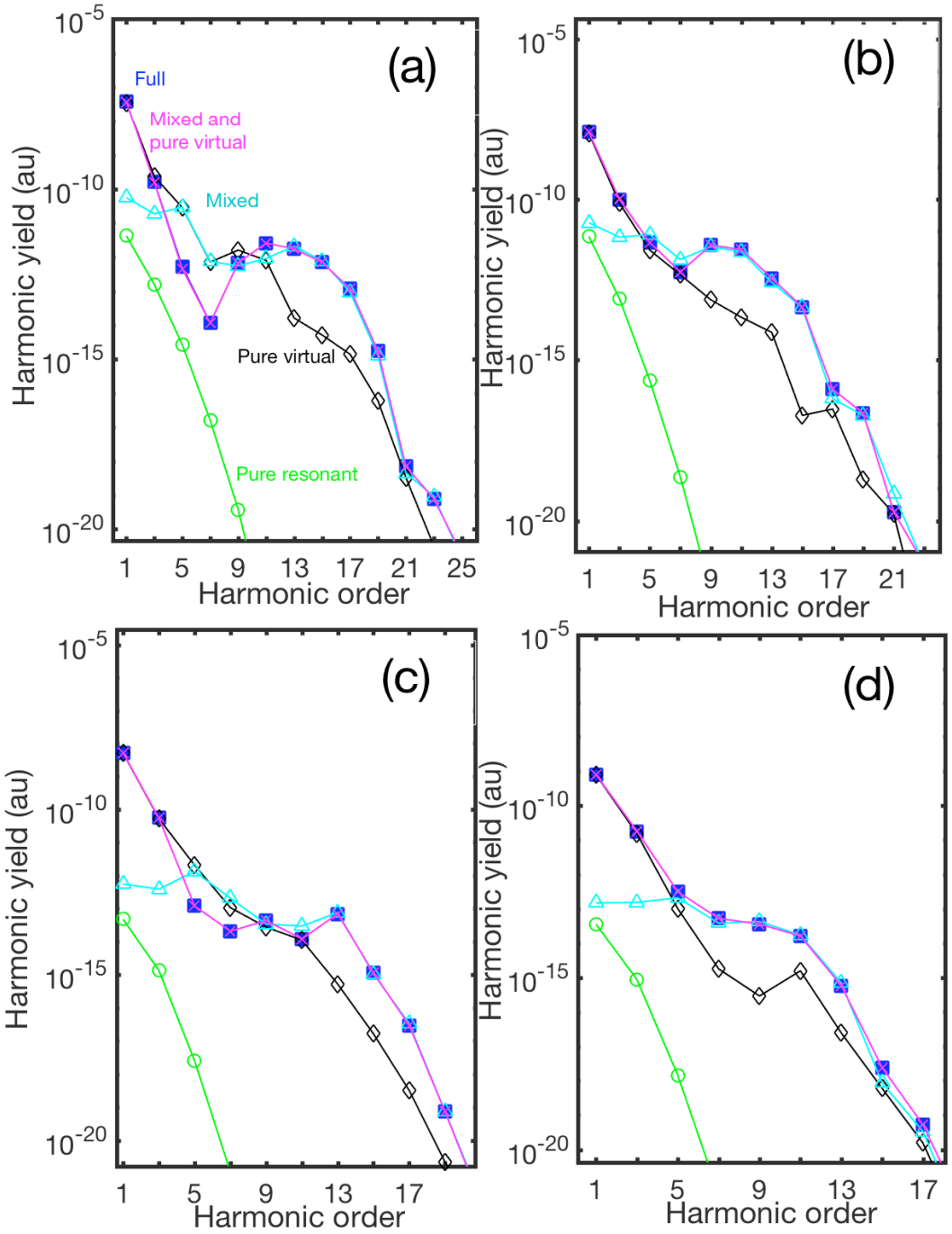

Figure 4.4: Comparison of full intraband HHG spectra (blue squares) to those constructed of purely resonant (green circles), purely virtual (black diamonds), mixed (cyan triangles) and the combination of mixed and purely virtual (pink crosses) ionization channel pairs (n, ν). Plots (a)-(d) are given in descending order of solid bandwidths $2\Delta = 0.2445$, 0.1573, 0.1153, 0.0566 au and are defined in the same order by lattice parameters $a = 8.9$, 9.9, 10.5, 11.7 au; barrier strengths $\Omega = 0.9$, 1.2, 1.5, 2.5 au; and the minimum band gaps $E_g = 0.1437$, 0.1431, 0.1440, 0.1410 au. For all, the field form is $F(t) = F_0 \sin(\omega_0 t)$, with $F_0 = 0.003$ au, $\omega_0 = E_g/7$ and dephasing time $T_2 = \pi/\omega_0$.

Summary

In summary, our results seem to imply that primarily resonant ionization driven interband HHG is more significant than non-resonant (mixed and pure virtual channel pairs) ionization driven intraband HHG. We find that how ionization processes affect HHG does not vary much by changing solid state bandwidths. However, we will consider these mechanisms more closely in Sections 4.2.2 and 4.2.3. We will next consider these results in the context of experimental findings.

Comparison with experiments

Let us discuss these findings in relation to experimental findings. Results for wide bandwidth materials (like the solid in Figure 4.3a and Figure 4.4a) seem to be in agreement with certain experiments involving semiconductors [32, 36]. In [36] an HHG experiment is performed with the semiconductor zinc oxide. In this experiment, odd harmonic symmetry is broken using a weak second harmonic laser field, and the time delay signature of second harmonics closely resembles results from an interband simulation. In [32] such an experiment is performed with magnesium oxide. There, results are attributed to an electron-hole recollision based interband model.

On the other hand, in [25, 28] HHG experiments are performed with the dielectric silicon dioxide (polycrystalline). The conclusion of both papers is that intraband current has greater importance than interband current. These results contradict our findings for narrow bandwidth materials like that in Figure 4.4d. Nevertheless, the method for which these conclusions were made are based on comparisons to chosen computational models. In the model used in the supplement of [28], interband HHG is modelled to be greater than intraband HHG. The conclusion that intraband HHG was greater from the experiment was according to closer similarity between the experimental signal characteristics to those of modelled intraband HHG. Similar is done in [25], but, in the computational simulation in the corresponding supplement, Coulomb binding energy of excitons is accounted for. Increasing this binding energy in turn increased the strength of intraband HHG relative to interband HHG. Despite this, they computationally found similar group delays (chirps) with harmonic order for interband and intraband currents for different exciton binding energies, indicating that important characteristics are not lost despite the introduction of such. The models we use are highly simplified and do not account for such features as exciton binding energy. In semiconductors screening is often greater than in dielectrics [54], such that excitonic binding energies are expected to be lower. Although this may not be an essential difference, this may be part of the explanation as to why our results agree better for experiments involving semiconductors than those involving

dielectrics. However, because much of our models can be expressed in simple analytical terms, they may still be of use for obtaining insight into idealized scenarios or situations where the strength of HHG in of itself is disregarded for overall spectral characteristics. In particular, its insight into the importance of virtual vs. resonant ionization processes may still be of relevance. However, the eventual addition of more complex features into reasonably simple models as such is still an objective.

To the extent that this model is viable, given the nature of different ionization processes explored in Figure 4.3 and Figure 4.4 in this section, we would like to have a better understanding of how such differences arise. We will explore such questions in the next sections.

4.2.2 Interband HHG more specifically

In this section we regard more closely how ionization channels lead to the harmonic spectra in Figure 4.3. We focus here on the example with greatest bandwidth material of Figure 4.3a and the examples with the smallest bandwidth Figure 4.3d. Figure 4.3 provides an overview of the ionization characteristics of interband HHG, but does not provide indication of how individual ionization channels contribute to the overall result based on their contributions' magnitudes and relative phases.

Phase free harmonic spectra

One method to regard this is by calculating interband HHG with relative phases of summation terms removed from (4.16) by rewriting it as

$$h_{er}(j\omega_0) = \frac{\pi i j F_0}{T_0} \sum_{n=-\infty}^{\infty} \left| \int_{-\pi/a}^{\pi/a} dK \left\{ \frac{L_{n-j}^*(K)[L_{n-1}(K) - L_{n+1}(K)]}{\tilde{\beta}_n(K)} + \frac{L_{n+j}(K)[L_{n-1}^*(K) - L_{n+1}^*(K)]}{\tilde{\beta}_n^*(K)} \right\} \right|. \quad (4.31)$$

That is we are now taking the absolute value of each summation term. We then compare phase free results of total, resonant and virtual spectra to actual spectra of Figure 4.3.

Figure 4.5a and Figure 4.5b show the phase free spectra corresponding to the wide and narrow bandwidth materials of Figure 4.3a and Figure 4.3d respectively. We observe in both cases that without relative phases, virtual contributions become significantly more important until regions of spectral fall-off that are beyond the high harmonic plateaus in Figure 4.3. The importance of virtual ionization channels in the phase free spectra of Figure 4.5, but not in the original spectra of Figure 4.3 demonstrates

the importance of destructive interference between interband current contributions of different virtual ionization channels. By contrast, the resonant ionization spectra do not differ so much between the original spectra of Figure 4.3 and the phase free spectra of Figure 4.5. This is particularly seen for the narrow bandwidth material's spectra of Figure 4.5b relative to Figure 4.3d where the resonant spectra are the same in both cases because this solid has only one resonant ionization channel ($n = -8$) for the given field configuration (see (4.19)). As for the wide bandwidth material of Figure 4.5a and Figure 4.3a, there is some degree of destructive interference as its resonant ionization channels range from -16 to -10. Nevertheless, the extent of this is significantly less than destructive interference between virtual channels. Overall, we find that, for both wide and narrow bandwidth materials, virtual ionization processes contribute the greatest overall magnitude to interband current, but much of these processes destructively interfere so that resonant ionization processes are the main drivers of interband HHG.

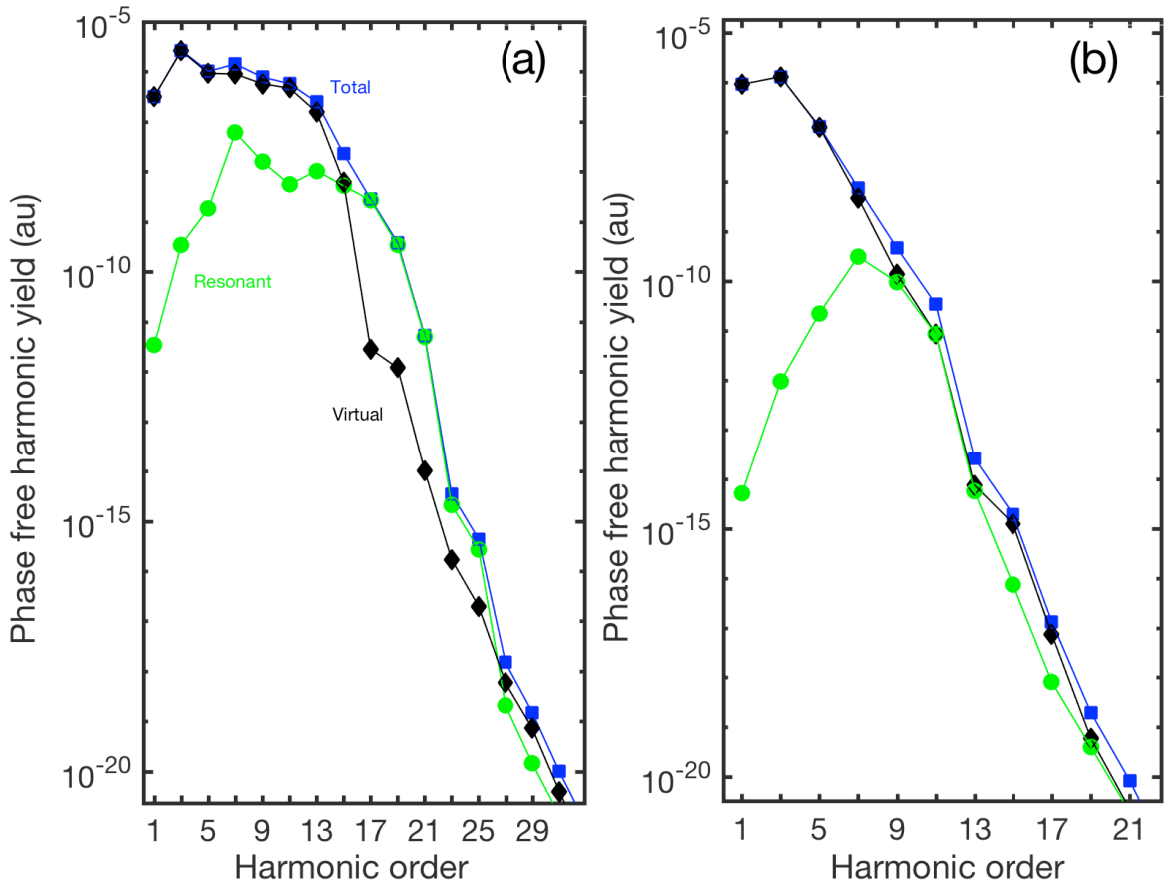

Figure 4.5: Phase free interband harmonic spectra for (a), the wide bandwidth material ($a = 8.9$ au, $\Omega = 0.9$ au, $E_g = 0.1437$ au, $2\Delta = 0.2445$ au) of Figure 4.3a and (b), the narrow bandwidth material ($a = 11.7$ au, $\Omega = 2.5$ au, $E_g = 0.1410$ au, $2\Delta = 0.0566$ au) of Figure 4.3d. Symbols plotted have meanings analogous to those in Figure 4.3 (blue squares - total, green circles - resonant, black diamonds - virtual) and field parameters are the same. That is, for both the field form is $F(t) = F_0 \sin(\omega_0 t)$, with $F_0 = 0.003$ au, $\omega_0 = E_g/7$ and dephasing time $T_2 = \pi/\omega_0$.

Cumulative summation steps over ionization channels

We can further regard individual ionization channel contributions by considering the harmonic yield calculated from each cumulative summation step in (4.16) for a representative set of ionization channels n (starting for example from the greatest magnitude negative channel to the greatest magnitude positive channel). Doing so allows us to examine the amount of change in harmonic yield resulting from any given step. It also allows us to pinpoint how channels interfere to give the final full result. We can regard such as well to observe similarities and differences between how such occurs with resonant vs. virtual channels.

To be clear, let us define

$$h_{er}^{(n)}(j\omega_0) = \frac{\pi i j F_0}{T_0} \sum_{n'=n_{\min}}^{n} \int_{-\pi/a}^{\pi/a} dK \left\{ \frac{L_{n'-j}^*(K)[L_{n'-1}(K) - L_{n'+1}(K)]}{\tilde{\beta}_{n'}(K)} + \frac{L_{n'+j}(K)[L_{n'-1}^*(K) - L_{n'+1}^*(K)]}{\tilde{\beta}_{n'}^*(K)} \right\}, \quad (4.32)$$

so that the cumulative summation harmonic yield is $|h_{er}^{(n)}(j\omega_0)|^2$. Using this we plot in Figure 4.6, for various harmonic orders, $\log_{10}(|h_{er}^{(n)}(j\omega_0)|^2/|h_{er}(j\omega_0)|^2)$, where $|h_{er}(j\omega_0)|^2$ corresponds approximately to the summation total (corresponds to results of Figure 4.3; approximate because summation limits are finite and are given by $n = \pm 23$ in Figure 4.6a and $n = \pm 15$ in Figure 4.6b). Figure 4.6a corresponds to the wide bandwidth solid ($a = 8.9$ au, $\Omega = 0.9$ au, $E_g = 0.1437$ au, $2\Delta = 0.2445$ au) of Figure 4.3a and Figure 4.6b the narrow bandwidth solid ($a = 11.7$ au, $\Omega = 2.5$ au, $E_g = 0.1410$ au, $2\Delta = 0.0566$ au) of Figure 4.3d.

Considering Figure 4.6a for the wide bandwidth material we observe for harmonic orders in the plateau region ($j = 7 - 17$; see Figure 4.3a) that the total harmonic yield is approximately reached upon summation to the final resonant channel $n = -10$. Generally, virtual channels beyond this either result in little change or destructively interfere. In this region the greatest change is generally contained in the resonant region while virtual channels below usually contribute little. The trend only differs at lower harmonic orders where virtual channels above $n = -10$ have the most significance. However, even in this region the full range of virtual channels is not needed as many of their contributions destructively interfere.

Next, considering Figure 4.6b for the narrow bandwidth material we see a similar trend. For most harmonic orders $j = 5$ onwards, approximate convergence to the total is seen at the sole resonant channel $n = -8$. The significance of processes associated with $n = -8$ is therefore clear. Virtual channels above $n = -8$ are generally insignificant (more so even than with the wide bandwidth material), but when they are, they destructively interfere out similarly to the case with the wide bandwidth material in Figure 4.6a. Virtual channels are only important for low harmonic orders in the same way as with the wide bandwidth material.

Overall, the results here further assert the importance of resonant transitions compared to non-resonant transitions as the cause of interband HHG.

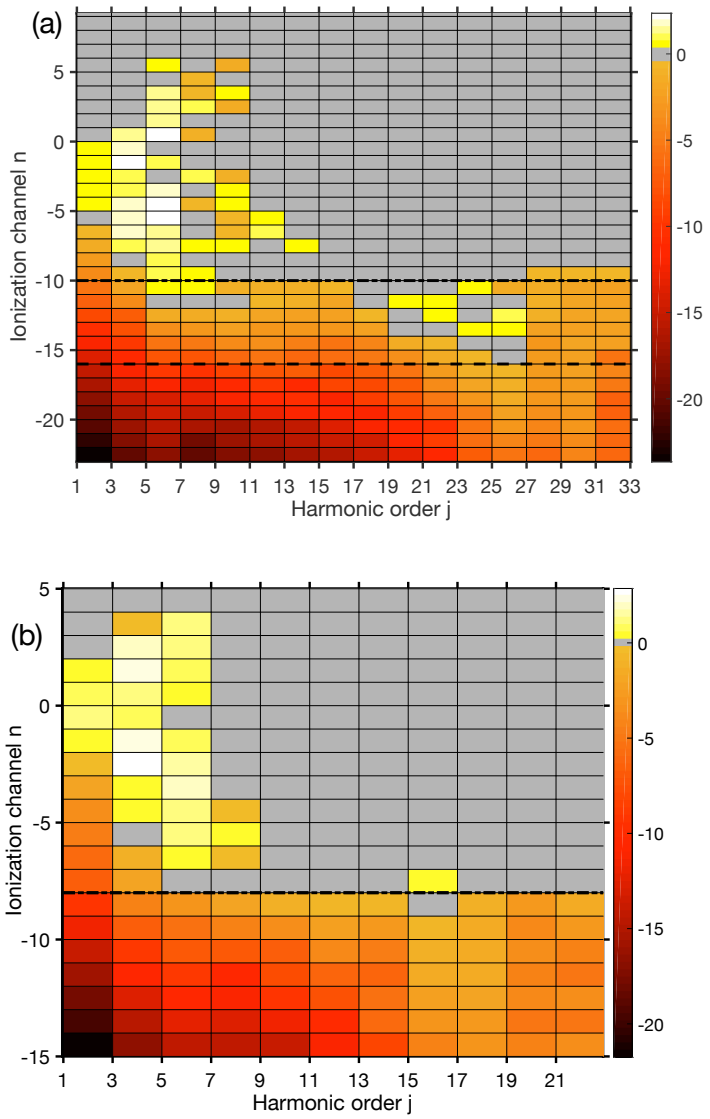

Figure 4.6: Cumulative summations over representative sets of ionization channels n used for calculating $h_{er}(j\omega_0)$ and corresponding spectra $|h_{er}(j\omega_0)|^2$ as in Figure 4.3. Specifically, the colourbar refers to $\log_{10}(|h_{er}^{(n)}(j\omega_0)|^2/|h_{er}(j\omega_0)|^2)$ where $|h_{er}^{(n)}(j\omega_0)|^2$ from (4.32) refers to the cumulative summation from the lowest channel displayed to channel n and $|h_{er}(j\omega_0)|^2$ refers to the summation total. Part (a) corresponds to the wide bandwidth solid ($a = 8.9$ au, $\Omega = 0.9$ au, $E_g = 0.1437$ au, $2\Delta = 0.2445$ au) of Figure 4.3a with summation minimum $n_{\min} = -23$ and part (b) the narrow bandwidth solid ($a = 11.7$ au, $\Omega = 2.5$ au, $E_g = 0.1410$ au, $2\Delta = 0.0566$ au) of Figure 4.3d with summation minimum $n_{\min} = -15$. In part (a) the summation total $|h_{er}(j\omega_0)|^2$ is calculated from summation from $n = -23$ to $n = 23$ while in (b) such is calculated from $n = -15$ to $n = 15$. Plots are asymmetric about $n = 0$ because little change is seen beyond maximum positive channels n displayed. Field parameters: $F_0 = 0.003$ au, $\omega_0 = E_g/7$ and $T_2 = T_0/2 = \pi/\omega_0$. Dashed and dash-dotted lines refer to greatest and lowest *magnitude* resonant channels respectively. Grey spaces are used to indicate results of $|h_{er}^{(n)}(j\omega_0)|^2$ approximately equal to the total summation harmonic yield $|h_{er}(j\omega_0)|^2$. Grey area ranges are from -0.4908 to 0.3129 in (a) and from -0.2219 to 0.1627 in (b).

4.2.3 Intraband HHG more specifically

In this section we regard transitions leading to intraband HHG more specifically. We do this primarily by comparing spectra with phases removed in summation terms for (n, ν) to actual spectra of Figure 4.4 corresponding to widest and narrowest bandwidth materials there. For both materials, we will also test an approximation where we set $v[K + A(t)] \approx v(K)$, and consider the insight this provides us.

Phase free harmonic spectra

Here we follow the same approach as we did for calculating phase free interband harmonic spectra. That is we modify (4.28) as

$$h_{ra}(j\omega_0) = \frac{F_0^2}{4T_0} \sum_{n,\nu} \left| \int_0^{T_0} dt e^{-ij\omega_0 t} \left\{ \int_{-\pi/a}^{\pi/a} dK v[K + A(t)] \frac{\{L_{n-1}(K) - L_{n+1}(K)\}}{\tilde{\beta}_n(K)} \right.\right.$$
$$\left.\left. \times \left\{L^*_{\nu-1}(K) - L^*_{\nu+1}(K)\right\} \left\{ \frac{1 - e^{i(n-\nu)\omega_0 t}}{(n-\nu)\omega_0} \chi_{n\neq\nu} + \frac{1}{\tilde{\beta}_\nu(K)} \right\} + c.c. \right\} \right|, \quad (4.33)$$

and calculate corresponding phase free spectra from $|h_{ra}(j\omega_0)|^2$. The results of such for the configuration of Figure 4.4 for the wide bandwidth material ($a = 8.9$ au, $\Omega = 0.9$ au, $E_g = 0.1437$ au, $2\Delta = 0.2445$ au) and the narrow bandwidth material ($a = 11.7$ au, $\Omega = 2.5$ au, $E_g = 0.1410$ au, $2\Delta = 0.0566$ au) are shown in Figure 4.7.

We observe for both materials of Figure 4.7 that non-resonant processes (pure virtual and mixed) overwhelmingly carry the majority of weight. Of these non-resonant processes, pure virtual processes hold greater weight than mixed processes. Nevertheless, in the actual spectra of Figure 4.4a (wide bandwidth material) and Figure 4.4d (low bandwidth material), we observe that high harmonics are primarily dominated by mixed channel processes. This demonstrates a significant degree of destructive interference amongst pure virtual processes (we would expect in a similar way as with virtual interband channels shown in Figure 4.6) and not amongst mixed channel processes. Despite this, virtual processes still retain greater importance than purely resonant processes that carry negligible weight.

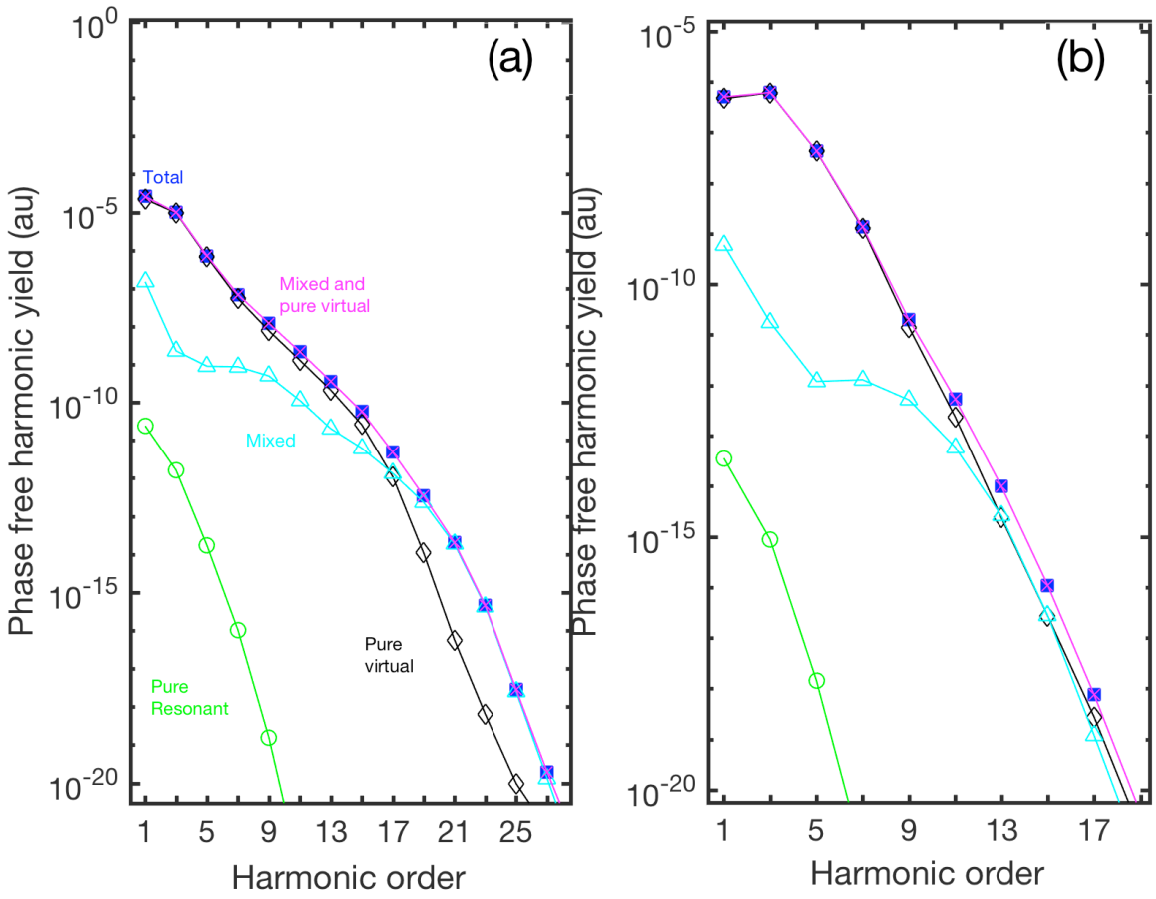

Figure 4.7: Phase free intraband harmonic spectra for (a), the wide bandwidth material ($a = 8.9$ au, $\Omega = 0.9$ au, $E_g = 0.1437$ au, $2\Delta = 0.2445$ au) of Figure 4.4a and (b), the narrow bandwidth material ($a = 11.7$ au, $\Omega = 2.5$ au, $E_g = 0.1410$ au, $2\Delta = 0.0566$ au) of Figure 4.4d. Symbols plotted have meanings analogous to those in Figure 4.4 (blue squares - total, green circles - pure resonant, black diamonds - pure virtual, cyan triangles - mixed, pink crosses - mixed and virtual) and field parameters are the same. That is, for both the field form is $F(t) = F_0 \sin(\omega_0 t)$, with $F_0 = 0.003$ au, $\omega_0 = E_g/7$ and dephasing time $T_2 = \pi/\omega_0$.

The $v[K + A(t)] \approx v(K)$ approximation

Finally, let us consider an approximation where we set $v[K+A(t)] = v(K)$. That is, within the context of the velocity gauge ($K = k - A(t)$), we remove the oscillating part that could possibly contribute to HHG. Within this context, transition processes associated with channel pairs (n, ν) could be taken as direct drivers of HHG. The processes leading to such can then be described exactly as shown in Figure 4.2. That is Figure 4.2a corresponds to $j = \nu - n$ and Figure 4.2b corresponds to $j = n - \nu$. Furthermore, in the context of positive harmonic orders ($j > 0$), we would only need to consider one of the processes for any given pair (n, ν) where $n \neq \nu$.

In the context of a nearest-neighbour band gap $\mathcal{E}_g(K) = E_g + \Delta\{1 - \cos(Ka)\}$ the velocity term is given by $v(K) = \partial_K \mathcal{E}_g(K) = a\Delta \sin(Ka)$. For a sine field of the form $F(t) = F_0 \sin(\omega_0 t)$, the vector potential is given by $A(t) = (F_0/\omega_0)\cos(\omega_0 t)$ so that $v[K + A(t)] = a\Delta \sin[Ka + \omega_b/\omega_0 \cos(\omega_0 t)]$, with Bloch angular frequency $\omega_b = F_0 a$. Therefore, for a small ratio ω_b/ω_0 we expect that we can neglect corresponding small amplitude oscillations about Ka values.

In Figure 4.8 we test this approximation (green circles) compared to the full result (blue squares; same as in Figure 4.4) for the widest bandwidth material ($a = 8.9$ au, $\Omega = 0.9$ au, $E_g = 0.1437$ au, $2\Delta = 0.2445$ au) and narrowest bandwidth material ($a = 11.7$ au, $\Omega = 2.5$ au, $E_g = 0.1410$ au, $2\Delta = 0.0566$ au) configurations of Figure 4.4. That is we use field parameters: $F_0 = 0.003$ au, $\omega_0 = E_g/7$ and $T_2 = T_0/2 = \pi/\omega_0$. We observe that the approximation works better for the wide bandwidth material than it does for the narrow bandwidth material. Note that the ratio $\omega_b/\omega_0 \approx 1.301$ for the wide bandwidth material configuration while it is ≈ 1.743 for the narrow bandwidth material. Although greater than one, the fact that this ratio is smaller for the wide bandwidth material is the most likely explanation for the better approximation there. This is despite the wide bandwidth material having a larger velocity amplitude of $a\Delta \approx 1.088$ au than that of the narrow bandwidth material with $a\Delta \approx 0.3311$ au. This demonstrates the potential usefulness of this approximation for simplifying analytical intraband calculations. Furthermore, our reason for testing this approximation for these particular examples is because in the context of our discussions about transitions associated with channel pairs (n, ν), we observe that these transitions are the primary drivers of intraband HHG for the wide bandwidth configuration, while with the narrow bandwidth configuration, one must consider the effect of nonlinear velocity oscillations with t in addition to these transitions. In addition, because mixed channel non-resonant transitions dominate the high harmonic plateau of the wide bandwidth material's spectrum as in Figure 4.4a, we note that thinking about intraband HHG being caused directly by these transitions is a valid approximation.

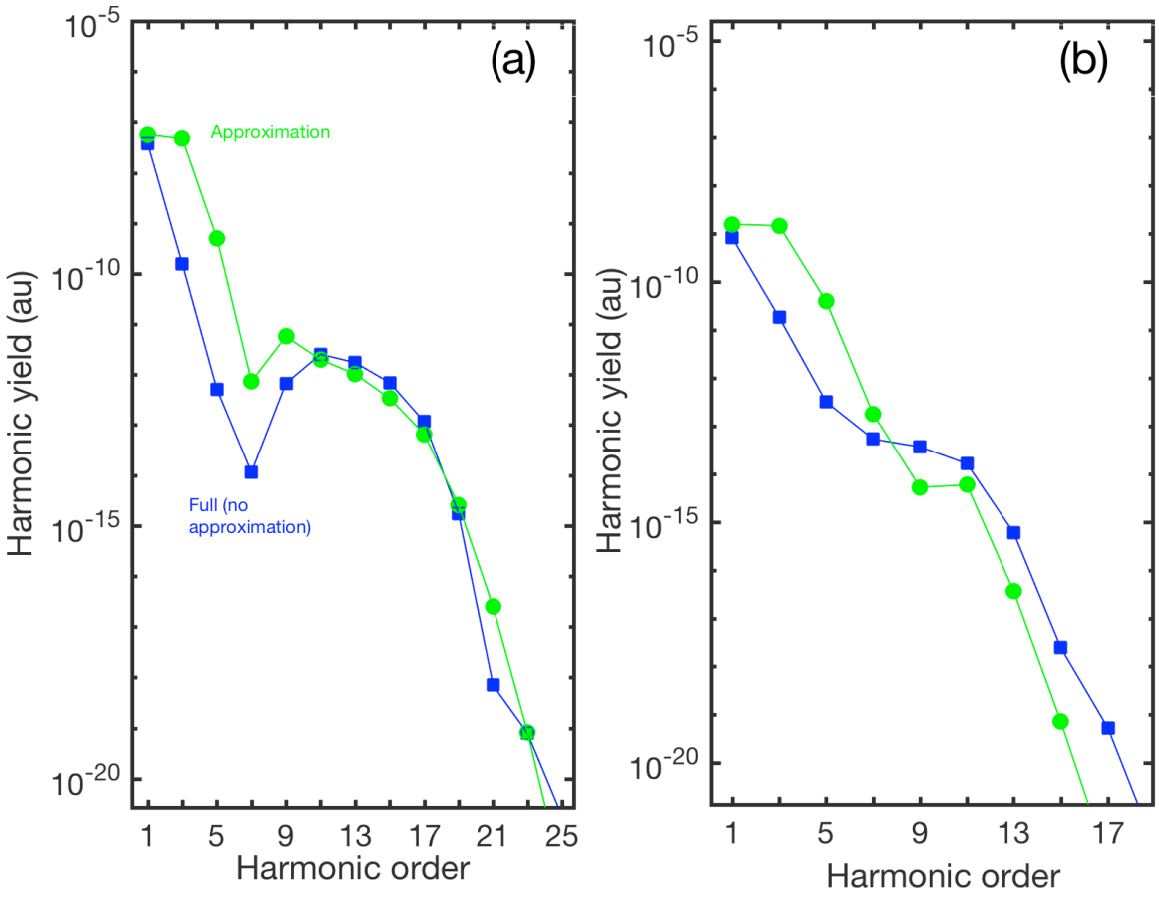

Figure 4.8: Comparison of intraband harmonic yields $|h_{ra}(j\omega_0)|^2$ calculated using (4.30) with the approximation $v[K+A(t)] \approx v(K)$ (green circles) and without the approximation (blue squares). Part (a) corresponds to the wide bandwidth solid ($a = 8.9$ au, $\Omega = 0.9$ au, $E_g = 0.1437$ au, $2\Delta = 0.2445$ au) of Figure 4.4a and part (b) the narrow bandwidth solid ($a = 11.7$ au, $\Omega = 2.5$ au, $E_g = 0.1410$ au, $2\Delta = 0.0566$ au) of Figure 4.4d. Field parameters: $F_0 = 0.003$ au, $\omega_0 = E_g/7$ and $T_2 = T_0/2 = \pi/\omega_0$.

Chapter 5

Conclusion

In this thesis we tried to gain a better understanding of prevailing mechanisms leading HHG in solids. We explored the mechanisms leading to HHG in solids by implementing a 1D δ-function potential of solids into a two-band model of interband and intraband current. We found that the 1D δ-function model provides a simple means of modelling electronic properties of solids required of the two-band model such as band gaps and dipole moments. We then constructed a WQC model for interband HHG in semiconductors by transforming k-space dependent Bloch dipole moments to the real space Wannier basis, and then applying the saddle point approximation. Using the 1D δ-function potential model we formulated, we found that this model demonstrated reasonable quantitative agreement with a fully numerical model. Furthermore, we found that this model provided an intuitive description of HHG in semiconductors in a 'three-step' model of ionization, acceleration and recollision of electron-hole pairs. Given that interband HHG has been demonstrated by experiments [32, 37] to be the dominant mechanism in semiconductors, we find that the WQC model explains the most important dynamics there. In the final chapter we approached HHG from a different perspective. We used methodology similar to that of Keldysh in [48] to examine the importance of resonant as well as non-resonant valence-conduction band transitions leading to interband HHG as well as intraband HHG in solids. Using the 1D δ-function potential model we developed, we found interband HHG to be primarily driven by resonant transitions and intraband HHG to be driven primarily by non-resonant processes. In both cases we noted that non-resonant transitions carried the most weight when phases of individual transitions were neglected. Nevertheless, destructive interference of non-resonant processes diminished its importance for interband HHG while this interference was lesser with intraband HHG. We saw similar results in narrow bandwidth modelled solids and wide bandwidth modelled solids with interband HHG dominating in all cases. We found this to be consistent with semiconductor experiments [32, 37] where interband HHG was found to dominate, but inconsistent with dielectric experiments [25, 28] where intraband current dominates.

Despite this, we considered the model to provide qualitative HHG characteristics in an idealized scenario where effects such as electron-hole Coulomb forces are neglected.

Although the results of the simple models used in this thesis are certainly non-exhaustive in explaining HHG in solids, we considered new ways of comprehending the relevant dynamics of such. Building on these simple models by adding such features as electron-hole Coulomb forces and thermal effects should hopefully improve understanding further. The improved understanding of HHG in solids will hopefully eventually allow for better control of such in its applications such as being an all-optical tabletop XUV source [28] and being a means to probe solid state quantum dynamics [37].

Appendix A

Hartree atomic units

Hartree atomic units (au) are convenient for calculations on scales relevant in atomic and molecular physics. The system of units is formed by setting $\hbar = m_e = e = 4\pi\epsilon_0 = 1$; where $\hbar$ is Planck's reduced constant, m_e is electronic mass, e is the absolute value of electronic charge and ϵ_0 is the vacuum permittivity [55]. For example, by using these constants the unit of length can be constructed with the relation

$$\frac{4\pi\epsilon_0\hbar^2}{m_e e^2} = \frac{\hbar}{\alpha m_e c} = a_0, \tag{A.1}$$

where the fine structure constant $\alpha = e^2/4\pi\epsilon_0\hbar c$ ($\alpha^{-1} \approx 137.036$) [55] is commonly used for expressing atomic units. As can be seen, the length scale is equivalent to the first Bohr radius a_0. A second example is the unit of energy given by

$$E_h = \frac{e^2}{4\pi\epsilon_0 a_0} = \alpha^2 m_e c^2. \tag{A.2}$$

This is known as Hartree energy and corresponds to double the ionization energy of a hydrogen atom in the limit of infinite nuclear mass [55]. Expressions for other atomic units and their equivalent values in terms of SI units are given in Table A.1.

Table A.1: Expressions defining units of various physical quantities in Hartree atomic units and their equivalent values in terms of SI units (rounded to six significant figures) [55].

Quantity	Expression	SI units
Length	a_0	0.529177×10^{-10} m
Mass	m_e	0.910938×10^{-30} kg
Charge	e	1.60218×10^{-19} C
Energy	E_h	4.35974×10^{-18} J
Action	$\hbar$	1.05457×10^{-34} J·s
Time	$\hbar/E_h$	2.41888×10^{-17} s
Velocity	αc	2.18769×10^{6} m/s
Electric field	$E_h/ea_0 = \alpha\hbar c/ea_0^2$	0.514221×10^{12} V/m
Force	E_h/a_0	0.823872×10^{-7} N
Power	$E_h^2/\hbar$	0.180238 W
Intensity	$E_h^2/\hbar a_0^2$	64.3641×10^{18} W/m^2

Bibliography

[1] A. Einstein. On the quantum theory of radiation. 1917.

[2] J. P. Gordon, H. J. Zeiger, and C. H. Townes. Molecular microwave oscillator and new hyperfine structure in the microwave spectrum of nh3. *Physical review*, 95(1):282–284, 1954.

[3] T. H. Maiman. Stimulated optical radiation in ruby. *Nature (London)*, 187(4736):493–494, 1960.

[4] J. Levesque and P. B. Corkum. Attosecond science and technology. *Canadian Journal of Physics*, 84(1):1–18, 2006.

[5] P. W. Milonni and J. H. Eberly. *Laser physics*. Wiley-Blackwell, Oxford, 2010.

[6] M. DiDomenico. Small-signal analysis of internal (coupling-type) modulation of lasers. *Journal of applied physics*, 35(10):2870–2876, 1964.

[7] L. E. Hargrove, R. L. Fork, and M. A. Pollack. Locking of he-ne laser modes induced by synchronous intracavity modulation. *Applied physics letters*, 5(1):4–5, 1964.

[8] T. Brabec and F. Krausz. Intense few-cycle laser fields: Frontiers of nonlinear optics. *Reviews of modern physics*, 72(2):545–591, 2000.

[9] A. H. Zewail. Laser femtochemistry. *Science (American Association for the Advancement of Science)*, 242(4886):1645–1653, 1988.

[10] P. B Corkum and F. Krausz. Attosecond science. *Nature physics*, 3(6):381–387, 2007.

[11] N. Bloembergen. *Nonlinear optics*. 1965.

[12] P. A. Franken, A. E. Hill, C. W. Peters, and G. Weinreich. Generation of optical harmonics. *Physical review letters*, 7(4):118, 1961.

[13] P. M. Paul and T. Le. Observation of a train of attosecond pulses from high harmonic generation. *Science (American Association for the Advancement of Science)*, 292(5522):1689–1692, 2001.

[14] M. Hentschel, R. Kienberger, C. Spielmann, G. A. Reider, N. Milosevic, T. Brabec, P. Corkum, U. Heinzmann, M. Drescher, and F. Krausz. Attosecond metrology. *Nature (London)*, 414(6863):509–513, 2001.

[15] P. B. Corkum. Plasma perspective on strong field multiphoton ionization. *Physical review letters*, 71(13):1994–1997, 1993.

[16] M. Drescher, M. Hentschel, R. Kienberger, M. Uiberacker, V. Yakovlev, A. Scrinzi, T. Westerwalbesloh, U. Kleineberg, U. Heinzmann, and F. Krausz. Time-resolved atomic inner-shell spectroscopy. *Nature (London)*, 419(6909):803–807, 2002.

[17] N. Milosevic, P. B. Corkum, and T. Brabec. How to use lasers for imaging attosecond dynamics of nuclear processes. *Physical review letters*, 92(1), 2004.

[18] J. Itatani, J. Levesque, D. Zeidler, H. Niikura, H. Pépin, J. C. Kieffer, P. B. Corkum, and D. M. Villeneuve. Tomographic imaging of molecular orbitals. *Nature (London)*, 432(7019):867–871, 2004.

[19] R. Locher, M. Lucchini, J. Herrmann, M. Sabbar, M. Weger, A. Ludwig, L. Castiglioni, M. Greif, M. Hengsberger, L. Gallmann, and U. Keller. Versatile attosecond beamline in a two-foci configuration for simultaneous time-resolved measurements. *Review of scientific instruments*, 85(1):013113–, 2014.

[20] L. Rego, K. M. Dorney, N. J. Brooks, Q. L. Nguyen, C-T. Liao, J. San Román, D. E. Couch, A. Liu, E. Pisanty, M. Lewenstein, L. Plaja, H. C. Kapteyn, M. M. Murnane, and C. Hernández-García. Generation of extreme-ultraviolet beams with time-varying orbital angular momentum. *Science (American Association for the Advancement of Science)*, 364(6447):eaaw9486–, 2019.

[21] S. Ghimire, A. D. DiChiara, E. Sistrunk, P. Agostini, L. F. DiMauro, and D. A. Reis. Observation of high-order harmonic generation in a bulk crystal. *Nature physics*, 7(2):138–141, 2011.

[22] H. Kim, S. Han, Y. W. Kim, S. Kim, and S-W. Kim. Generation of coherent extreme-ultraviolet radiation from bulk sapphire crystal. *ACS photonics*, 4(7):1627–1632, 2017.

[23] G. Vampa, T. J. Hammond, M. Taucer, X. Ding, X. Ropagnol, T. Ozaki, S. Delprat, M. Chaker, N. Thiré, B. E. Schmidt, F. Légaré, D. D. Klug, A. Yu Naumov, D. M. Villeneuve, A. Staudte, and P. B. Corkum. Strong-field optoelectronics in solids. *Nature photonics*, 12(8):465–468, 2018.

[24] H. Liu, Y. Li, Y. S. You, S. Ghimire, T. F. Heinz, and D. A. Reis. High-harmonic generation from an atomically thin semiconductor. *Nature physics*, 13(3):262–265, 2016.

[25] M. Garg, M. Zhan, T. T. Luu, H. Lakhotia, T. Klostermann, A. Guggenmos, and E. Goulielmakis. Multi-petahertz electronic metrology. *Nature (London)*, 538(7625):359–363, 2016.

[26] M. Hohenleutner, F. Langer, O. Schubert, M. Knorr, U. Huttner, S. W. Koch, M. Kira, and R. Huber. Real-time observation of interfering crystal electrons in high-harmonic generation. *Nature (London)*, 523(7562):572–575, 2015.

[27] O. Schubert, M. Hohenleutner, F. Langer, B. Urbanek, C. Lange, U. Huttner, D. Golde, T. Meier, M. Kira, S. W. Koch, and R. Huber. Sub-cycle control of terahertz high-harmonic generation by dynamical bloch oscillations. *Nature photonics*, 8(2):119–123, 2014.

[28] T. T. Luu, M. Garg, S. Y. Kruchinin, A. Moulet, M. T. Hassan, and E. Goulielmakis. Extreme ultraviolet high-harmonic spectroscopy of solids. *Nature (London)*, 521(7553):498–502, 2015.

[29] G. Ndabashimiye, S. Ghimire, M. Wu, D. A. Browne, K. J. Schafer, M. B. Gaarde, and D. A. Reis. Solid-state harmonics beyond the atomic limit. *Nature (London)*, 534(7608):520–523, 2016.

[30] Y. S. You, Y. Yin, Y. Wu, A. Chew, X. Ren, F. Zhuang, S. Gholam-Mirzaei, M. Chini, Z. Chang, and S. Ghimire. High-harmonic generation in amorphous solids. *Nature communications*, 8(1):724–5, 2017.

[31] N. Yoshikawa, T. Tamaya, and K. Tanaka. High-harmonic generation in graphene enhanced by elliptically polarized light excitation. *Science (American Association for the Advancement of Science)*, 356(6339):736–738, 2017.

[32] A. J. Uzan, G. Orenstein, Á. Jiménez-Galán, C. McDonald, R. E. F. Silva, B. D. Bruner, N. D. Klimkin, V. Blanchet, T. Arusi-Parpar, M. Krüger, A. N. Rubtsov, O. Smirnova, M. Ivanov, B. Yan, T. Brabec, and N. Dudovich. Attosecond spectral

singularities in solid-state high-harmonic generation. *Nature photonics*, 14(3):183–187, 2020.

[33] G. Vampa, C. R. Mcdonald, G. Orlando, D. D. Klug, P. B. Corkum, and T. Brabec. Theoretical analysis of high-harmonic generation in solids. *Physical review letters*, 113(7):073901, 2014.

[34] H. Haug and S. W. Koch. *Quantum theory of the optical and electronic properties of semiconductors*. World Scientific, Singapore, 5th edition, 2009.

[35] G. Vampa, C. R. McDonald, G. Orlando, P. B. Corkum, and T. Brabec. Semiclassical analysis of high harmonic generation in bulk crystals. *Physical review. B, Condensed matter and materials physics*, 91(6), 2015.

[36] C. R. Mcdonald, G. Vampa, P. B. Corkum, and T. Brabec. Intense-laser solid state physics: Unraveling the difference between semiconductors and dielectrics. *Physical review letters*, 118(17):173601, 2017.

[37] G. Vampa, T. J. Hammond, N. Thiré, B. E. Schmidt, F. Légaré, C. R. McDonald, T. Brabec, and P. B. Corkum. Linking high harmonics from gases and solids. *Nature (London)*, 522(7557):462–464, 2015.

[38] S. Almalki, A. M. Parks, G. Bart, P. B. Corkum, T. Brabec, and C. R. McDonald. High harmonic generation tomography of impurities in solids: Conceptual analysis. *Physical review. B*, 98(14), 2018.

[39] G. Vampa, B. G. Ghamsari, S. Siadat Mousavi, T. J. Hammond, A. Olivieri, E. Lisicka-Skrek, A. Y. Naumov, D. M. Villeneuve, A. Staudte, P. Berini, and P. B. Corkum. Plasmon-enhanced high-harmonic generation from silicon. *Nature physics*, 13(7):659–662, 2017.

[40] M. Sivis, M. Taucer, G. Vampa, K. Johnston, A. Staudte, A. Y. Naumov, D. M. Villeneuve, C. Ropers, and P. B. Corkum. Tailored semiconductors for high-harmonic optoelectronics. *Science (American Association for the Advancement of Science)*, 357(6348):303–306, 2017.

[41] S. Han, H. Kim, Y. W. Kim, Y-J. Kim, S. Kim, I-Y. Park, and S-W. Kim. High-harmonic generation by field enhanced femtosecond pulses in metal-sapphire nanostructure. *Nature communications*, 7(1):13105–, 2016.

[42] R. de L. Kronig and W. G. Penney. Quantum mechanics of electrons in crystal lattices. *Proceedings of the Royal Society of London. Series A, Containing papers of a mathematical and physical character*, 130(814):499–513, 1931.

[43] F. Bloch. *Z. Physik*, 52:555, 1928.

[44] C. Kittel. *Introduction to solid state physics*. J. Wiley, New York, 8th ed. edition, 2005.

[45] G. H. Wannier. The structure of electronic excitation levels in insulating crystals. *Physical review*, 52(3):191–197, 1937.

[46] W Kohn. Analytic properties of bloch waves and wannier functions. *Physical review*, 115(4):809–821, 1959.

[47] M. J. Ablowitz and A. S. Fokas. *Complex variables : introduction and applications*. Cambridge texts in applied mathematics. Cambridge University Press, Cambridge, 2nd edition, 2003.

[48] L. V. Keldysh. Ionization in the field of a strong electromagnetic wave. *Soviet Physics JETP*, 20(5):1307–1314, 1965.

[49] E.I Blount. *Formalisms of Band Theory*. Elsevier, 1962.

[50] U. Lindefelt, H-E. Nilsson, and M. Hjelm. Choice of wavefunction phases in the equations for electric-field-induced interband transitions. *Semiconductor Science and Technology*, 19(8):1061–1066, 2004.

[51] M. V. Berry. Quantal phase factors accompanying adiabatic changes. *Proceedings of the Royal Society A.*, 392(1802):45–57, 1984.

[52] M. Lewenstein, P. Balcou, M. Y. Ivanov, A. L'Huillier, and P. B. Corkum. Theory of high-harmonic generation by low-frequency laser fields. *Physical review. A, Atomic, molecular, and optical physics*, 49(3):2117–2132, 1994.

[53] M. Abramowitz and I. A. Stegun. *Handbook of mathematical functions with formulas, graphs, and mathematical tables*. Selected government publications. Wiley, New York, 1972.

[54] R. Ravichandran, A. X. Wang, and J. F. Wager. Solid state dielectric screening versus band gap trends and implications. *Optical materials*, 60(C):181–187, 2016.

[55] G. W. F Drake. *Springer Handbook of Atomic, Molecular, and Optical Physics*. Springer-Verlag, New York, NY, 2. aufl. edition, 2005.